



## 저작자표시-비영리-변경금지 2.0 대한민국

이용자는 아래의 조건을 따르는 경우에 한하여 자유롭게

- 이 저작물을 복제, 배포, 전송, 전시, 공연 및 방송할 수 있습니다.

다음과 같은 조건을 따라야 합니다:



저작자표시. 귀하는 원저작자를 표시하여야 합니다.



비영리. 귀하는 이 저작물을 영리 목적으로 이용할 수 없습니다.



변경금지. 귀하는 이 저작물을 개작, 변형 또는 가공할 수 없습니다.

- 귀하는, 이 저작물의 재이용이나 배포의 경우, 이 저작물에 적용된 이용허락조건을 명확하게 나타내어야 합니다.
- 저작권자로부터 별도의 허가를 받으면 이러한 조건들은 적용되지 않습니다.

저작권법에 따른 이용자의 권리는 위의 내용에 의하여 영향을 받지 않습니다.

이것은 [이용허락규약\(Legal Code\)](#)을 이해하기 쉽게 요약한 것입니다.

[Disclaimer](#)

공학박사학위논문

기판과 접촉하는 그래핀의 열전도도 계측

Thermal Conductivity Measurement of Supported  
Graphene in Contact with Substrate

2018 년 2 월

서울대학교 대학원

기계항공공학부

김 홍 구

# 기판과 접촉하는 그래핀의 열전도도 측정

## Thermal Conductivity Measurement of Supported Graphene in Contact with Substrate

지도교수 고 승 환

이 논문을 공학박사 학위논문으로 제출함

2017 년 10 월

서울대학교 대학원

기계항공공학부

김 홍 구

김홍구의 공학박사 학위논문을 인준함

2017 년 12 월

위 원 장 : 전 누리

부위원장 : 고 승 환

위 원 : 조 형 록

위 원 : KENNETH D. KIHM

위 원 : 이 준 석



# **Thermal Conductivity Measurement of Supported Graphene in Contact with Substrate**

Hong Goo Kim

School of Mechanical and Aerospace Engineering  
Seoul National University

## **Abstract**

Graphene as a two-dimensional material with outstanding characteristics has attracted immense interest in recent years. Due to its extraordinarily high thermal conductivity, application of graphene as a heat spreading material for thermal management has high expectations.

However, experimental reports on thermal properties of graphene have been leaned toward the freely *suspended* graphene samples, while it is the *supported* graphene in contact with a substrate that is suited for practical applications. Scarcity of experimental studies on supported graphene thermal conductivity is due to the lack of a reliable high-throughput measurement technique, since the methods hitherto deployed had serious drawbacks.

Micro resistance thermometry technique has been implemented in measuring the thermal conductivity of supported graphene at temperatures from 100 K to 400

K. Despite its excellent measurement accuracy, complicated sample fabrication process leads to high cost and as well as contamination of the graphene. On the contrary, optothermal Raman method is easy to implement and does not require patterning or etching of graphene samples. However, when applied to supported graphene, the measurement uncertainties of optothermal Raman technique is excessively high, resulting in questionable thermal conductivity data.

In this study, we developed a thermal conductivity measurement technique based on the optothermal Raman method with a dramatically improved measurement accuracy for supported graphene. By conducting a three-dimensional heat transfer analysis on optothermal Raman measurements, we found that the critical parameter that affects the measurement accuracy is the substrate thickness. Advantage of a thin substrate has been demonstrated experimentally through conducting the optothermal Raman measurement of supported graphene thermal conductivity.

For the first time, thermal conductivity of supported graphene has been measured at temperatures from 350 K to 600 K, which is essential for applications in thermal managing. Furthermore, we observed the strong dependence of thermal conductivity on varying degrees of graphene-substrate conformity due to thermal pre-annealing. Investigation of Raman G and 2D peaks of supported graphene revealed that repeated thermal annealing resulted in enhanced graphene-substrate conformity. A theoretical analysis based on elastic theory has been conducted, where reduction in thermal conductivity was attributed to increased substrate-

induced phonon scattering arising from graphene-substrate conformity.

The measurement technique in this work applies not only to supported graphene, but also could lead to extensive studies in graphene-analogous 2D materials and their applications in thermal management. The wide variations in thermal conductivity of supported graphene through thermo-mechanical affiliation of graphene and substrate could offer an alternative route to tailoring the thermal properties of graphene.

Keywords: thermal conductivity, supported graphene, optothermal Raman technique, graphene-substrate conformity, substrate-induced phonon scattering, thermal expansion mismatch, finite-difference method, CVD

Student Number: 2011-20704

# Contents

<b>Abstract</b>	i
<b>Contents</b>	iv
<b>List of Tables</b>	viii
<b>List of Figures</b>	ix
<b>Nomenclature</b>	xvi
 <b>Chapter 1. Introduction</b>	
1.1 Motivation and objectives	1
1.1.1 Graphene as a promising material	1
1.1.2 Importance of supported graphene thermal conductivity for practical applications	1
1.1.3 Thermometry techniques for thermal conductivity measurement	2
1.1.4 Objectives and prospects of this work	3
1.2 Review of previous studies	4
1.2.1 Thermal conductivity of graphene in general	4
1.2.2 Theoretical studies on supported graphene thermal conductivity	6
1.2.3 Measurement techniques of supported graphene thermal conductivity	7
1.3 Overview	8

## **Chapter 2. Experimental Design**

2.1 Introduction	12
2.2 Optothermal Raman technique	14
2.3 Sample design	15
2.4 Governing equations and boundary conditions	16
2.4.1 Heat transfer model in 2D	17
2.4.2 Heat transfer model in 3D	18
2.4.3 Finite difference method and numerical analysis	21
2.5 Improvement in measurement accuracy	22
2.5.1 Inadequacy of the 2D heat transfer model	22
2.5.2 Advantages of the thin SiO <sub>2</sub> substrate	23
2.6 Conclusion	27

## **Chapter 3. Sample Preparation and Characterization**

3.1 Synthesis of graphene	42
3.1.1 Sample requirements and growth mechanism of CVD graphene	43
3.1.2 CVD system	45
3.1.3 CVD synthesis of graphene	46
3.2 Transfer of graphene	47
3.3 Characterization	48
3.3.1 Scanning electron microscopy (SEM)	48
3.3.2 X-ray photoelectron spectroscopy (XPS)	49



3.3.3 Optical microscopy	49
3.3.4 Raman spectroscopy	49
3.4 Conclusion	51

## **Chapter 4. Optothermal Raman Measurement of Supported Graphene Thermal Conductivity**

4.1 Introduction	65
4.2 Effective optical absorbance of supported graphene	65
4.3 Sample description in terms of thermal annealing	67
4.4 Raman peak position vs. temperature	67
4.4.1 Linear temperature dependence of Raman peaks for samples 1st, 2nd, and 3rd	68
4.4.2 Curve-fitting of temperature dependence of Raman peaks for samples 4th, Nth, and VAC	68
4.5 Temperature vs. laser power	71
4.6 Thermal conductivity dependence on pre-annealing	72
4.7 Conclusion	74

## **Chapter 5. Effect of Graphene-Substrate Interactions on Thermal Conductivity of Supported Graphene**

5.1 Introduction	87
5.2 Effect of thermal annealing on graphene-substrate conformity	88

5.2.1 Height ratio and FWHM of Raman peaks	89
5.2.2 Charge carrier concentration of supported graphene	89
5.2.3 Increase in temperature coefficients of Raman peaks as a result of thermal annealing	91
5.3 Effect of graphene-substrate separation distance on thermal conductivity	92
5.4 Effect of intercalated layer of water on thermal conductivity	93
5.5 Conclusion	94
<b>Chapter 6. Summary and Conclusions</b>	<b>104</b>
<b>References</b>	<b>107</b>
<b>Appendix – MATLAB codes for numerical simulations</b>	<b>122</b>
Appendix A. 3D heat transfer model for supported graphene	122
Appendix B. Effect of graphene-SiO <sub>2</sub> conformity on force constant	132
Appendix C. Effect of intercalated water layer on force constant	136
<b>Abstract (in Korean)</b>	<b>138</b>

## List of Tables

- Table 2.1 Comparison of  $k_g$  dependence on  $G_b$  and  $k_{SiO_2}$ , demonstrating the superior accuracy of using a thin substrate
- Table 3.1 Comparison of graphene synthesis techniques
- Table 4.1 Temperature coefficients of Raman G and 2D peak positions for 1st, 2nd, and 3rd samples

## List of Figures

- Figure 1.1 Schematic representations of suspended graphene (above), and supported graphene (below) configurations.
- Figure 1.2 Thermal conductivity values of supported graphene obtained from experiments.
- Figure 2.1 Schematic comparison of heat transfer in supported graphene (above) and suspended graphene (below).
- Figure 2.2 Minimization of heat dissipation through the substrate for a supported graphene could be achieved by reducing the thickness of the substrate, resulting in a heat flow similar to that of a suspended graphene.
- Figure 2.3 (a) Schematic representation of an optothermal Raman measurement for a suspended membrane (graphene). (b) Procedures of an optothermal Raman measurement.
- Figure 2.4 (a) Specimen using 8-nm-thick SiO<sub>2</sub> TEM grid as the substrate, (b) and its optical image.
- Figure 2.5 Heat transfer in a supported graphene sample for an optothermal Raman measurement in cylindrical coordinate system. ‘//’ and ‘⊥’ represent the in-plane and out-of-plane directions with respect to the supported graphene, respectively.
- Figure 2.6 Discretized  $r$  and  $z$  for the supported graphene (above) and the substrate (below) for numerical analysis.

Figure 2.7 Spatial temperature distribution obtained using Eqs. (2.3) ~ (2.11) for a supported graphene with 8-nm-thick substrate, assuming  $k_g = 1000$  W/m K,  $k_{\text{sub}} = 1.38$  W/m K,  $G_b = 25$  MW/m<sup>2</sup> K, and the incident laser power of 2.49 mW. It is shown that the temperature difference along the cross-plane direction ( $\perp$ ) is negligible to that along the in-plane direction ( $\parallel$ ). Also it is demonstrated that the large lateral size of our supported graphene (70  $\mu\text{m}$ ) justifies imposing a constant temperature ( $T_\infty$ ) boundary condition at  $r = R$  in evaluating the thermal conductivity of the graphene ( $k_g$ ).

Figure 2.8 Evaluation of thermal conductivity and constant cross-plane heat transfer coefficient using a 2D heat transfer model, Eq. (2.2), and two objective lenses (50x, 100x), where true value of  $k_g$  is assumed as 1000 W/m K. It is clearly seen that the  $k_g$  deduced from the 2D model (1430 W/m K) is significantly overestimated, stressing the importance of a 3D heat transfer model.

Figure 2.9 Comparison of cross-plane heat transfer coefficient at the graphene-substrate interface ( $g$ ), between 3D heat transfer model and 2D heat transfer model. It is shown that constant-value  $g$  approximation for a 2D model results in an underestimation of  $g$ , which actually is a spatial variable, near the heating zone ( $r < r_0$ ).

Figure 2.10 Dependence of evaluated  $k_g$  on the variation of  $G_b$  for a thin substrate (8 nm) and a thick substrate (10000 nm). Supported graphene thermal conductivity deviates significantly from the true value (assumed as 1000 W/m K for this case) depending on the  $G_b$  value that is coupled with large uncertainty.

Figure 2.11 Dependence of evaluated  $k_g$  on the variation of  $k_{\text{SiO}_2}$  for a thin

substrate (8 nm) and a thick substrate (10000 nm).

Figure 2.12 Dependence of evaluated  $k_g$  on the measured temperature ( $T_m$ ) for a thin substrate (8 nm) and a thick substrate (10000 nm).

Figure 3.1 Schematic of chemical vapor deposition technique.

Figure 3.2 Growth of graphene on a copper foil. (a) Copper foil as received. (b) Recrystallization of copper after annealing at 1000 °C. (c) Initial stage of graphene growth – formation of graphene islands. (d) Complete growth of graphene on copper foil.

Figure 3.3 Relation between nucleation density ( $n$ ) of graphene growth and CVD synthesis parameters.

Figure 3.4 Schematic of the CVD equipment.

Figure 3.5 Photographic image of the CVD equipment and its components.

Figure 3.6 Graphene CVD synthesis procedure using  $\text{CH}_4$  and  $\text{H}_2$  as precursor gas.

Figure 3.7 Comparison of SEM image of graphene/copper foil sample with (below) and without (above) pre-cleansing of the copper foil. Note the difference in contaminant (white particles) densities.

Figure 3.8 Transfer of graphene from copper foil catalyst to target substrate using PMMA method. (a) Graphene as synthesized by CVD technique. (b) PMMA flexible membrane spin-coated on graphene. (c) Removal of the graphene at the other side (backside) of the copper

foil. (d), (e) Etching of copper in ammonium persulfate. (f) Cleansing in deionized water. (g) Graphene/PMMA sample brought to contact with the target substrate. (h), (i) Dissolution of the PMMA top layer in acetone.

Figure 3.9 SEM image of initial stage of the graphene growth. Flow rates for CH<sub>4</sub> and H<sub>2</sub> were 30 sccm and 5 sccm, respectively, at 1000 °C.

Figure 3.10 Core electron binding energy of carbon (C1s spectrum) for CVD synthesized graphene. XPS measurement was taken at NCIRF, SNU.

Figure 3.11 Optical microscopy (100x lens) image of CVD graphene on SiO<sub>2</sub>/Si wafer with SiO<sub>2</sub> thickness of 280 nm. Mostly uniform shade of the image indicates monolayer dominant characteristic of our sample, without major cracks.

Figure 3.12 Raman spectrum of the CVD graphene sample transferred on 8-nm-thick SiO<sub>2</sub> TEM grid.

Figure 4.1 Procedure of determining the effective absorbance of supported graphene on 8-nm-thick SiO<sub>2</sub> substrate using a powermeter.

Figure 4.2 Photographic image of the powermeter (above) and the temperature-controlled heated stage (below).

Figure 4.3 Thermal annealing conditions for 1st, 2nd, 3rd, 4th and Nth samples.

Figure 4.4 Temperature dependence of Raman G peak positions for 1st (a), 2nd (b), and 3rd (c) samples.

Figure 4.5 Temperature dependence of Raman 2D peak positions for 1st (a), 2nd

(b), and 3rd (c) samples.

Figure 4.6 Temperature dependence of Raman G peak positions for 4th, Nth, and VAC samples, along with the prediction and confidence bands determined from Bonferroni criteria.

Figure 4.7 Curve fitting of Raman G peak position as a function of temperature change for the Nth sample, where temperature change is the summation of intrinsic component and thermal expansion mismatch induced strain component.

Figure 4.8 Thermal expansion mismatch coefficient of monolayer graphene deduced from the curve-fitting of Raman G peak position as a function of temperature.

Figure 4.9 Shifts of Raman G (left) and 2D (right) peak positions upon varying laser power for 1st, 2nd, 3rd, 4th, Nth, and VAC samples.

Figure 4.10 Thermal conductivity of graphene ( $k_g$ ) as a function of measured temperature ( $T_m$ ) divided by laser power ( $P_L$ ), obtained from the 3D heat transfer model and spline interpolation.

Figure 4.11 Thermal conductivity of supported graphene at various temperatures for 1st, 2nd, 3rd, 4th, Nth, and VAC samples, using either Raman G or 2D peaks.

Figure 4.12 Comparison of thermal conductivity values with previous works.

Figure 5.1 Schematic comparison of supported graphene as prepared (above), and after annealing (below).



- Figure 5.2 Raman spectra of supported graphene as prepared and after 10th thermal annealing. Notice the significant decrease in the ratio of height between Raman 2D and G peaks.
- Figure 5.3 Raman peak positions of supported graphene samples with varying degree of thermal pre-annealing, measured at room temperature in atmospheric conditions. By vector decomposition of the p-doping components (slope = 0.7) and the strain component (slope = 2.2), difference in positive charge carrier concentrations between the samples could be estimated.
- Figure 5.4 Comparison of the temperature dependence of Raman G (above) and 2D (below) peaks of supported graphene samples with varying degree of thermal pre-annealing.
- Figure 5.5 Schematic representation of the simplified model for a supported graphene over a substrate with a sinusoidal corrugations.
- Figure 5.6 Relations between the force constant and the degree of conformation parameters,  $h$  and  $\delta_g$ . Here,  $h_0$  is the equilibrium distance between a flat graphene and a flat substrate free of corrugation and strain.
- Figure 5.7 Schematic of the balance between the forces enacting over a supported monolayer graphene with an intercalated layer of  $H_2O$ , where  $F_1$  is the downward force due to the ambient atmospheric pressure,  $F_2$  is the compressive force exerted by the  $H_2O$  layer, and  $F_{vdW}$  is the attractive force induced by the graphene-substrate van der Waals interaction.
- Figure 5.8 Net force constant ( $K_{net}$ ) as a function of normalized separation distance between graphene and  $SiO_2$  substrate with intercalated  $H_2O$

layer in between.

## Nomenclature

$A$	area ( $\text{m}^2$ )
$E$	energy (J)
$F$	force (N)
$g$	cross-plane heat transfer coefficient ( $\text{W}/\text{m}^2 \text{ K}$ )
$G_b$	thermal boundary conductance ( $\text{W}/\text{m}^2 \text{ K}$ )
$h$	convection heat transfer coefficient ( $\text{W}/\text{m}^2 \text{ K}$ )
$I$	height of Raman peaks (arbitrary unit)
$k$	thermal conductivity ( $\text{W}/\text{m K}$ )
$k_B$	Boltzmann constant ( = $1.38 \times 10^{-23} \text{ J/K}$ )
$K$	force constant (N/m)
$l$	length (m)
$MSE$	means squared error
$N$	total number
$n$	number density of nucleation points ( $\text{m}^{-2}$ )
$n_p$	number density of p-type charge carriers ( $\text{cm}^{-2}$ )
$NA$	numerical aperture of the objective lens
$P$	laser power (W)
$\mathbf{q}''$	heat flux ( $\text{W}/\text{m}^2$ )
$r$	radial distance from the origin of cylindrical coordinate system (m)

$r_0$	Gaussian beam radius (m)
$R_{s,th}$	sheet thermal resistance (K/W)
$t$	thickness (m)
$T$	temperature
$\dot{V}$	volumetric flow rate (m <sup>3</sup> /s)
$z$	vertical coordinate in cylindrical system (m)

### **Greek symbols**

$\alpha$	optical absorbance (%)
$\beta$	linear thermal expansion coefficient (K <sup>-1</sup> )
$\gamma$	Grüneisen parameter
$\Gamma$	equilibrium van der Waals energy per unit area (J/m <sup>2</sup> )
$\delta$	corrugation amplitude (m)
$\varepsilon$	strain
$\lambda$	wavelength (m)
$\rho$	optical reflectance (%)
$\theta$	angular coordinate in cylindrical system (rad)
$\omega$	Raman peak position (cm <sup>-1</sup> )

### **Subscripts**

2D	Raman 2D peak
b	boundary

eff	effective
g	graphene
G	Raman G peak
L	laser
m	measured
p	p-type charge carrier
sub	substrate
vdW	van der Waals

# **Chapter 1**

## **Introduction**

### **1.1 Motivation and objectives**

#### **1.1.1 Graphene as a promising material**

Graphene has attracted significant interest in recent years, due to its fascinating properties since its demonstration by Novoselov et al. (2004). Graphene is a planar array of carbon atoms in hexagonal rings of  $sp^2$  covalent bonding, an ultimate two-dimensional material that is constituted only by atoms that are exposed to the surface. Graphene has the highest electronic mobility (Bolotin et al., 2008) as well as the highest mechanical strength (Lee et al., 2008) and the highest thermal conductivity (Balandin et al., 2008), combined with its optical transparency and flexibility, offering great opportunities for electronic device applications (Castro Neto et al., 2009; Novoselov et al., 2012).

#### **1.1.2 Importance of supported graphene thermal conductivity for practical applications**

Studies on the thermal properties of graphene not only enable the exploitation of the outstanding heat spreading capability for thermal management applications, but also lead to a collective understanding of the thermal properties of graphene-

analogous two-dimensional materials (Geim and Grigorieva, 2013; Novoselov et al., 2016; Wang et al., 2017). Thermal transport in graphene is mostly contributed by phonons, quantized vibrational modes arising from the elasticity of periodic sp<sup>2</sup> covalent bonding of carbon atoms (Balandin, 2011; Pop et al., 2012; Sadeghi et al., 2012; Xu et al., 2014).

The extreme characteristics of graphene are mostly reported for a free-standing ‘suspended’ graphene that is effectively isolated from interactions from the external environment as shown in Figure 1.1. However, for any practical applications, graphene is inevitably brought to an interfacial contact with a solid substrate, becoming a ‘supported’ graphene, since a stand-alone single-atom-thick graphene is costly to realize and virtually impossible to mass produce. Due to its nature as a surface material, it has been observed that the thermal conductivity of graphene is significantly altered when the graphene is in contact with a solid substrate, where a reduction in thermal conductivity by nearly an order-of-magnitude has been reported (Seol et al., 2010; Cai et al., 2010).

### **1.1.3 Thermometry techniques for thermal conductivity measurement**

Despite the high demand for an extensive study on the thermal properties of supported graphene for practical applications, experimental reports have been scarce due to the lack of a reliable high-throughput measurement technique. Micro resistance thermometry of supported graphene, developed by the research group of L. Shi (Seol et al., 2010; Seol et al., 2011; Sadeghi et al., 2013) involves a

complicated low-yield sample fabrication process which is difficult to emulate, notwithstanding its superior measurement accuracy. On the other hand, while optothermal Raman technique devised by the research group of A. Balandin (2008) has proven to be a simple and effective tool for thermometry of *suspended* graphene, its deployment to supported graphene thermometry showed unacceptably high measurement uncertainties (Cai et al., 2010).

The scarcity of experimental reports on supported graphene leads to a complete absence of thermal conductivity data at high temperature regimes of more than 400 K, as shown in Figure 1.2. Taking into considerations the hot spot temperatures of graphene devices that exceed 400 K (Yan et al., 2012; Kim et al., 2016), evaluation of the supported graphene thermal conductivity at higher temperature regime has a high priority.

#### **1.1.4 Objectives and prospects**

In this dissertation we develop a reliable and efficient optothermal Raman technique for the measurement of supported graphene thermal conductivity, optimized for room temperature and above. By conducting a three-dimensional heat transfer analysis we optimize the sample configuration, where thickness of the substrate turns out to be the most critical parameter in improving the measurement accuracy of the supported graphene thermal conductivity. Our thermometry technique should be applicable for future studies on thermal conductivity of any two-dimensional material supported by a substrate.



We not only aim to measure and delineate the thermal conductivity of monolayer supported graphene at temperatures ranging from 350 K to 600 K, but also account for the varying degree of substrate-induced phonon scattering of graphene arising from graphene-substrate conformity. Consequently we demonstrate the possibility of modulating the thermal conductivity of supported graphene through controlling the thermo-mechanical affiliation of graphene to substrate.

## **1.2 Review of previous studies**

### **1.2.1 Thermal conductivity of graphene in general**

The intrinsic thermal conductivity of graphene (freely suspended graphene) is reported range from 2000 to 4000 W/m K at room temperature by optothermal Raman measurements (Balandin et al., 2008; Cai et al., 2010; Chen et al., 2012a), which is among the highest values for the existing materials. Ultrahigh in-plane thermal conductivity of graphene is attributed to high bond strength to atomic mass ratio of sp<sup>2</sup>-bonded carbons, resulting in a strong lattice vibrational modes (Pop et al., 2012). The defining feature of thermal property that differentiates graphene from graphite, a vertical stack of graphene layers bound by weak van der Waals force, is the strong out-of-plane acoustic vibrational modes (ZA phonons), which is a unique aspect of graphene as a truly two-dimensional material. It is widely accepted that ZA phonon branch is the dominant contributor

to the in-plane thermal conduction of graphene (Sadeghi et al., 2011; Pop et al., 2012), where a theory predicts that the contribution of ZA modes to thermal conductivity room temperature is over 70% (Lindsay et al., 2010).

Due to its very long intrinsic phonon mean path of over 600 nm (Pop et al., 2012), thermal conductivity of graphene is easily affected by defects and has a strong size effect. A. Balandin's research group of reported the substantial decrease in thermal conductivity of suspended graphene due to carbon isotope concentration using the optothermal Raman technique, where  $C^{13}$  acts as a phonon scattering source due to atomic mass difference (Chen et al., 2012). Size effect of thermal conductivity of suspended graphene has been investigated by micro resistance thermometry technique, showing the strong dependence of thermal conductivity on sample length from 300 nm to 600 nm (Xu et al., 2014). Optothermal Raman measurement revealed that grain boundary, a line defect of dislocated carbon atoms, also suppress the thermal conductivity of suspended graphene, where the effect was marked for samples with grain size of less than 1  $\mu m$  (Lee et al., 2017).

While intrinsic thermal conductivity of graphene was believed to be limited by 'umklapp' process, referring to a phonon scattering process that results in a net momentum change of phonons, a recent theoretical study suggests that momentum-conserving process of phonons also play a significant role in thermal conduction of graphene, especially at low temperature regimes (Lee et al., 2015a). Another theoretical study argues that theoretical limit of suspended graphene

thermal conductivity is achieved at a sample size greater than 1 mm, where collective phonon excitations with mean free paths of several hundred micrometers are the main heat carriers (Fugallo et al., 2014).

### **1.2.2 Theoretical studies on supported graphene thermal conductivity**

There is a wide consensus among theoretical studies that the thermal conductivity of a supported graphene in contact with a solid substrate is significantly lower than that of a freely suspended graphene. Previous theoretical studies on supported graphene thermal conductivity are based on either molecular dynamics (MD) or Boltzmann transport equation (BTE) approaches.

MD simulation reported that the thermal conductivity of supported graphene is independent of the thickness of the substrate, implying the predominance of surface atoms of the substrate on graphene-substrate interaction (Chen et al., 2013). However, there are conflicting views on the thermal conductivity dependence on graphene-substrate coupling strength, where some groups reported a significant decrease in thermal conductivity due to shortened phonon lifetime (Qiu and Ruan, 2012; Chen et al., 2013; Lee et al., 2015), while Eric Pop group predicted an increase in thermal conductivity due to coupling of graphene ZA phonons to the substrate Rayleigh waves which linearizes the phonon dispersion of graphene (Ong and Pop, 2011). Size dependence of supported graphene is believed to be weaker than that of suspended graphene due to strong substrate-graphene coupling (Chen et al., 2013). Another MD simulation revealed the

importance of interfacial morphology and graphene-substrate morphology, where a nonconformed graphene (923 W/m K) showed a significantly higher thermal conductivity than an optimally conformed graphene (713 W/m K). BTE simulations by N. Mingo's group and Li Shi's group emphasized the role of ZA phonons in thermal conduction of graphene and the suppression of ZA phonons in supported graphene resulting in a significantly reduced thermal conductivity values that are in good agreement with the experiment (Lindsay et al., 2010; Seol et al., 2010).

The thermal conductivity values of supported graphene on SiO<sub>2</sub> at room temperature predicted by theories range from approximately 600 W/m K (Lindsay et al., 2010; Seol et al., 2010; Ong and Pop, 2011; Chen et al., 2013) to 923 W/m K (Lee et al., 2015b).

### **1.2.3 Measurement techniques of supported graphene thermal conductivity**

Previous experimental studies on supported graphene thermal conductivity are plotted in Figure 1.2. Most studies are based on micro resistance thermometry technique (Seol et al., 2010; Wang et al., 2011; Bae et al., 2013; Sadeghi et al., 2013), while a sole data point at room temperature is obtained by optothermal Raman technique (Cai et al., 2010).

Micro resistance method probes the temperature of the supported graphene sample from the linear dependence of electrical resistance of metallic thermometers on temperature, where one-dimensional heat flow rate is determined

from the spatial temperature difference between thermometers placed at different positions. Li Shi's group fabricated a supported graphene on a suspended 300-nm-thick SiO<sub>2</sub> beam structure and reported a steady increase in thermal conductivity at temperatures from 100 K to 380 K, obtaining a peak value of 636 W/m K at 300 K for a supported monolayer graphene (Seol et al., 2010; Sadeghi et al., 2013). On the other hand, Eric Pop's group developed a micro resistance technique with graphene samples patterned on a 290-nm-thick SiO<sub>2</sub> substrate deposited on silicon, reporting the length and width dependence of supported monolayer graphene nanoribbon samples (Bae et al., 2013; Li et al., 2014). While micro resistance technique shows a superior measurement accuracy, complicated series of patterning and etching processes are not only costly but also vulnerable to defect-generation and contamination of the supported graphene samples.

Optothermal Raman technique, while serving as the primary tool for measuring the thermal conductivity of suspended graphene, its application to supported graphene on an Au/Si<sub>x</sub>N<sub>y</sub> substrate showed large measurement uncertainties (370 + 650/−320 W/m K), partly due to the overly approximated heat transfer model, and partly due to the excessive cross-plane dissipation of heat to the substrate, as will be discussed in Chapter 2.

### 1.3 Overview

In Chapter 2, we develop a three-dimensional heat transfer model accounting

for the spatial temperature distribution of optothermal Raman measurements. We demonstrate the inadequacy of previous two-dimensional heat transfer model and the advantages of using a thin substrate with respect to measurement accuracy.

In Chapter 3, the preparation of the sample is presented, including the synthesis of graphene and its transfer to the target substrate. Synthesized graphene sample is characterized by optical microscopy, scanning electron microscopy, Raman spectroscopy, and X-ray photoelectron spectroscopy techniques.

In Chapter 4, optothermal Raman method is implemented, measuring the thermal conductivity of supported monolayer graphene at temperatures from 350 K to 600 K. It is shown that thermal conductivity of supported graphene is dependent on the number of pre-annealing cycles as well as the measurement temperature.

In Chapter 5, the effect of thermal annealing on thermal conductivity of the supported graphene is examined, where it is revealed that enhanced graphene-substrate conformity increases the substrate-induced phonon scattering rate, thereby decreasing the thermal conductivity of graphene. Chapter 6 summarizes the results.

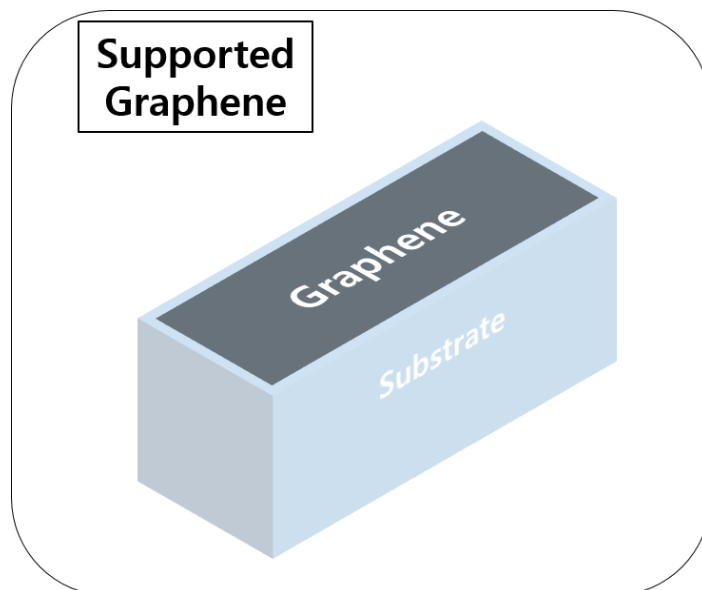
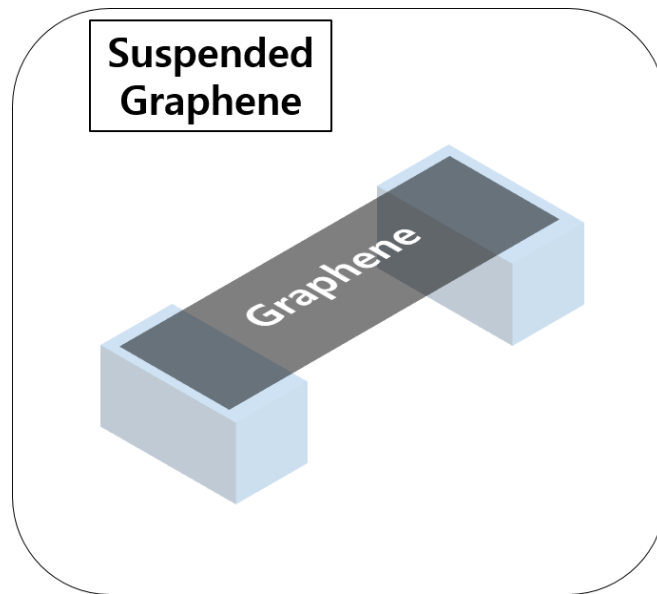


Figure 1.1 Schematic representations of suspended graphene (above), and supported graphene (below) configurations.

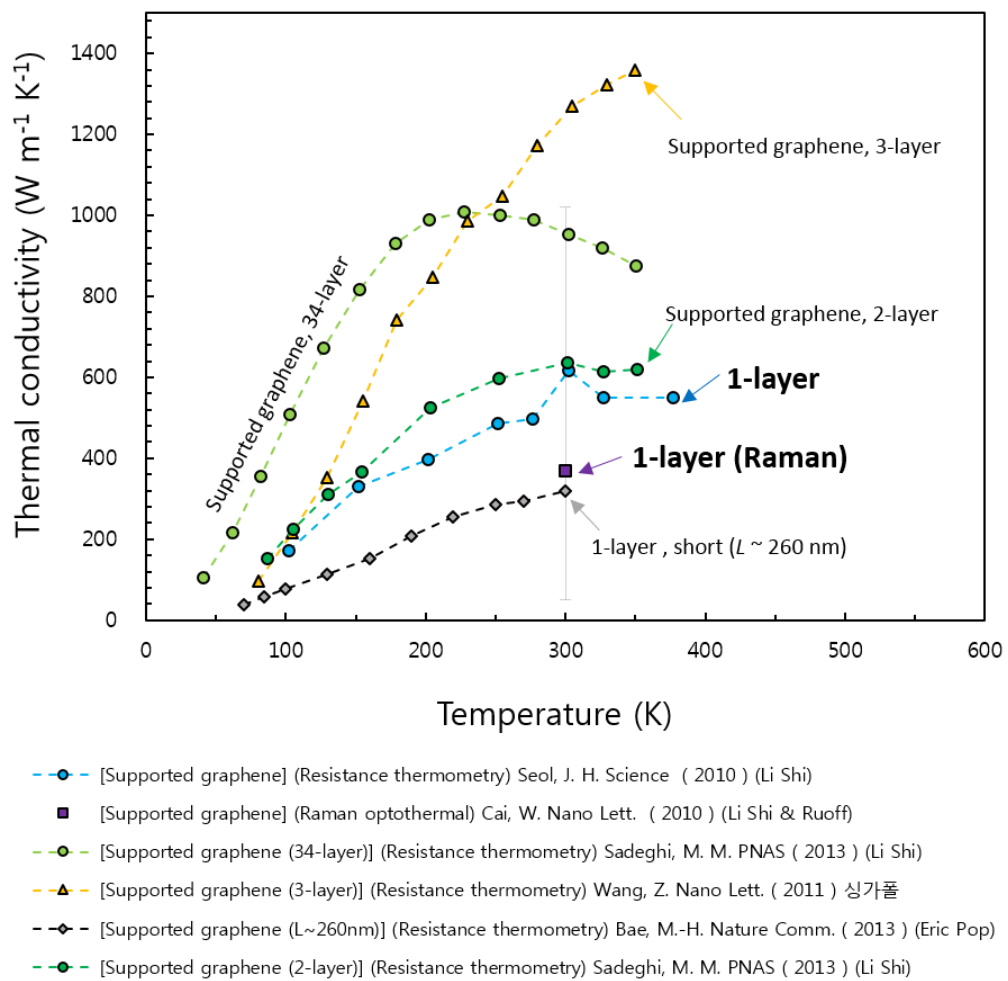


Figure 1.2 Thermal conductivity values of supported graphene obtained from experiments.



# **Chapter 2**

## **Experimental Design**

### **2.1 Introduction**

Measuring the thermal conductivity of a supported graphene has major challenges to overcome as compared with a suspended graphene. A suspended graphene consists of a graphene that is effectively isolated from the surrounding in terms of heat transfer interactions, in which case the heat transfer is confined to the basal-plane (in-plane) direction of the graphene. On the other hand thermal transport in occurs in three dimensions for a system consisting of a supported graphene and its surroundings (i.e. substrate and atmosphere), complicating the assessment of the basal-plane thermal conductivity of graphene, since heat is transferred across the graphene-substrate interface (out-of-plane, or cross-plane direction) as well as within the graphene (in-plane). Comparison of heat transfer in suspended graphene and supported graphene is depicted in Figure 2.1.

Three dimensional heat transfer in a supported graphene complicates the derivation of a heat transfer model for deducing the thermal conductivity of graphene. To determine the thermal conductivity of graphene, thermal properties of substrate, and the graphene-substrate interface should be given as a prerequisite, so as to establish the relation between experimentally measured

temperature (dependent variable) and the supplied heat (controlled variable), where thermal conductivity of graphene serves as a fitting parameter. As will be shown in the following sections, the uncertainty in thermal boundary conductance (TBC) of graphene-substrate interface ( $G_b$ ) as well as temperature dependence of thermal conductivity of substrate ( $k_{\text{sub}}$ ) significantly affect the reliability of the thermal conductivity measurement.

To circumvent this problem, we have adopted an extremely thin substrate for the supported graphene sample. Reduction of substrate thickness enhances the reliability of the thermal conductivity measurement by minimizing the heat that is transferred through the substrate, as schematically shown in Figure 2.2. By minimizing the graphene-to-substrate heat dissipation, it will be shown that effect of uncertainty in  $G_b$  and temperature dependence  $k_{\text{sub}}$  on measured thermal conductivity becomes negligible, improving the measurement reliability as a result.

Also, we derive a fully three-dimensional finite difference temperature model for numerical analysis of heat transfer in optothermal Raman measurement for a supported graphene sample, rather than relying on a two-dimensional heat transfer model using a constant-value cross-plane heat transfer coefficient ( $g$ ) for approximation, which has been prevalent up to this date. Limitations of two-dimensional heat transfer model in evaluating the thermal conductivity of supported graphene will be discussed, stressing the necessity of a fully 3D numerical simulation.

## 2.2 Optothermal Raman technique

Optothermal Raman technique for measuring the thermal conductivity of graphene (Fig. 2.3 (a)) was devised by Balandin et al. (2008), becoming the dominant method for experimental studies in graphene thermal transport (Cai et al., 2010; Faugeras et al., 2010, Chen et al., 2011; Lee et al., 2011; Chen et al., 2012a; Chen et al., 2012b; Lee et al., 2017). Procedure of optothermal Raman method is depicted in Fig. 2.3 (b). Heat is provided to the sample by controlled laser heating, where the amount of supplied heat is determined from the product between the laser power and the optical absorbance of graphene ( $\alpha_g$ ), where the optical reflectance is known to be negligible for a suspended graphene (Nair et al., 2008). As the temperature of graphene increases as a result of heating, the positions of Raman G and 2D peaks (refer to Section 3.3.4 for more details) of graphene shift to lower wavenumbers (red-shift). Since a one-to-one correspondence exists between temperature rise of graphene ( $\Delta T$ ) and the shift of Raman peak position ( $\Delta\omega$ ), temperature of graphene could be measured. The measured temperature rise of graphene is expressed as a function of laser power, optical absorbance, and thermal conductivity of graphene, which is determined as a fitting parameter.

The advantage of optothermal Raman technique is in its simplicity in sample preparation and implementation of the experiment, leading to reduction in cost

and time. Compared with the optothermal Raman technique, the micro-bridge resistance method (Seol et al., 2010; Bae et al., 2013), despite its superior measurement accuracy, requires a series of expensive lithography process to fabricate the experimental specimen. Complicated sample preparation procedure not only increases the experiment cost, but also results in contamination of graphene due to repeated coating of polymeric layers, which could lead to unexpected reduction of the thermal conductivity of graphene (Pettes et al., 2011; Xu et al., 2014).

However, the optothermal Raman technique was mostly limited to suspended graphene thermal conductivity measurements up to this date. Previous study shows that for a supported graphene, measurement error of optothermal Raman technique becomes unacceptably large (86% ~ 175%, Cai et al., 2010), compared to that for a suspended graphene (10% ~ 30%). As discussed in the previous section, primary cause for this large uncertainty is the large amount of heat leakage from graphene to the substrate, which is difficult to quantify. For a given amount of laser heating, temperature rise of a supported graphene on thick graphene is significantly smaller than that of a suspended graphene, since only a small portion of the supplied heat is used to heat the temperature of graphene rather than dissipated through the substrate.

## **2.3 Sample design**

To deny the role of the substrate as a heat sink, we deploy a commercially available 8-nm-thick SiO<sub>2</sub> TEM grid (silicon dioxide support film, Ted Pella Inc.). The lateral size of each SiO<sub>2</sub> membrane is 70  $\mu\text{m}$   $\times$  70  $\mu\text{m}$ , fringed by a 200-nm-thick silicon nitride (Si<sub>x</sub>N<sub>y</sub>) frame. Monolayer CVD graphene was transferred to the substrate, as will be discussed in Section 3.1 and 3.2. The overall schematic of optothermal Raman measurement using an 8-nm-thick SiO<sub>2</sub> substrate is shown in Figure 2.4.

## 2.4 Governing equations and boundary conditions

Heat transfer in a supported graphene is studied under the assumption of Fourier's Law, where thermal conductivity  $k$  is defined as

$$k = \frac{\mathbf{q}''}{\nabla T} \quad (2.1)$$

where  $\mathbf{q}''$  is the heat flux (W/m<sup>2</sup>) and  $\nabla T$  is the temperature gradient in the real space. Since the laser beam is axisymmetric with respect to the line of laser-incidence, cylindrical coordinate system ( $r, \theta, z$ ) is best suited to modeling the heat transport for this specific case.

### 2.4.1 Heat transfer model in 2D

A previous study using optothermal Raman technique for supported graphene measurement (Cai et al., 2010) applied a two-dimensional heat transfer model to derive the thermal conductivity from measured temperature. The governing equation is given as

$$k_g t_g \frac{1}{r} \frac{\partial}{\partial r} \left( r \frac{\partial T}{\partial r} \right) - g [T - T_\infty] + \mathbf{q}''_{\text{laser}} - \mathbf{q}''_{\text{convection}} = 0 \quad (2.2)$$

where  $k_g$  is the thermal conductivity of graphene,  $t_g$  is the thickness of graphene (0.334 nm),  $T = T(r)$  is the temperature of the graphene,  $g$  is the lumped cross-plane heat transfer coefficient with as regards the graphene-substrate heat dissipation,  $\mathbf{q}''_{\text{laser}}$  is the absorbed portion of the heat flux due to incident laser beam, and  $\mathbf{q}''_{\text{convection}}$  is the heat flux due to natural convection from graphene to atmosphere. Since both  $k_g$  and  $g$  are unknown parameters, optothermal Raman measurement has been performed for two lenses (50x and 100x) with different  $\mathbf{q}''_{\text{laser}}$  terms in Eq. (2.2), thus resulting in two independent equations and two measured temperatures, allowing for simultaneous evaluation of  $k_g$  and  $g$ .

While being simple to implement, 2D heat transfer model with constant value approximation of  $g$  not only leads to large amount of measurement error, but also results in a systematic bias as to the evaluated thermal conductivity of supported graphene, as will be discussed in the following sections. Therefore, a fully three-

dimensional heat transfer model simultaneously accounting for the spatial temperature distribution of the substrate as well as the graphene is required to determine the thermal conductivity correctly and accurately.

#### 2.4.2 Heat transfer model in 3D

As depicted in Figure 2.5, central axis of the incident laser is set to  $r = 0$ , bottom of the substrate is set to  $z = 0$ , and top of the substrate which is in contact with the supported graphene is set to  $z = 8$  nm. The governing equation for the heat conduction within the substrate is expressed as

$$\frac{1}{r} \frac{\partial}{\partial r} \left( r \frac{\partial T_{\text{sub}}}{\partial r} \right) + \frac{\partial^2 T_{\text{sub}}}{\partial z^2} = 0 \quad (2.3)$$

where  $T_{\text{sub}}(r, z)$  is the temperature distribution of the substrate. The governing equation for the graphene is

$$k_g t_g \frac{1}{r} \frac{\partial}{\partial r} \left( r \frac{\partial T_g}{\partial r} \right) - k_{\text{sub}} \frac{\partial T_{\text{sub}}}{\partial z} \Big|_{z=Z} + \mathbf{q}_{\text{laser}}'' - \mathbf{q}_{\text{convection}}'' = 0 \quad (2.4)$$

where  $T_g(r)$  is the temperature of graphene. Here,  $\mathbf{q}_{\text{laser}}''$  is given as

$$\mathbf{q}''_{\text{laser}} = \alpha q''_0 \exp\left(-\frac{2r^2}{r_0^2}\right) \quad (2.5)$$

where  $q''_0$  is the maximum intensity and  $r_0$  is the beam radius for the incident Gaussian laser beam. Gaussian beam radius is given as

$$r_0 = \frac{\lambda}{\pi NA} \quad (2.6)$$

where  $NA = 0.75$  is the numerical aperture of the objective lens (100x) used for focusing the laser beam.

While the heat loss due to natural convection at the upper surface of heated plate is known to correspond to convection heat transfer coefficient ( $h$ ) of several  $\text{W/m}^2 \text{ K}$  at larger scales, orders-of-magnitude increase in convection heat transfer coefficient has been observed for samples that have micro and nanoscale heated zone size (Hu et al., 2008; Kim and King, 2009; Pulavarthy et al., 2014). Since Gaussian beam size is 218 nm for the incident laser, we use the convection heat transfer coefficient value of  $2.9 \times 10^4 \text{ W/m}^2 \text{ K}$  that has been obtained from optothermal Raman measurement in vacuum and atmospheric pressures (Chen et al., 2011). As a result, convection loss term in Eq. (2.4) is expressed as

$$\mathbf{q}''_{\text{convection}} = h(T_g - T_\infty) \quad (2.7)$$



where  $T_\infty = 300$  K is the ambient temperature.

At the center of the laser beam axis (i.e.  $r = 0$ ), adiabatic boundary condition applies due to axisymmetry of heating.

$$\left. \frac{\partial T_g}{\partial r} \right|_{r=0} = \left. \frac{\partial T_{\text{sub}}}{\partial r} \right|_{r=0} = 0 \quad (2.8)$$

If the size of the specimen is sufficiently large, temperature of the graphene and the substrate decreases at the far end of the sample with respect to the radial axis ( $r = R$ ), approaching room temperature, resulting in a constant temperature boundary condition.

$$T_g(R) = T_{\text{sub}}(R, z) = T_\infty \quad (2.9)$$

At the bottom of the substrate ( $z = 0$ ), the boundary condition is expressed as

$$-K_{\text{sub}} \left. \frac{\partial T_{\text{sub}}}{\partial z} \right|_{z=0} - h [T_{\text{sub}}(r, 0) - T_\infty] = 0 \quad (2.10)$$

where  $z$ -directional heat flux between substrate and convection is balanced. At the graphene-substrate interface ( $z = 8$  nm), another boundary condition is given as

$$-K_{\text{sub}} \left. \frac{\partial T_{\text{sub}}}{\partial z} \right|_{z=Z} - G_b [T_g - T_{\text{sub}}(r, Z)] = 0 \quad (2.11)$$

where  $G_b$  is the thermal boundary conductance between graphene and  $\text{SiO}_2$  substrate. System of two governing linear partial differential equations, Eq. (2.3) and Eq. (2.4), and six boundary conditions, Eq. (2.8) ~ (2.11), two variables,  $T_g$  and  $T_{\text{sub}}$ , can be uniquely determined for a given value of  $k_g$  and  $\mathbf{q}''_{\text{laser}}(r)$ .

### 2.4.3 Finite difference method and numerical analysis

Finite difference energy balance method has been applied to solve the heat transfer model for discretized control volumes in the cylindrical coordinate system. Nodal points and their corresponding indices for  $r$ - and  $z$ - coordinates are given as Figure 2.6. Non-uniform graded grid was deployed at the nodes in the vicinity of the center axis, where spatial temperature change is rapid due to concentrated laser heating. Gauss-Seidel method was applied for successive iteration until convergence criterion of  $10^{-9}$  was met. See Appendix A.1 for details in numerical implementation using MATLAB for a sample case where  $k_g = 1000 \text{ W/m K}$  and  $G_b = 25 \text{ MW/m}^2 \text{ K}$  are assumed. Radius ( $R$ ) of the spatial domain was set as  $20 \text{ }\mu\text{m}$ , which is considered adequately large to satisfy the constant temperature boundary condition at  $r = R$ , Eq. (2.9). Spatial temperature distribution for the supported graphene is shown in Figure 2.7, where it is clearly demonstrated that temperature approaches the room temperature at  $r > 10 \text{ }\mu\text{m}$  for a typical case

where  $k_g = 1000$  W/m K and laser power of 2.48 mW is assumed, where laser power  $P_L$  is defined as

$$P_L = 2\pi q_0'' \int r \exp(-2r^2/r_0^2) dr \quad (2.12)$$

## 2.5 Improvement in measurement accuracy

### 2.5.1 Inadequacy of the 2D heat transfer model

To compare the effect of applying a 2D (Eq. (2.2)) and 3D (Eq. (2.3) and (2.4)) heat transfer model, ‘true’ thermal conductivity of supported graphene is assumed as 1000 W/m K, incident laser power is given as 5.0 mW, and true measured temperatures for 100x and 50x lenses are computed by the 3D heat transfer model. The measured temperatures corresponding to 100x and 50x lenses obtained by the 3D model and their counterparts as to the 2D heat transfer model (Eq. (2.2)) are applied to evaluate the measured  $k_g$ , which in turn will be compared with the ‘true’  $k_g$ .

For a given incident laser power of 5.0 mW and graphene thermal conductivity of 1000 W/m K, measured temperature of a supported graphene on a semi-infinite-thick SiO<sub>2</sub> substrate using the 3D heat transfer model is computed as 360.77 K and 379.39 K for 50x and 100x lenses, respectively. Figure 2.8 shows the  $k_g$  and  $g$  pairs in 2D heat transfer model that satisfy the measured temperatures for 50x and 100x lenses, respectively. The  $k_g$  and  $g$  pair that satisfy the measured

temperatures for both 50x and 100x lenses are  $k_g = 1430$  W/m K and  $g = 1.2$  MW/m<sup>2</sup> K, respectively. Compared to the ‘true’ supported thermal conductivity value of 1000 W/m K, the thermal conductivity determined by the 2D model (1430 W/m K) is overestimated by 43%, indicating a significant systematic error originating from the constant value approximation of interfacial heat transfer coefficient  $g$ .

True value of  $g$ , which is a spatial variable of  $r$ , defined as

$$g(r) = \frac{q_z''(r)}{T_g(r) - T_\infty} \quad (2.13)$$

where  $q_z''$  is the cross-plane ( $z$ -direction) component of the heat flux vector, is computed by the 3D heat transfer model for comparison. As shown in Figure 2.9, it is noted that 2D approximation underestimates the  $g(r)$  value near the heating zone ( $r < 218$  nm), resulting in an overestimation of  $k_g$  to compensate for the underestimated graphene-substrate heat dissipation, for a given measured temperature.

### 2.5.2 Advantages of the thin SiO<sub>2</sub> substrate

For quantitative comparison of measurement accuracy between the revised method (8-nm-thick SiO<sub>2</sub> substrate) and the conventional method (semi-infinite-thick SiO<sub>2</sub> substrate), thermal conductivity of the substrate ( $k_{\text{SiO}_2}$ ) and thermal

boundary conductance of the graphene-substrate interface ( $G_b$ ) has been varied. We show that the  $k_g$  value that is deduced from a given measured temperature,  $T_m$ , for the thin substrate is negligibly affected by the variances in  $G_b$  and  $k_{SiO_2}$ , while  $k_g$  derived from the thick substrate is strongly dependent on, i.e. easily distorted by the choice of input parameters,  $G_b$  and  $k_{SiO_2}$ . Unless otherwise specified,  $T_m$  was set to 400 K and the corresponding laser powers for the thin substrate and the thick substrate were  $P_L = 2.49$  mW and 6.30 mW, respectively. The thickness of the substrate were 8 nm and 10000 nm for the thin substrate and the thick  $SiO_2$  substrate.

Thermal boundary conductance at the graphene- $SiO_2$  interface had been measured experimentally by numerous groups, and it is noticed that the  $G_b$  values that has been reported varies over a wide range, from 266 W/m<sup>2</sup> K using modified a modified optothermal Raman technique (Tang et al., 2014) to 50 MW/m<sup>2</sup> K using a pump/probe technique (Mak et al., 2010). It is also worthy of note that the measured  $G_b$  value showed a large dispersion (from 20 MW/m<sup>2</sup> K to 110 MW/m<sup>2</sup> K) even for the measurements conducted by the same group and for the same instance, alluding to the variable nature of the interface rather than the reliability of the measurement technique (Mak et al., 2010). As to the 3D heat transfer numerical simulation for determining the thermal conductivity of optothermal Raman measurements (see Chapter 4), we used the theoretically predicted value of  $G_b = 25$  MW/m<sup>2</sup> K using the diffusive mismatch model (Persson et al., 2010) unless otherwise specified.

The evaluation of  $k_g$  from the measured temperature,  $T_m$ , defined as

$$T_m = \frac{\int rT(r)\exp(-2r^2/r_0^2)dr}{\int r\exp(-2r^2/r_0^2)dr} \quad (2.14)$$

is affected by the choice of the input parameter  $G_b$ , through the heat flux boundary condition at the graphene interface, Eq. (2.11). The extent to which the evaluated  $k_g$  depends on  $G_b$  is shown in Figure 2.10, where it could be clearly seen that 8-nm-thick substrate offers a reliable measurement of  $k_g$  compared to the 10000-nm-thick substrate, irrespective of the variation as to the input parameter  $G_b$ , available knowledge of which is insufficient. The result is in good agreement with the physical intuition. Since cross-plane heat flux at the graphene-SiO<sub>2</sub> interface of the thin substrate case is limited by the significantly higher thermal resistance of the extremely thin SiO<sub>2</sub> substrate that has orders of magnitude lower thermal conductivity compared to that of the graphene. In-plane thermal sheet resistance,  $R_{s,th}$ , analogous to the electrical sheet resistance, is a useful concept to compare the relative heat-conducting capacity of the membrane, defined as

$$R_{s,th} = \frac{1}{kt} \quad (2.15)$$

where  $k$  and  $t$  are thermal conductivity and thickness of the sheet, respectively. Since  $R_{s,th}$  of a monolayer graphene ( $k_g = 1000$  W/m K,  $t_g = 0.334$  nm), 8-nm-

thick substrate ( $k_{\text{SiO}_2} = 1.34 \text{ W/m K}$ ,  $t_{\text{sub}} = 8 \text{ nm}$ ), and 10000-nm-thick substrate ( $k_{\text{SiO}_2} = 1.34 \text{ W/m K}$ ,  $t_{\text{sub}} = 10000 \text{ nm}$ ) is  $2.99 \times 10^6 \text{ K/W}$ ,  $9.33 \times 10^7 \text{ K/W}$ , and  $7.46 \times 10^4 \text{ K/W}$ , respectively, implying that graphene is the dominant path of the heat transfer for the 8-nm-thick substrate case, while thick  $\text{SiO}_2$  substrate has orders-of-magnitude effective conduction path compared to that of graphene for the 10000-nm-thick substrate case.

Similar analysis was conducted with respect to the thermal conductivity of the  $\text{SiO}_2$  ( $k_{\text{SiO}_2}$ ). Although thermal properties of thermally grown amorphous  $\text{SiO}_2$  is well known, temperature dependence of  $k_{\text{SiO}_2}$  is non-negligible, ranging from  $1.34 \text{ W/m K}$  at  $300 \text{ K}$  to  $1.75 \text{ W/m K}$  at  $600 \text{ K}$ . Considering the typical sample temperature range ( $300 \text{ K}$  to  $600 \text{ K}$  or more) of the optothermal Raman measurements supported graphene, it is deduced from Figure 2.11 that for the 10000-nm-thick substrate case, over-complicated numerical analysis where  $k_{\text{SiO}_2}$  dependence on  $T$  is accounted for is needed to correctly evaluate the  $k_g$ , whereas for the 8-nm-thick case, any value of  $k_{\text{SiO}_2}$  between  $0.5$  to  $2.0 \text{ W/m K}$  will not affect the evaluated  $k_g$  significantly.

Another advantage of the thin substrate is the sensitivity of the measured  $T_m$  on  $k_g$ . From Figure 2.12, it is seen that for a given measured temperature  $T_m = 335 \text{ K}$ , and its measurement error  $\delta T_m$ , optothermal Raman measurement for the thin substrate could determine the  $k_g$  more accurately (smaller  $\delta k_g$ ) due to larger  $\partial T_m / \partial k_g$ .

Propagated measurement uncertainty of  $k_g$  is expressed as

$$\delta k_g = \sqrt{\sum_i \left( \frac{\partial k_g}{\partial X_i} \delta X_i \right)^2} \quad (2.16)$$

where  $X_i$  is either a variable or a parameter that is related to  $k_g$  with a certain amount of uncertainty  $\delta X_i$ . For a given amount of  $\delta X_i$ , which is often related to the limitation of the equipment rather than the experiment scheme, lower  $\partial k_g / \partial X_i$  results in lower  $\delta k_g$ , therefore better accuracy. Comparison between thin substrate and thick substrate is summarized in Table 2.1, where advantage of the 8-nm substrate over the thick substrate in terms of measurement accuracy is clearly seen.

## 2.6 Conclusion

For optothermal Raman measurement of supported graphene thermal conductivity, an experiment design using a substrate of an ultra-thin (8 nm) SiO<sub>2</sub> has been developed, in order to minimize the transfer of heat via the substrate. To determine the thermal conductivity of graphene ( $k_g$ ) from the measured temperature using optothermal Raman technique, a heat transfer model specifying the quantitative relation between the variables and parameters is required. It has been demonstrated that the prevalent 2D heat transfer approximation using a constant value cross-plane heat transfer coefficient ( $g$ ) results in a significant overestimation of  $k_g$ , stressing the importance of a 3D heat transfer model where



spatial temperature distribution of graphene as well substrate is fully accounted for. Numerical analysis based on finite difference method and Gauss-Seidel iteration has been performed over typical range optothermal Raman measurement conditions, demonstrating the superior measurement accuracy of thin substrate over thick substrate.

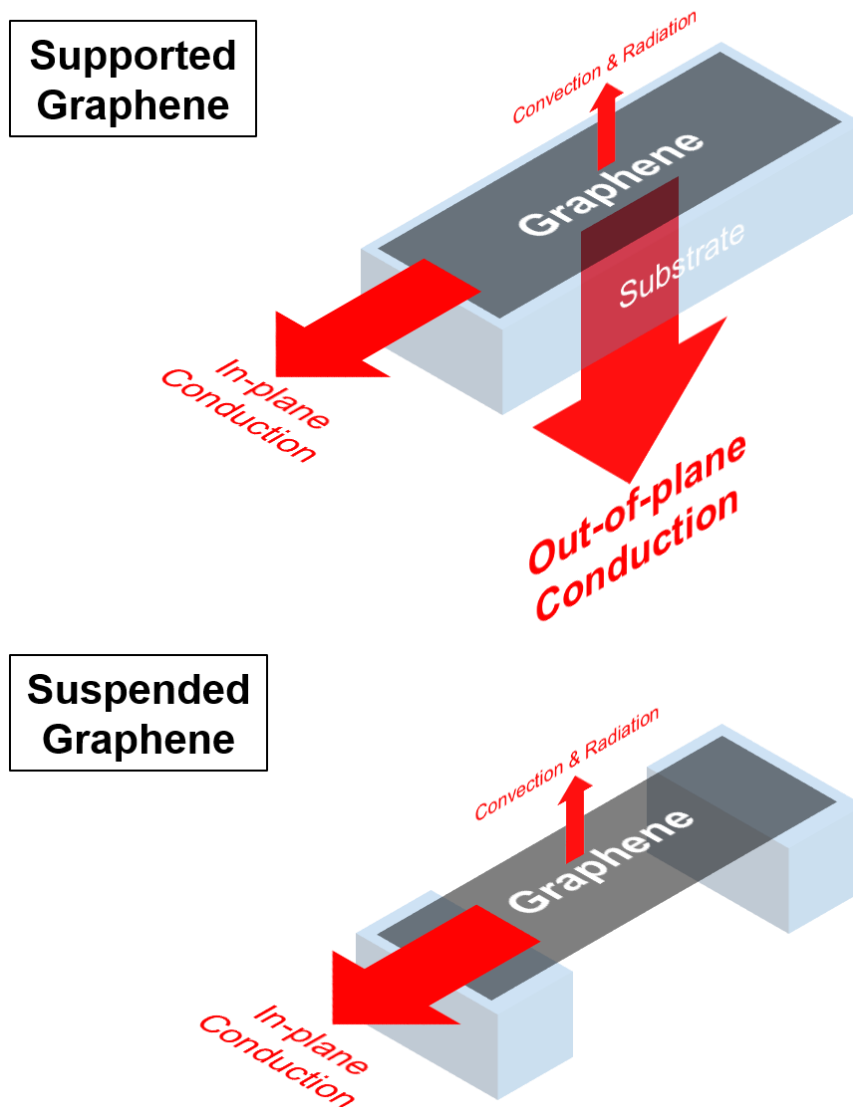


Figure 2.1 Schematic comparison of heat transfer in supported graphene (above) and suspended graphene (below).

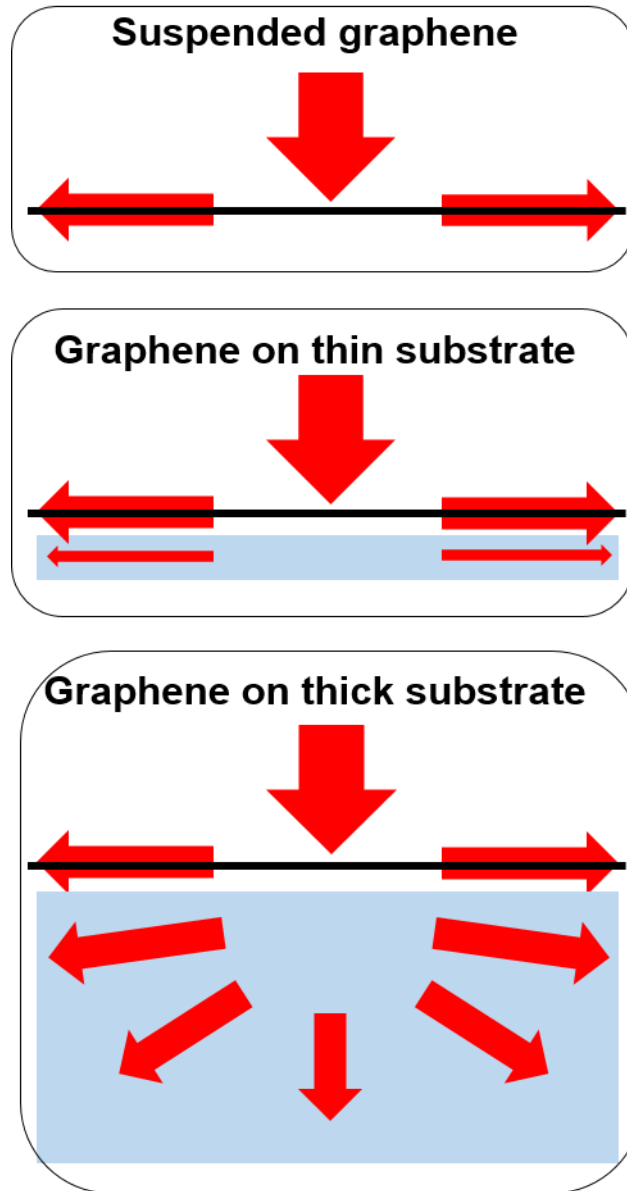


Figure 2.2 Minimization of heat dissipation through the substrate for a supported graphene could be achieved by reducing the thickness of the substrate, resulting in a heat flow similar to that of a suspended graphene.

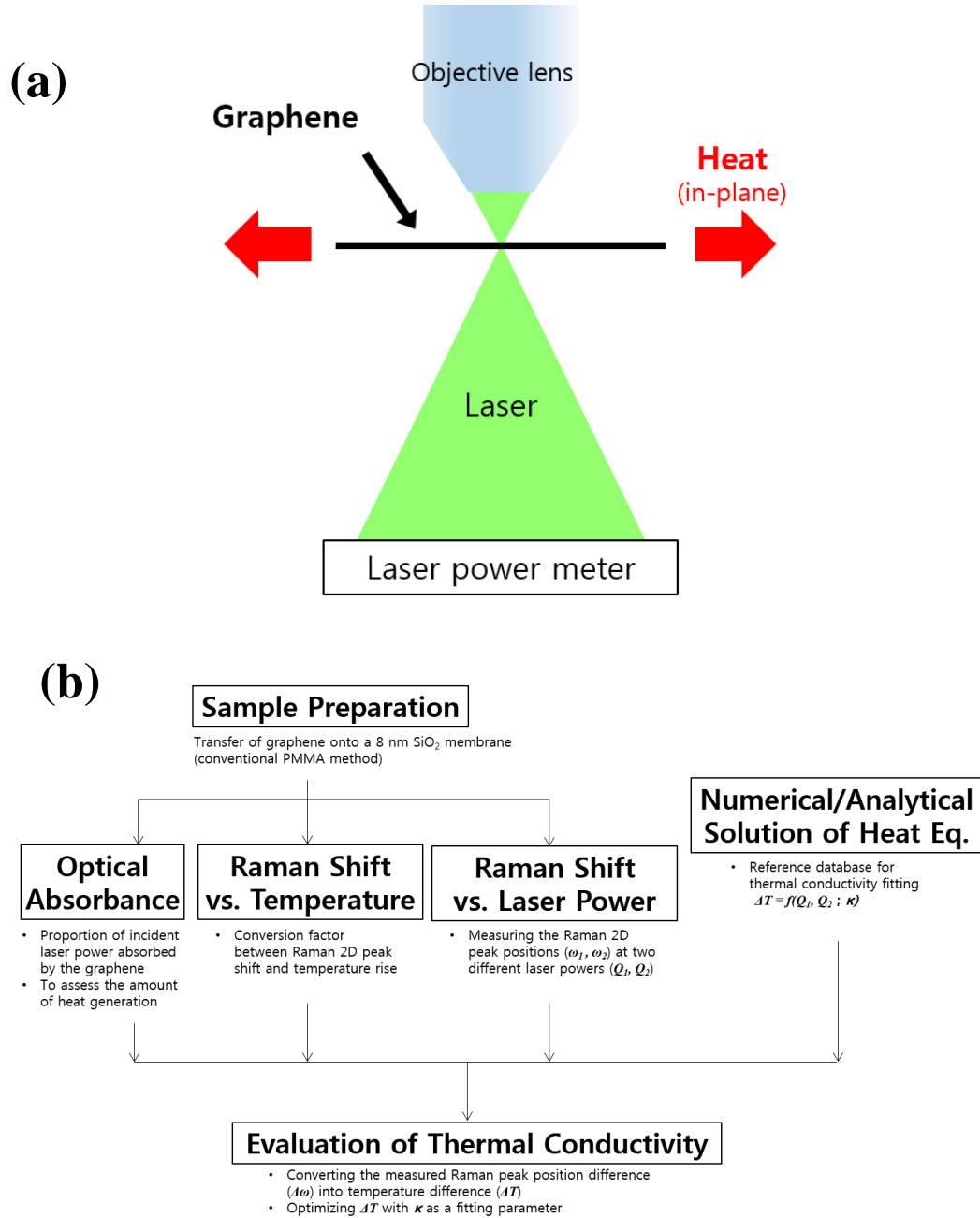
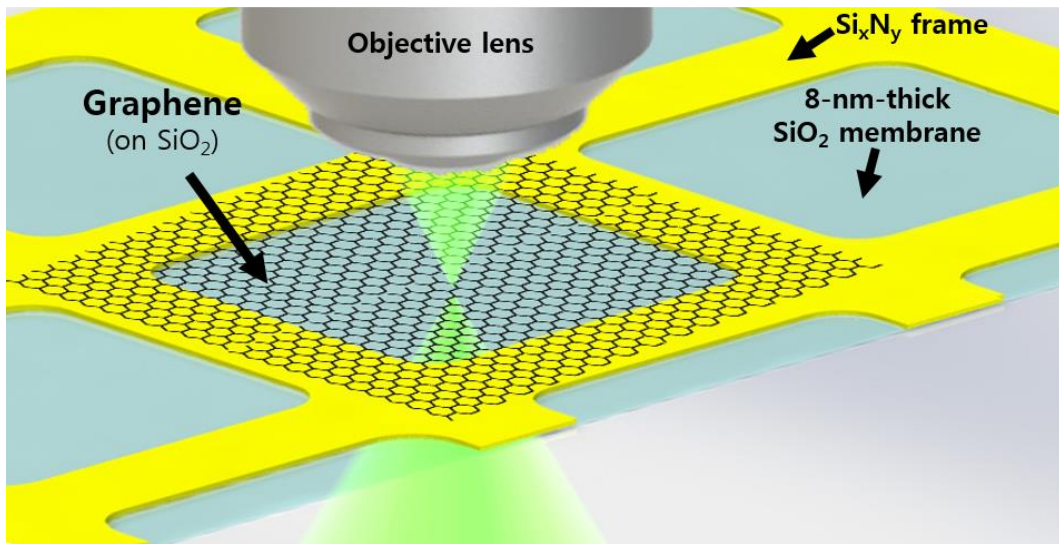


Figure 2.3 (a) Schematic representation of an optothermal Raman measurement for a suspended membrane (graphene). (b) Procedures of an optothermal Raman measurement.

**(a)**



**(b)**

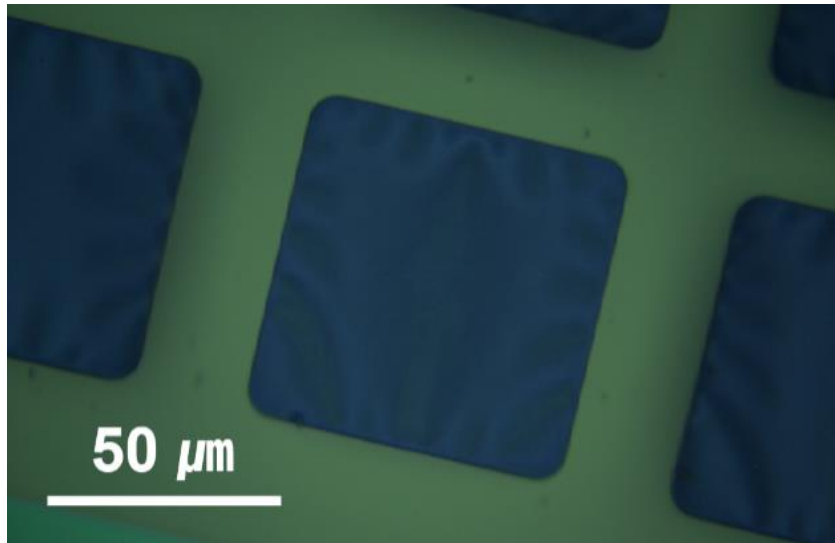


Figure 2.4 (a) Specimen using 8-nm-thick  $\text{SiO}_2$  TEM grid as the substrate, (b) and its optical image.

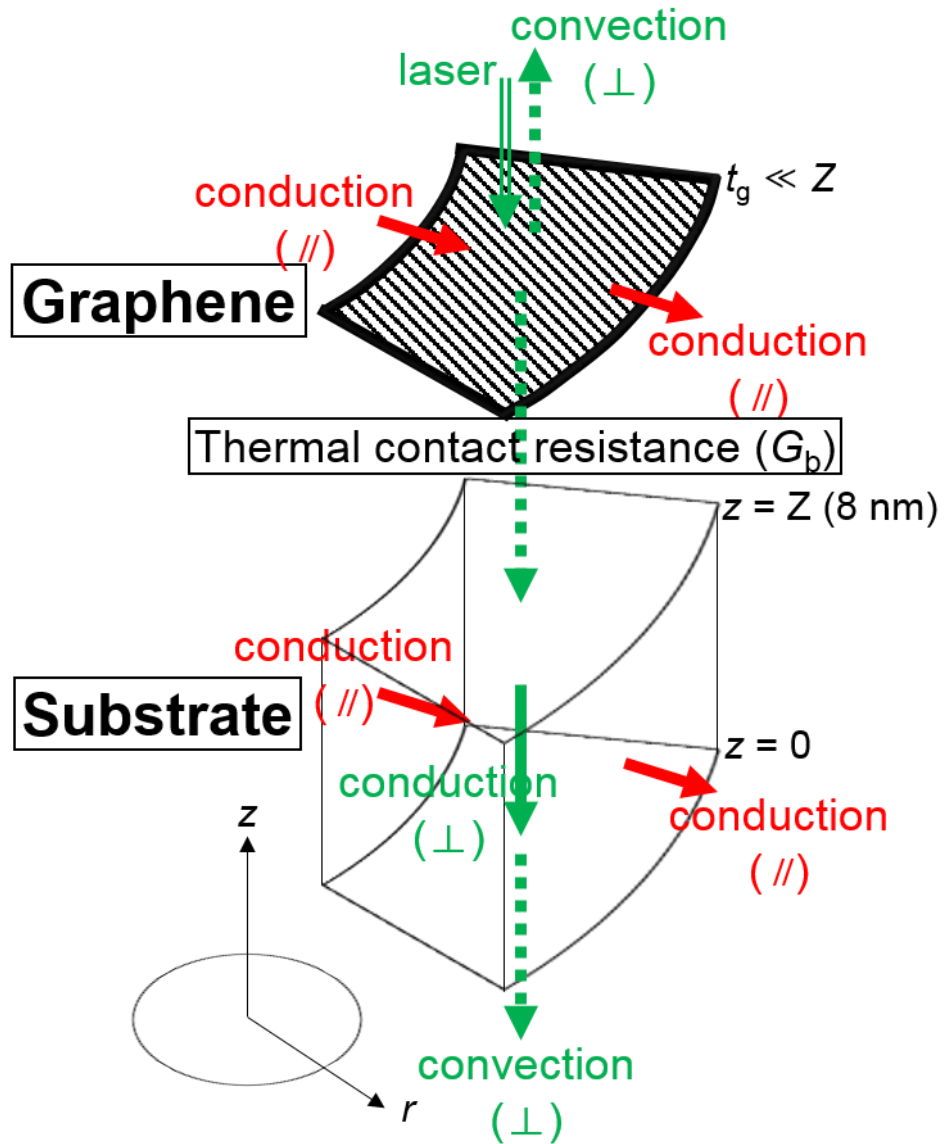


Figure 2.5 Heat transfer in a supported graphene sample for an optothermal Raman measurement in cylindrical coordinate system. ‘ $//$ ’ and ‘ $\perp$ ’ represent the in-plane and out-of-plane directions with respect to the supported graphene, respectively.

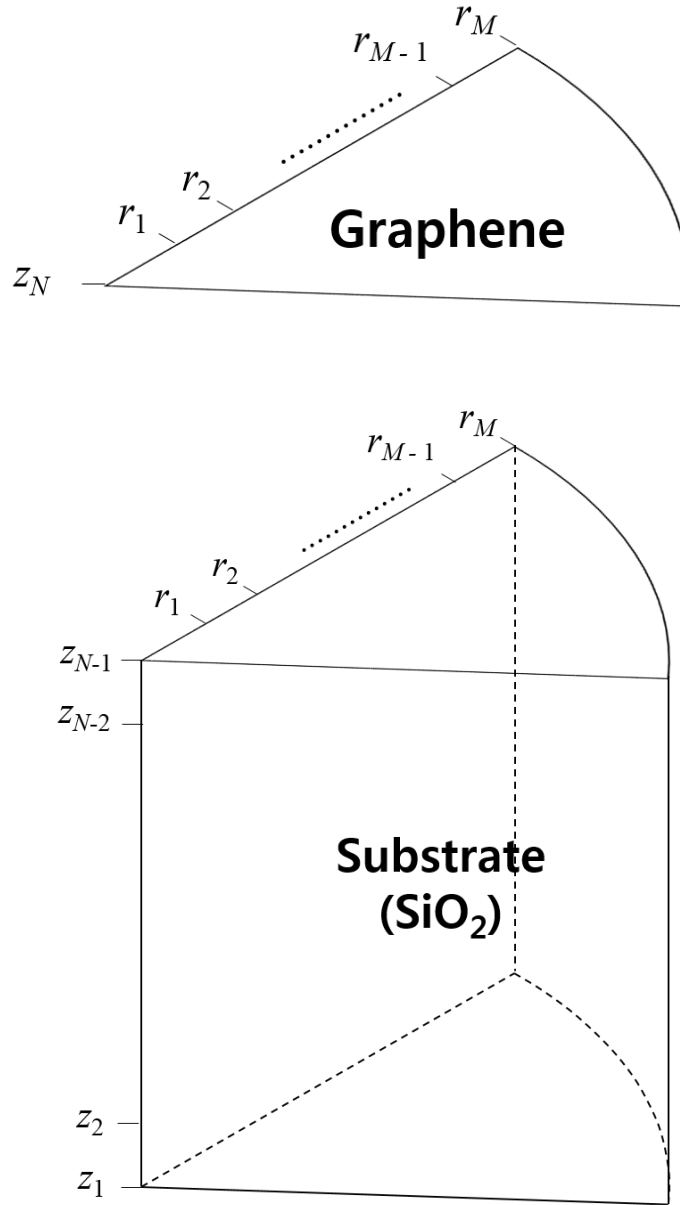


Figure 2.6 Discretized  $r$  and  $z$  for the supported graphene (above) and the substrate (below) for numerical analysis.

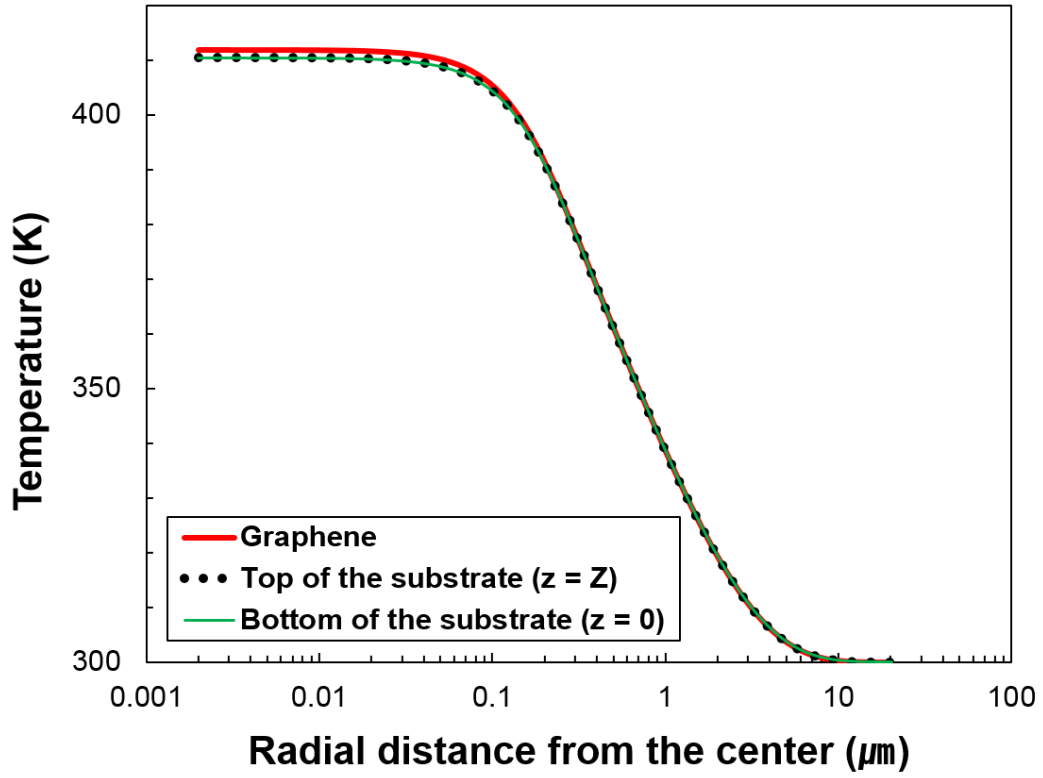


Figure 2.7 Spatial temperature distribution obtained using Eqs. (2.3) ~ (2.11) for a supported graphene with 8-nm-thick substrate, assuming  $k_g = 1000$  W/m K,  $k_{\text{sub}} = 1.38$  W/m K,  $G_b = 25$  MW/m<sup>2</sup> K, and the incident laser power of 2.49 mW. It is shown that the temperature difference along the cross-plane direction ( $\perp$ ) is negligible to that along the in-plane direction ( $\parallel$ ). Also it is demonstrated that the large lateral size of our supported graphene (70  $\mu\text{m}$ ) justifies imposing a constant temperature ( $T_\infty$ ) boundary condition at  $r = R$  in evaluating the thermal conductivity of the graphene ( $k_g$ ).



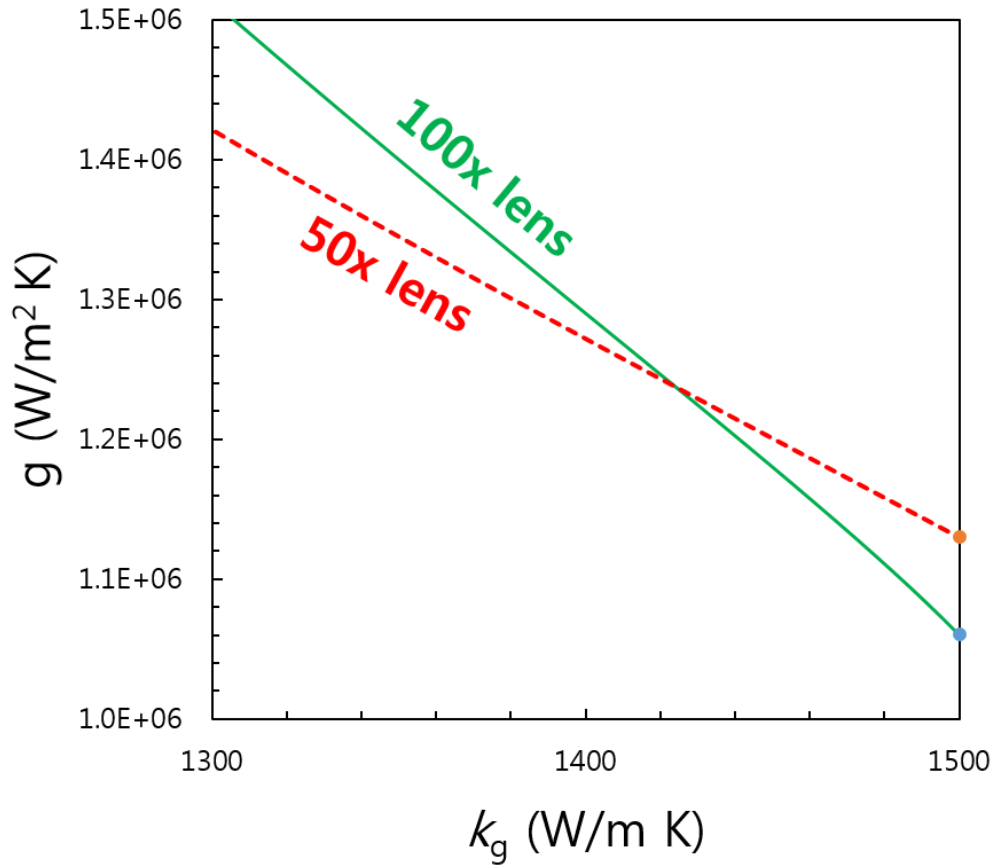


Figure 2.8 Evaluation of thermal conductivity and constant cross-plane heat transfer coefficient using a 2D heat transfer model, Eq. (2.2), and two objective lenses (50x, 100x), where true value of  $k_g$  is assumed as 1000 W/m K. It is clearly seen that the  $k_g$  deduced from the 2D model (1430 W/m K) is significantly overestimated, stressing the importance of a 3D heat transfer model.

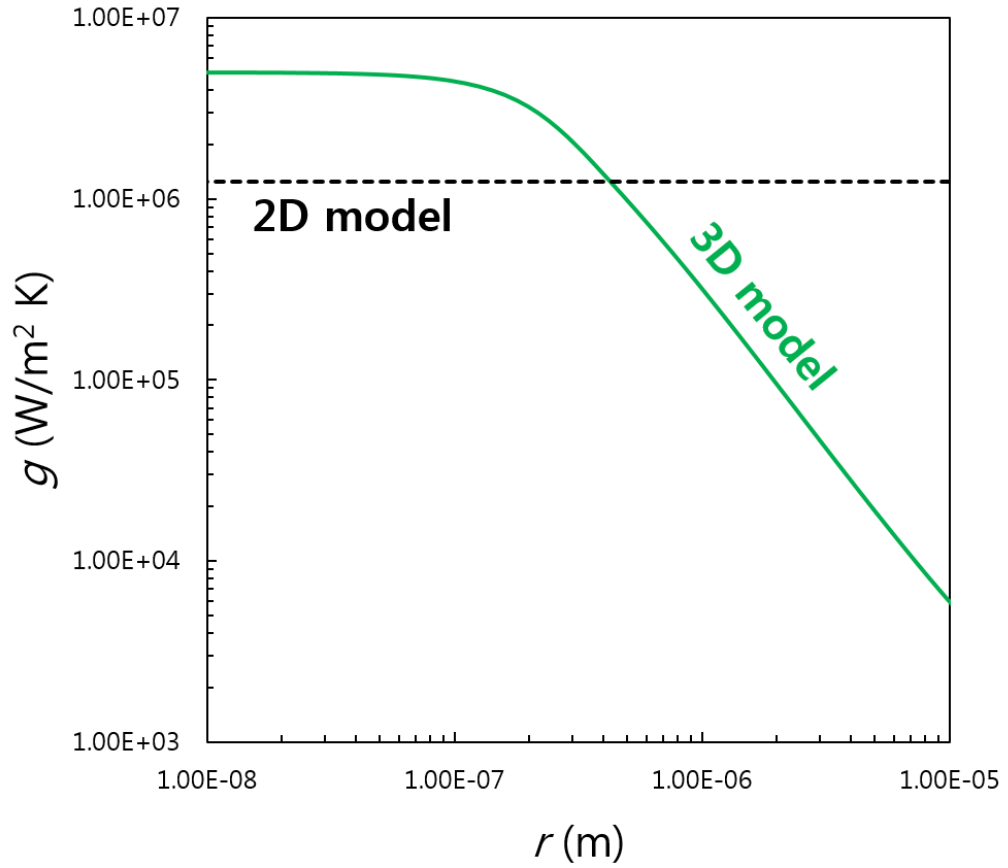


Figure 2.9 Comparison of cross-plane heat transfer coefficient at the graphene-substrate interface ( $g$ ), between 3D heat transfer model and 2D heat transfer model. It is shown that constant-value  $g$  approximation for a 2D model results in an underestimation of  $g$ , which actually is a spatial variable, near the heating zone ( $r < r_0$ ).

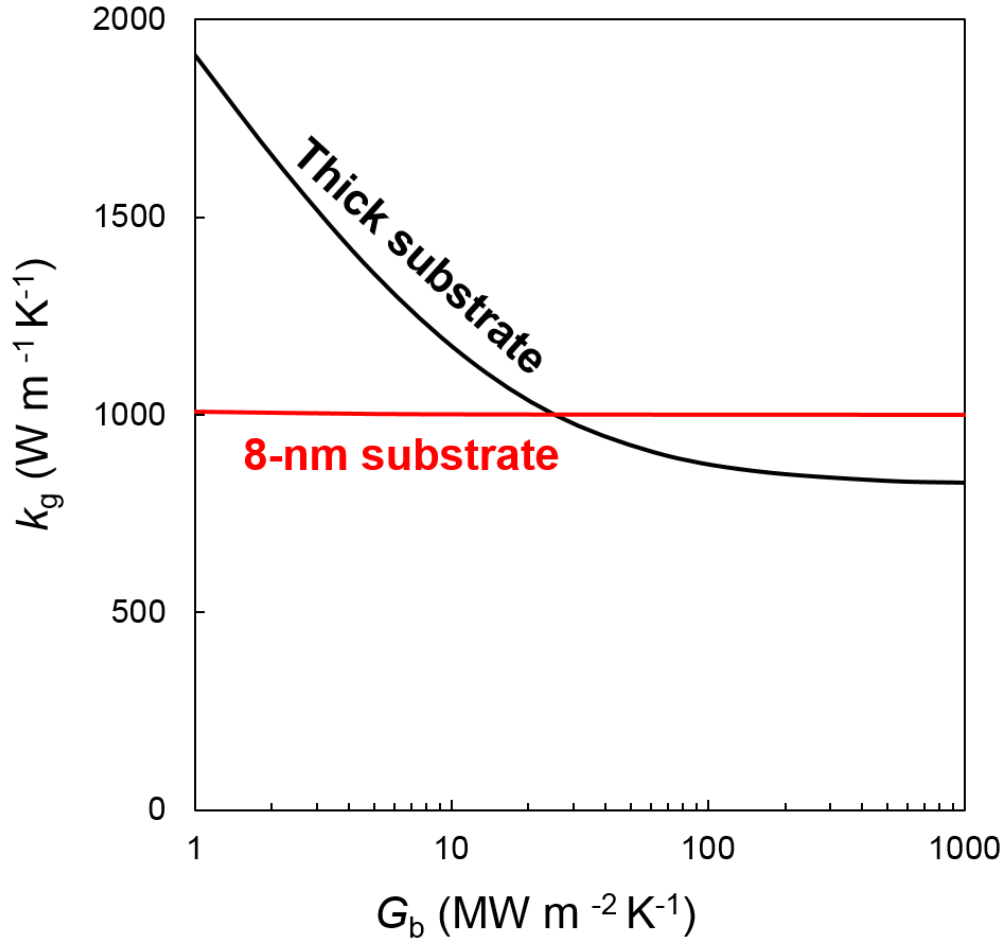


Figure 2.10 Dependence of evaluated  $k_g$  on the variation of  $G_b$  for a thin substrate (8 nm) and a thick substrate (10000 nm). Supported graphene thermal conductivity deviates significantly from the true value (assumed as 1000 W/m K for this case) depending on the  $G_b$  value that is coupled with large uncertainty.

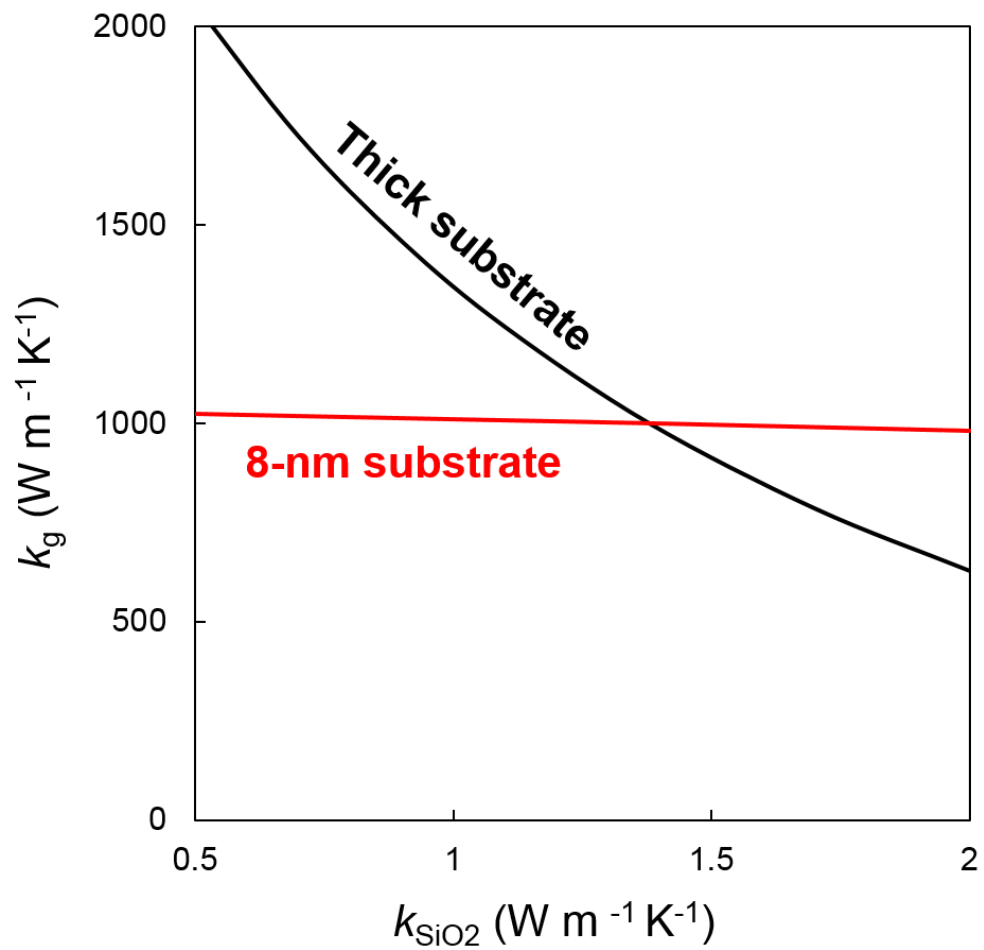


Figure 2.11 Dependence of evaluated  $k_g$  on the variation of  $k_{\text{SiO}_2}$  for a thin substrate (8 nm) and a thick substrate (10000 nm).

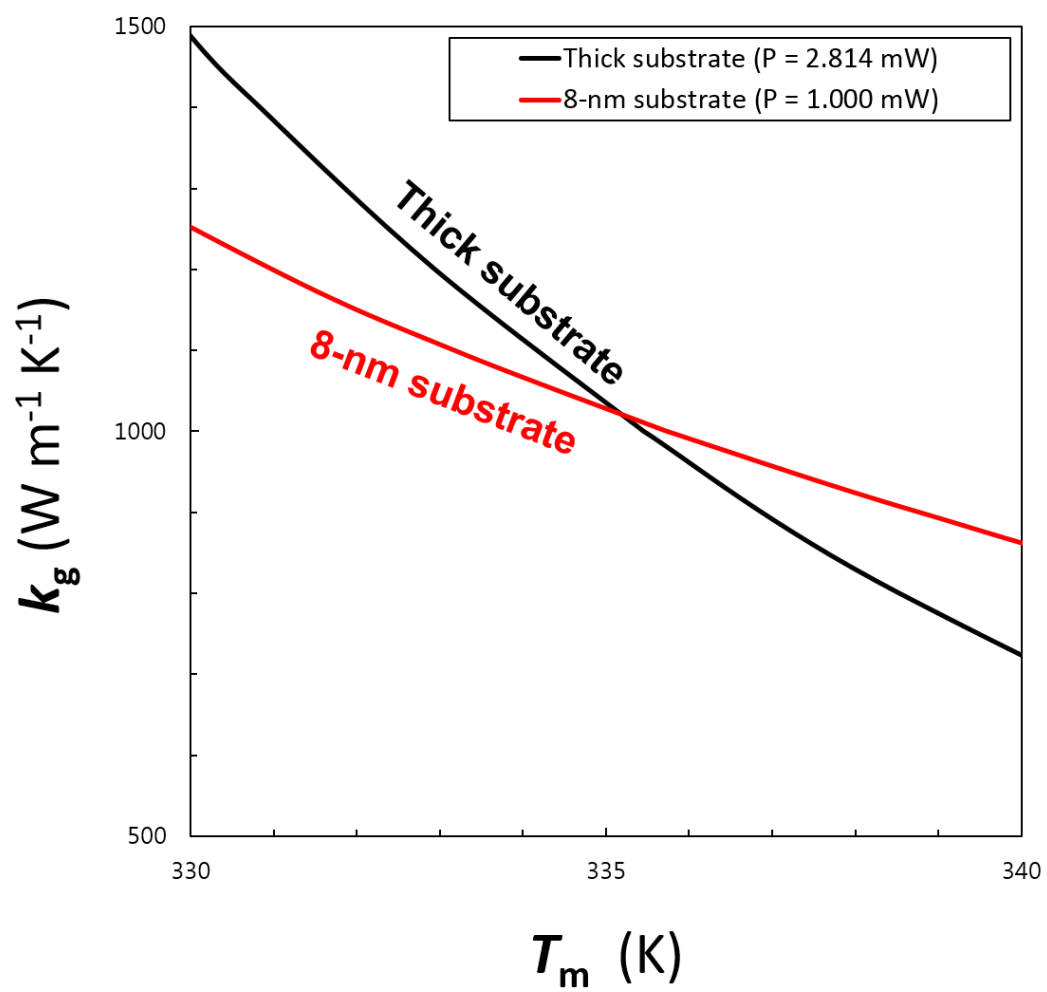


Figure 2.12 Dependence of evaluated  $k_g$  on the measured temperature ( $T_m$ ) for a thin substrate (8 nm) and a thick substrate (10000 nm).

	8-nm SiO <sub>2</sub> substrate [A]	[B/A]	Thick SiO <sub>2</sub> substrate [B]
$\partial k_g / \partial k_{\text{SiO}_2}$	-29.1	<b>26.3</b>	-765
$\partial k_g / \partial G_b$ [W m <sup>-1</sup> K <sup>-1</sup> ] / [MW m <sup>-2</sup> K <sup>-1</sup> ]	-0.018	<b>318</b>	-5.73

Table 2.1 Comparison of  $k_g$  dependence on  $G_b$  and  $k_{\text{SiO}_2}$ , demonstrating the superior accuracy of using a thin substrate.

## **Chapter 3**

### **Sample Preparation and Characterization**

#### **3.1 Synthesis of graphene**

The first experimental demonstration of graphene was achieved by mechanical exfoliation from a bulk pyrolytic graphite (Novoselov et al., 2004), also known as the “Scotch tape method”. However random peeling of graphene by mechanical exfoliation limited the lateral size of the single-atom-thick samples to few micrometers at best, therefore being inappropriate for mass production and practical applications. Various efforts have been made to obtain large-area high-quality graphene with chemical vapor deposition (CVD) method becoming the most prevalent. Comparison of various synthesis methods of graphene are shown in Table 3.1, where it is seen that CVD method is a reasonable compromise between versatility, availability, and quality.

CVD synthesis of graphene requires a precursor gas that contains carbon and a heat source that provides energy for thermal decomposition of hydrocarbon precursor gas. Since thermal decomposition temperatures of carbon sources are very high, imposing a severe limitation on the system, a transition metal catalyst is preferred as the growth bed. Schematic of CVD is described in Figure 3.1. Gas phase reactant is transported to the reaction zone, followed by thermal

decomposition, diffusion, and reaction at the surface of the catalyst, subsequently desorbed and pumped away.

### **3.1.1 Sample requirements and growth mechanism of CVD graphene**

For the current study, a high-quality monolayer-dominant graphene with sample size as large as possible is favorable in order to determine the effect of graphene-substrate interaction, while minimizing the undesired effect on thermal transport including size effect, phonon scattering by defects and/or grain boundaries, and uncertainty in graphene thickness.

While various transition metals including have been tested as the catalyst substrate for graphene synthesis, it has been discovered that copper is best suited for producing monolayer graphene. The distinctive feature of copper in comparison with other transition metals is its negligible carbon solubility. Low carbon solubility of copper leads to graphene growth limited to single-atom-layer thickness originating from the surface reaction only, whereas other transition metals have additional layers of graphene due to precipitation of carbon that originally has been diffused into depth of the bulk catalyst substrate during cooling. Therefore copper offers a significantly better control over the thickness of graphene (i.e. monolayer), while spatially nonuniform multilayered graphene is inevitable for other transition metals such as nickel (Li et al., 2009a). Therefore, we chose copper foil (Alfa Aesar, 99.999% purity, 25- $\mu\text{m}$ -thick) as the catalyst substrate for synthesizing a large-area monolayer graphene sample.



Methane ( $\text{CH}_4$ ) and hydrogen ( $\text{H}_2$ ) was used as reactant gas. The role of methane is to provide hydrocarbon species ( $\text{CH}_x$ ) which agglomerates into  $\text{C}_n\text{H}_y$ , which is thermodynamically favorable, eventually leading to fully grown graphene at the catalyst substrate (Zhang et al., 2011).  $\text{CH}_x$  species are known to move freely on the copper surface due to weak interaction between carbon and copper, therefore the number of nucleation sites for graphene growth are significantly smaller than the number of decomposed  $\text{CH}_4$  molecules, resulting in large single crystalline grain size, as shown in Figure 3.2.

The role of hydrogen, on the other hand, is more complicated than that of  $\text{CH}_4$ . It has been observed that hydrogen serves not only as catalyst for thermal decomposition of  $\text{CH}_4$  during graphene growth, but also as an etching reagent for removing multi-layered graphene (Vlassiouk et al., 2011). Due to the duality of the effect of  $\text{H}_2$ , careful adjustment of the ratio between  $\text{CH}_4$  and  $\text{H}_2$  is necessary, where excessive amount of  $\text{CH}_4$  lead to a spatially-nonuniform defective multi-layered graphene, while excessive supply of  $\text{H}_2$  results in interrupted monolayer graphene or isolated graphene islands (Lewis et al., 2013).

Optimization of the ratio between  $\text{CH}_4$  and  $\text{H}_2$  as well as their partial pressures not only important for thickness control of graphene, but also affects the nucleation density of graphene growth, and eventually the resulting grain size. A study based on the kinetic model of graphene growth has revealed that nucleation density, which is inversely proportional to the grain size, is a function of  $\text{CH}_4$  and  $\text{H}_2$  flow rate as well as temperature and growth time (Mehdipour and Ostrikov,

2012), as shown in Figure 3.3.

Temperature of CVD graphene growth is related to the density of point defects of graphene through Arrhenius equation

$$n_{\text{defects}} \propto \exp\left(\frac{E_a}{k_B T}\right) \quad (3.1)$$

where  $n_{\text{defects}}$  is the density of defects,  $E_a$  is the activation energy,  $k_B$  is the Boltzmann constant, and  $T$  is the temperature, and it could be seen that higher temperature reduces the amount of defects. However, due to the melting point of the copper substrate (1085 °C), the synthesis temperature was limited to 1000 °C to minimize the evaporation of copper atoms to the ambient atmosphere.

### 3.1.2 CVD system

Schematic of the CVD system for synthesizing the graphene samples for this work is depicted in Figures 3.4 and 3.5. CVD consists of a quartz tube chamber (inner diameter of 100 mm) and a furnace that surrounds the quartz tube for supplying heat to the reaction zone via radiation heat transfer. Precursor gas is supplied from a gas cylinder, mediated by a pressure regulator and a mass flow rate controller (CG2000, ATOVAC). Temperature and pressure inside the chamber are monitored by a capacitance manometer (MKS Instruments) and a K-type thermocouple (Omega). A rotary pump (750 W, W2V40, Woosung Automa)

is connected to the chamber to lower the pressure, with the exhaust gas exiting through a gas scrubber to minimize the amount of combustible gas molecules. For safety purpose, a gas detector/alarm system was installed, to prevent the leakage of flammable H<sub>2</sub> or CH<sub>4</sub>.

### 3.1.3 CVD synthesis of graphene

To obtain high-quality monolayer graphene, various synthesis parameters including temperature ( $T_{\text{growth}}$ ), growth time ( $t_{\text{growth}}$ ), volumetric flow rates of H<sub>2</sub> and CH<sub>4</sub> ( $\dot{V}_{\text{methane}}$  and  $\dot{V}_{\text{hydrogen}}$ ) has been tested. It has turned out that CH<sub>4</sub> flow rate of 30 cm<sup>3</sup>/s and H<sub>2</sub> flow rate of 5 cm<sup>3</sup>/s at growth temperature of 1000 °C yields an interrupted monolayer graphene with large grain size (larger than 5 μm) and insignificant amount of defects. To obtain a completely grown graphene, a second growth step increasing the  $\dot{V}_{\text{methane}}$  from 30 to 60 cm<sup>3</sup>/s has been added to supplement the first step. To remove the copper oxide species on the surface of the copper foil catalyst substrate, as well as recrystallization of the copper surface before CVD synthesis, pre-annealing has been performed under H<sub>2</sub> environment and high temperature (1000 °C). Summarized growth procedure is shown in Figure 3.6.

It should be noted that pre-cleansing of copper foil before CVD synthesis is required to minimize the impurity that could otherwise adversely affect the growth of graphene (Kim et al., 2013). Cu foil was immersed in Ni etchant (nickel etchant TFB, Transene) for 90 seconds for removing the surface contaminants,

and washed in deionized water, acetone, and IPA, resulting in a cleaner the copper foil surface as shown in Figure 3.7.

### **3.2 Transfer of graphene**

After synthesis, monolayer graphene should be transferred to the target substrate, a TEM (transmission electron microscopy) grid of 8-nm-thick SiO<sub>2</sub> membranes in this case, procedure of which is depicted in Figure 3.8. While graphene is known to be amongst the strongest material with yield strength of up to 130 GPa (Lee et al., 2008), monolayer graphene samples are prone to tearing apart due to its extremely small cross-sectional area. Therefore, a flexible membrane is needed to strengthen the graphene sample for transfer process. Poly(methyl methacrylate)/chlorobenzene solution of 46 g/l was spin-coated on graphene/copper at 4500 rpm, followed by baking at 150 °C for 90 seconds, forming an approximately 300-nm-thick flexible polymer film on top of the graphene.

Subsequently, copper foil in contact with the layered sample of PMMA on graphene was etched away using aqueous solution of ammonium persulfate (28g/l), followed by rinsing in deionized water. The PMMA/graphene sample was manually brought to contact with the target substrate (TEM grid) in deionized water bath, and immersed in acetone in order to remove the PMMA top coat thereafter.

### 3.3 Characterization

#### 3.3.1 Scanning electron microscopy (SEM)

CVD synthesized graphene consists of patchwork quilt of randomly oriented single-crystalline domains (grains) divided by grain boundaries (Huang et al., 2011; Mattevi et al., 2011). SEM image of incompletely grown CVD graphene (i.e. supply of CH<sub>4</sub> and H<sub>2</sub> gas is cut after a short growth time) offers a simple way to estimate its average grain size for a given CVD synthesis condition. As shown in Figure 3.9, number density of nucleation sites over the investigated area is 14.5 sites per 1128  $\mu\text{m}^2$

$$\sqrt{\frac{4A}{2\pi N}} < l_{\text{graphene}} < \sqrt{\frac{4A}{\pi N}} \quad (3.2)$$

where  $N$  is the number of graphene islands,  $A$  is the investigated area, and  $l_{\text{graphene}}$  is the average grain diameter, resulting in  $l_{\text{graphene}}$  of approximately 7 - 10  $\mu\text{m}$ . As will be discussed later, grain size of our sample exceeds the average phonon mean free path of graphene (less than 1  $\mu\text{m}$ ), implying that the effect of grain boundaries on basal-plane heat conduction of graphene is negligible. Since the scope of this work is to determine the graphene-substrate interaction on heat transfer, the average grain size of our CVD graphene is considered sufficiently large.

### **3.3.2 X-ray photoelectron spectroscopy (XPS)**

XPS is a surface analysis technique probing the elemental composition and the chemical structure of a material by detecting the kinetic energy of photo-emitted electrons. XPS measurement of graphene reveals the distribution of binding energies of core electrons (s-orbital) of carbon atoms consisting the graphene, with binding energy of sp<sup>2</sup>-bonded carbon corresponding to 284.5 eV. As shown in Figure 3.10, deconvoluted C1s spectrum of the CVD synthesized graphene, obtained from XPS measurement performed in NCIRF at SNU (Sigma Probe, ThermoVG), shows that 83.6% of carbon atoms are sp<sup>2</sup>-bonded, while other 16.4% of carbons are attributed to carbon adsorbates, defects and grain boundaries. Judging from the XPS carbon spectra, our sample is comparable to the latest high-quality CVD synthesized graphene (Zhang et al., 2017).

### **3.3.3 Optical microscopy**

Optical microscopy image (100× lens, NA = 0.75) of CVD graphene transferred on SiO<sub>2</sub>/Si wafer (Figure 3.11) shows a uniform optical contrast, indicating that the coverage of graphene is complete without noticeable cracks over 180 μm × 120 μm area.

### **3.3.4 Raman spectroscopy**

Raman spectroscopy is a versatile tool for characterizing the graphene,

capable of investigating the number of layers, defects, charge carrier density, built-in strain, and thermal properties as well (Ferrari and Basko, 2013). Raman spectrum of graphene has two distinctive peaks – G peak ( $\sim 1600 \text{ cm}^{-1}$ ) and 2D peak ( $\sim 2700 \text{ cm}^{-1}$ ), respectively. G peak is known to arise from the in-plane optical bond-stretching vibrational motions of  $\text{sp}^2$  carbons (Ferrari, 2007), whereas 2D peak originates from momentum conservation relation for two phonons with opposite wave vectors (Ferrari et al., 2006). Another conditionally existent peak is the D peak ( $\sim 1350 \text{ cm}^{-1}$ ), originating from the breathing motion of the six-member carbon rings, which is Raman-active only at the presence of defects that breaks the symmetry (Tuinstra and Koenig, 1970). Raman spectra for graphene sample on 8-nm-thick  $\text{SiO}_2$  TEM grid has been obtained using 514 nm laser (inVia, Renishaw), with positions, intensity, and width of G and 2D peaks of graphene determined from WiRE 3.4 spectral analysis software. Typical Raman spectrum of our sample is shown in Figure 3.12.

Raman spectrum of a monolayer graphene is known to have an intensity ratio between 2D and G peaks over two

$$\frac{I_{2D}}{I_G} > 2 \quad (3.1)$$

where  $I_{2D}$  and  $I_G$  are the heights of the G and 2D peaks, respectively. On the other hand, multilayered graphene has an  $I_{2D}$  to  $I_G$  ratio of less than two, due to

broadening and decomposition of the 2D peak into multiple peaks. Another criterion for assessing the number of graphene layers is the FWHM (full-width at half maximum), where  $\text{FWHM}_{2\text{D}}$  of a monolayer graphene is approximately  $30\text{ cm}^{-1}$  while that of a multilayer graphene is larger than  $40\text{ cm}^{-1}$  (Li et al., 2009b). It is clearly seen in Fig. 3.12 that our sample is monolayer dominant with  $I_{2\text{D}}$  to  $I_{\text{G}}$  ratio of more than three and  $\text{FWHM}_{2\text{D}}$  of less than  $30\text{ cm}^{-1}$ . It is also evident in Fig. 3.12 that Raman D peak is of negligible intensity, alluding to the point-defect-free quality of our graphene sample.

### 3.4 Conclusion

Large-area high-quality monolayer graphene has been synthesized by CVD method using copper foil as the catalyst substrate with  $\text{CH}_4$  and  $\text{H}_2$  as reactant gas, and PMMA technique has been deployed to transfer the graphene from the copper foil to the target substrate (TEM grid). SEM measurement for an intermediately grown sample shows the large single-crystalline domain size of our graphene, and Raman measurement as well as optical image reveals that the graphene is uniformly covered and monolayer dominant. XPS measurement for binding energy of carbon core electrons ( $\text{C1s}$ ) and the absence of Raman D peak at  $1350\text{ cm}^{-1}$  demonstrates that the graphene contains negligible amount of defects. As a result, our graphene sample is of adequate quality for the subsequent thermal conductivity measurements.



	Pros	Cons
<b>Mechanical Exfoliation</b>	<ul style="list-style-type: none"> <li>✓ Easy to produce</li> <li>✓ High quality</li> </ul>	<ul style="list-style-type: none"> <li>✓ Small sample size</li> <li>✓ Tape residuals</li> </ul>
<b>Chemical Exfoliation</b>	<ul style="list-style-type: none"> <li>✓ Mass production</li> </ul>	<ul style="list-style-type: none"> <li>✓ Low quality</li> </ul>
<b>CVD</b>	<ul style="list-style-type: none"> <li>✓ Large sample size</li> <li>✓ Easy to produce</li> <li>✓ Easy to transfer</li> <li>✓ Capable of doping</li> </ul>	<ul style="list-style-type: none"> <li>✓ Reaction residuals</li> <li>✓ Polycrystalline</li> </ul>
<b>Epitaxial</b>	<ul style="list-style-type: none"> <li>✓ Very clean synthesis</li> </ul>	<ul style="list-style-type: none"> <li>✓ High temperature</li> <li>✓ Ultrahigh vacuum</li> </ul>

Table 3.1 Comparison of graphene synthesis techniques.

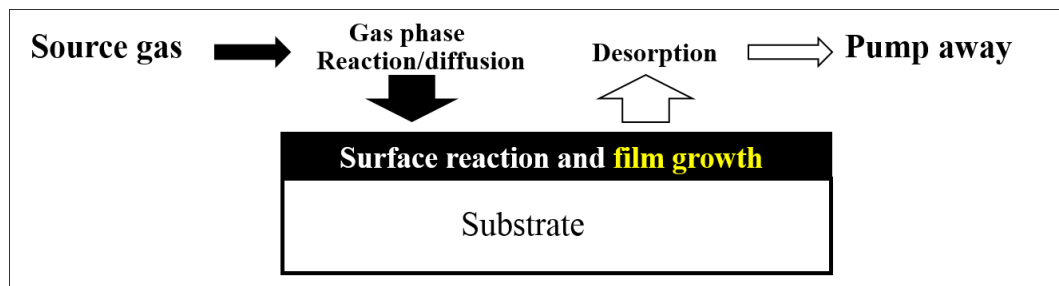


Figure 3.1 Schematic of chemical vapor deposition technique.

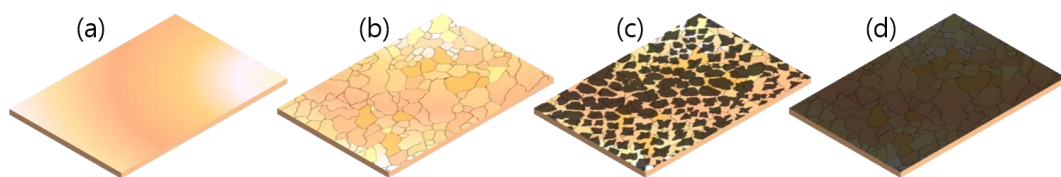


Figure 3.2 Growth of graphene on a copper foil. (a) Copper foil as received. (b) Recrystallization of copper after annealing at 1000 °C. (c) Initial stage of graphene growth – formation of graphene islands. (d) Complete growth of graphene on copper foil.

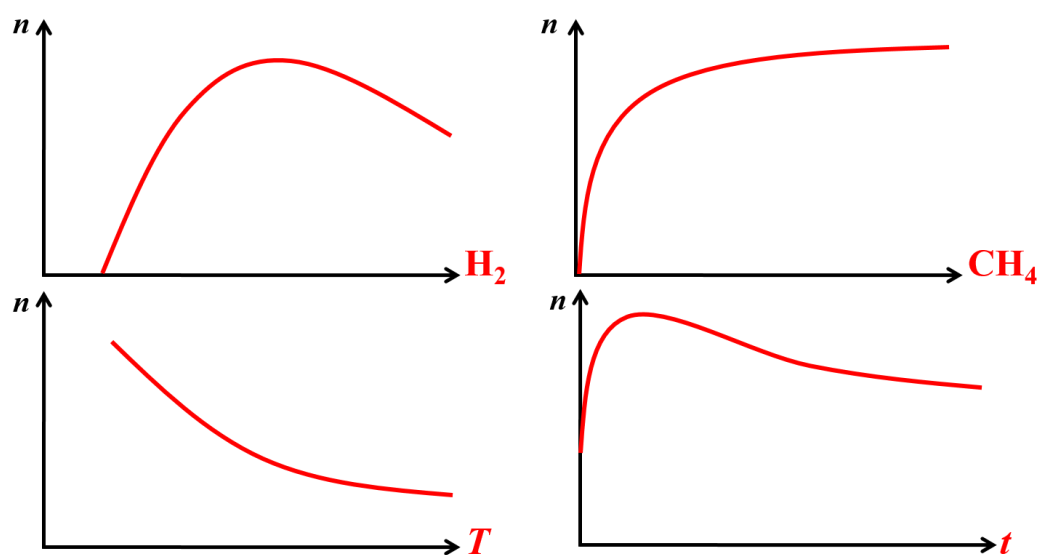


Figure 3.3 Relation between nucleation density ( $n$ ) of graphene growth and CVD synthesis parameters.

## CVD system

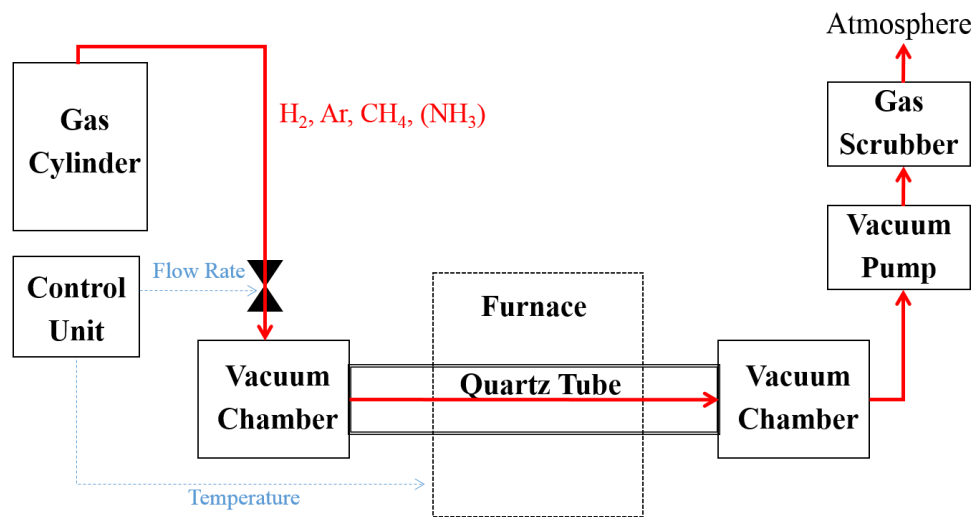
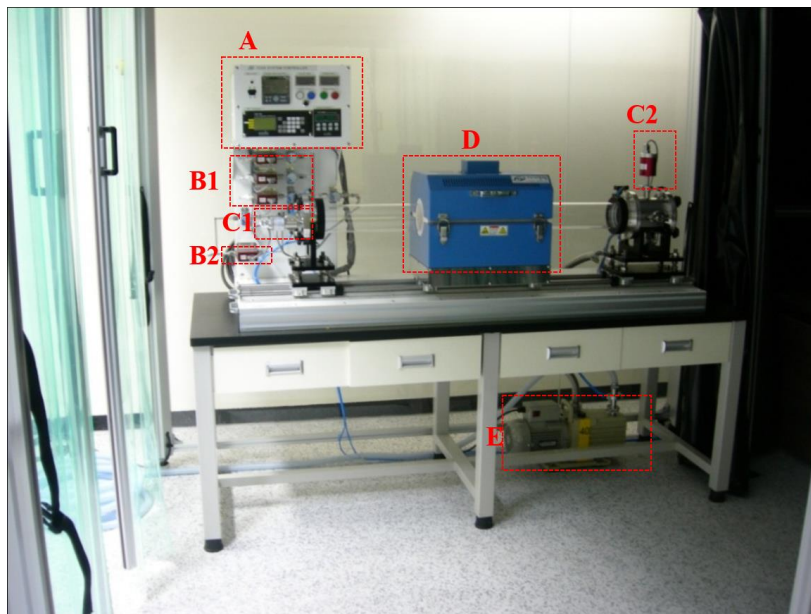


Figure 3.4 Schematic of the CVD equipment.



- A. Controller box
- B1. Mass flow rate controller (Ar, CH<sub>4</sub>, H<sub>2</sub>)
- B2. Mass flow rate controller (NH<sub>3</sub>)
- C1. Manometer
- C2. Capacitance manometer
- D. Furnace
- E. Rotary pump

### Fume Hood

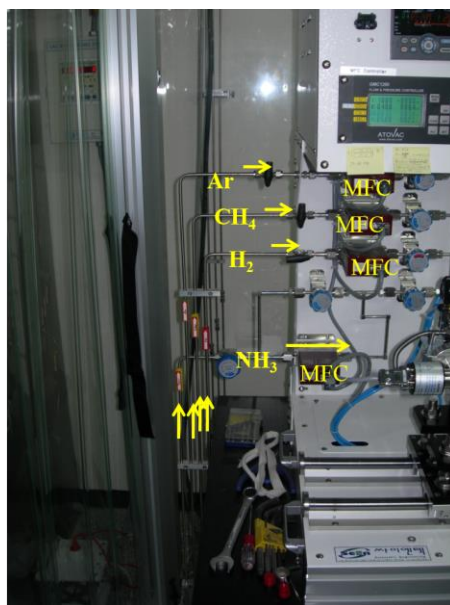


Figure 3.5 Photographic image of the CVD equipment and its components.

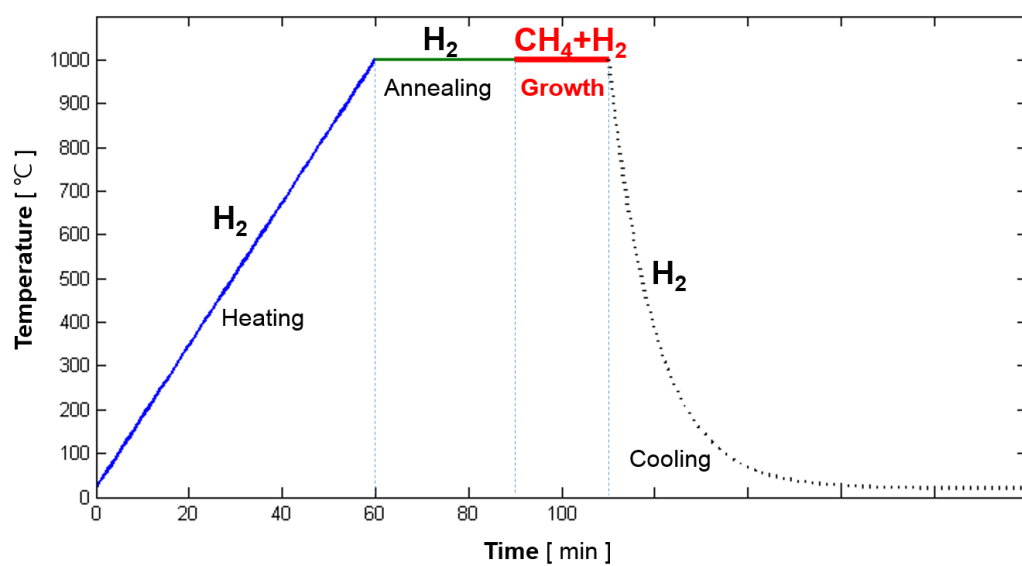


Figure 3.6 Graphene CVD synthesis procedure using CH<sub>4</sub> and H<sub>2</sub> as precursor gas.

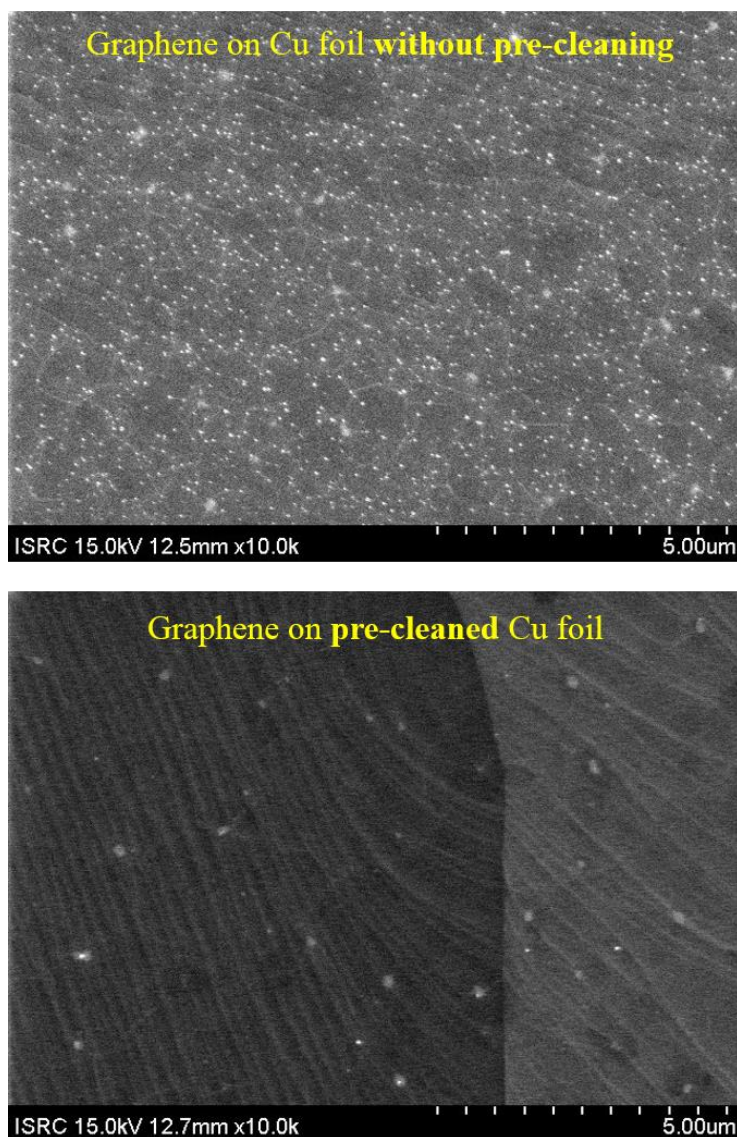


Figure 3.7 Comparison of SEM image of graphene/copper foil sample with (below) and without (above) pre-cleansing of the copper foil. Note the difference in contaminant (white particles) densities.



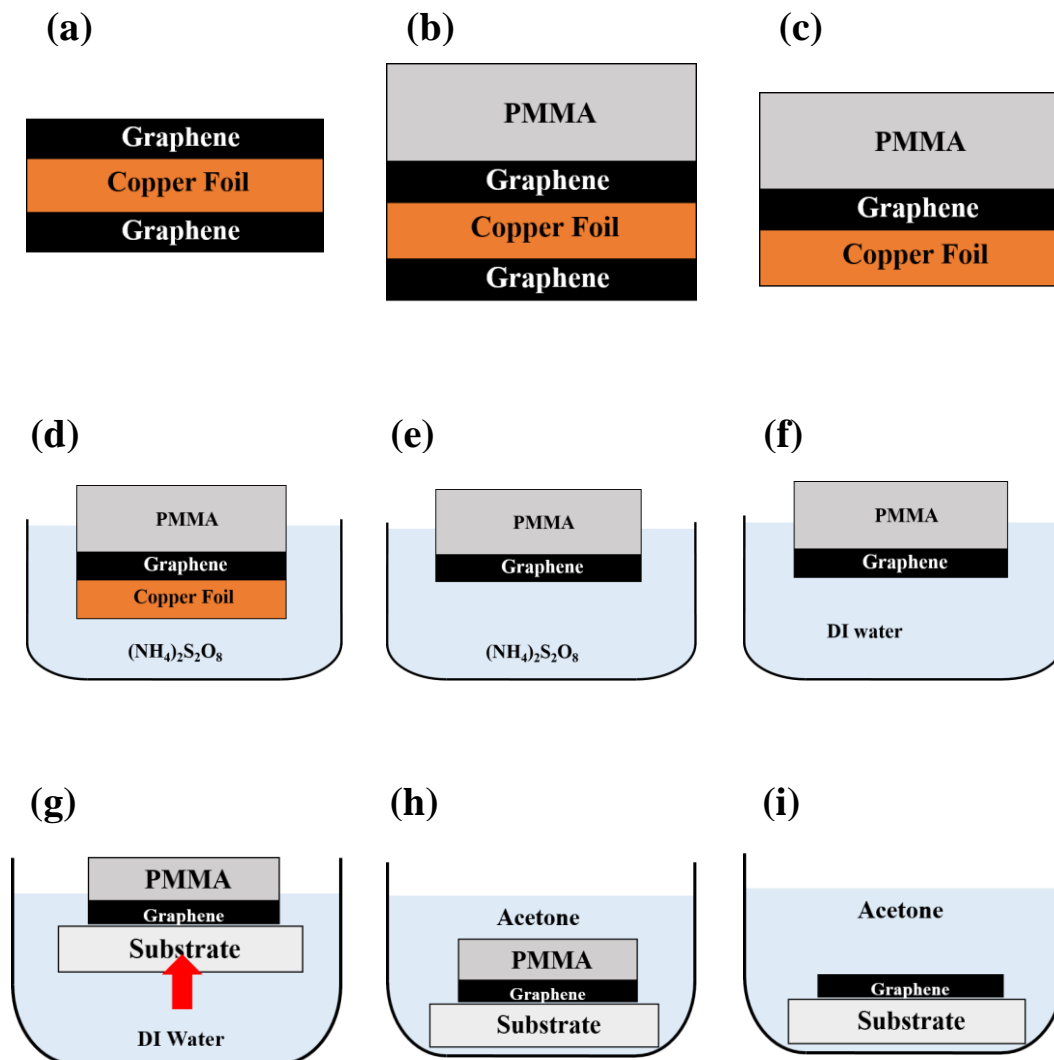


Figure 3.8 Transfer of graphene from copper foil catalyst to target substrate using PMMA method. (a) Graphene as synthesized by CVD technique. (b) PMMA flexible membrane spin-coated on graphene. (c) Removal of the graphene at the other side (backside) of the copper foil. (d), (e) Etching of copper in ammonium persulfate. (f) Cleansing in deionized water. (g) Graphene/PMMA sample brought to contact with the target substrate. (h), (i) Dissolution of the PMMA top layer in acetone.

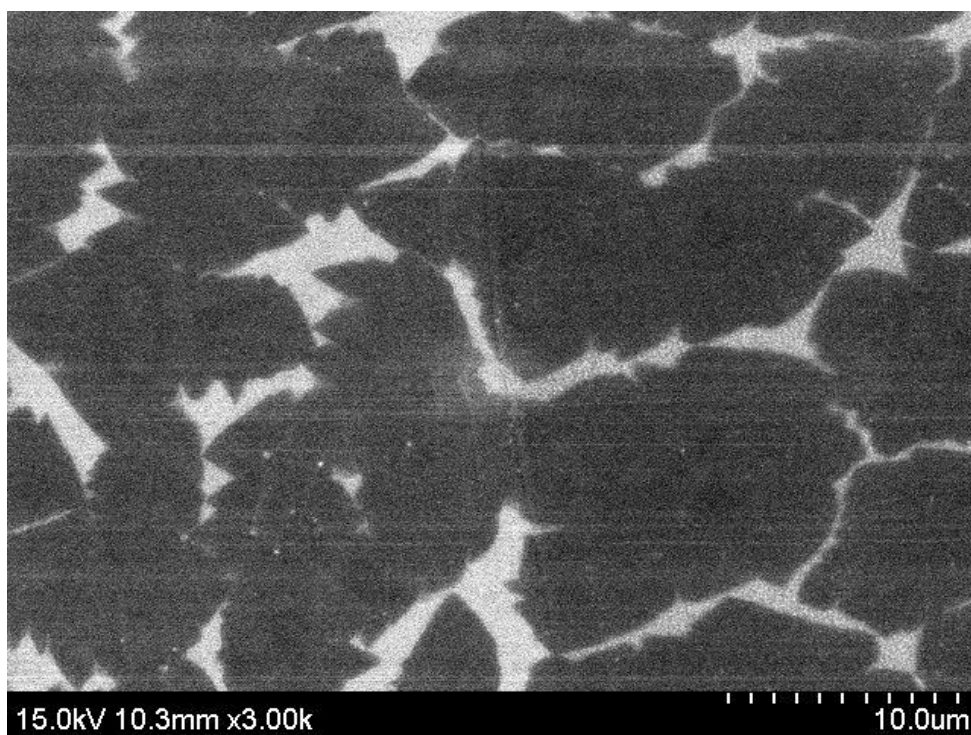


Figure 3.9 SEM image of initial stage of the graphene growth. Flow rates for  $\text{CH}_4$  and  $\text{H}_2$  were 30 sccm and 5 sccm, respectively, at 1000  $^{\circ}\text{C}$ .

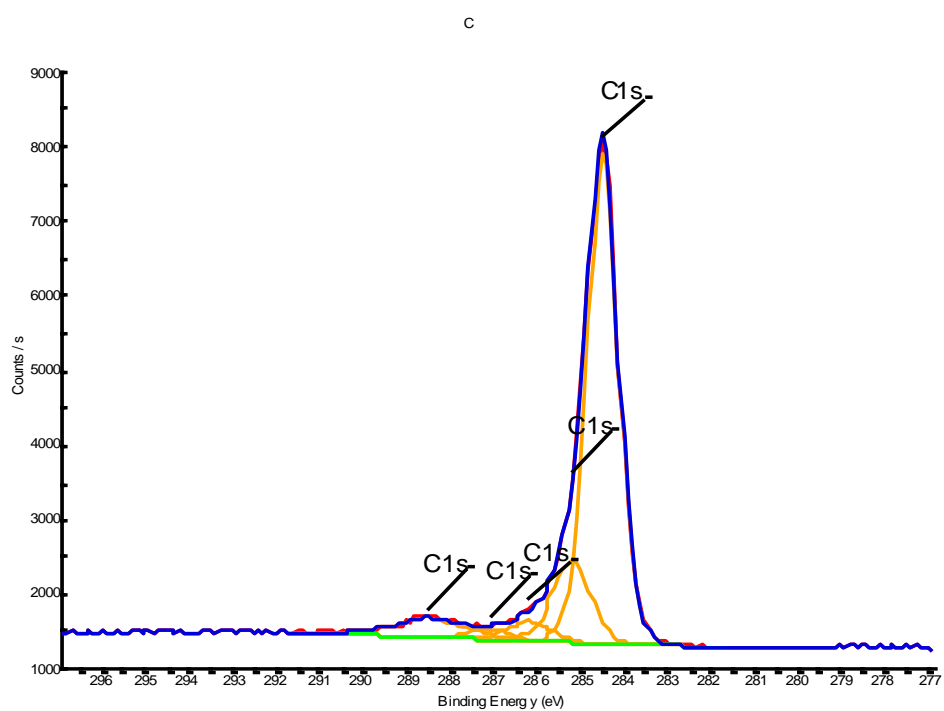


Figure 3.10 Core electron binding energy of carbon (C1s spectrum) for CVD synthesized graphene. XPS measurement was taken at NCIRF, SNU.



Figure 3.11 Optical microscopy (100x lens) image of CVD graphene on SiO<sub>2</sub>/Si wafer with SiO<sub>2</sub> thickness of 280 nm. Mostly uniform shade of the image indicates monolayer dominant characteristic of our sample, without major cracks.

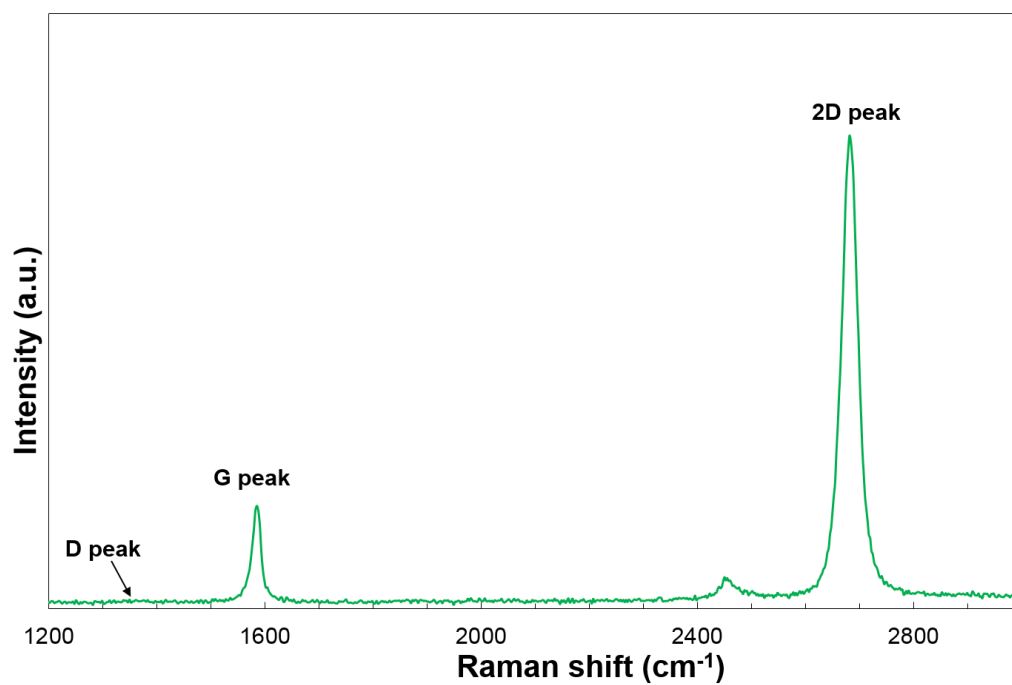


Figure 3.12 Raman spectrum of the CVD graphene sample transferred on 8-nm-thick SiO<sub>2</sub> TEM grid.

# **Chapter 4**

## **Optothermal Raman Measurement of Supported Graphene Thermal Conductivity**

### **4.1 Introduction**

In this chapter, we implement the optothermal Raman method that has been devised (Chapter 2), using the high-quality monolayer graphene synthesized by CVD method which has been transferred on an 8-nm-thick SiO<sub>2</sub> substrate (Chapter 3). Procedure of optothermal Raman measurement is described in Section 2.3 and schematically represented in Fig. 2.3 (b). Thermal conductivity of supported monolayer graphene has been measured over a temperature range from 350 K to 600 K for a varying numbers of thermal annealing pre-treatment before the measurement is conducted. The purpose of repeated thermal annealing is to enhance the graphene-substrate conformity, the effect of which will be discussed in Chapter 4.

### **4.2 Effective optical absorbance of supported graphene**

While optical absorbance of a suspended graphene has been studied previously (Nair et al., 2008; Cai et al., 2010), assessing the effective absorbance

of laser power by the supported graphene sample should take into consideration the effect of the substrate. The procedure of evaluating the effective absorbance,  $\alpha_{\text{eff}}$ , is shown in Figure 4.1, where power of the laser (514 nm wavelength collimated by 100x objective lens with  $NA = 0.75$ ) was measured using a powermeter (Fig. 4.2 (a)). By comparing the power of the incident laser ( $P_0$ , Case 0) and the transmitted laser through the 8-nm substrate without the graphene ( $P_1$ , Case 1), reflectance of the substrate ( $\rho_{\text{SiO}_2}$ ) is determined as

$$\rho_{\text{SiO}_2} = 1 - \frac{P_1}{P_0} \quad (4.1)$$

By measuring the transmitted laser power of the 8-nm substrate with the graphene ( $P_2$ , Case 2), optical absorbance of the monolayer graphene ( $\alpha_g$ ) is deduced as

$$\alpha_g = 1 - \frac{P_2}{P_0} \frac{1}{1 - \rho_{\text{SiO}_2}} \quad (4.2)$$

The power absorbed by the supported graphene sample ( $P_{\text{eff}}$ ) is summation of the incident and reflected (by the  $\text{SiO}_2$  substrate) laser beam absorbed by the graphene, expressed as

$$P_{\text{eff}} = \alpha_g \{1 + \rho_{\text{SiO}_2} (1 - \alpha_g)\} P_0 = \alpha_{\text{eff}} P_0 \quad (4.3)$$

The measured value of  $\rho_{\text{SiO}_2}$  was  $3.687 \pm 0.408$  %, which is in good agreement with the calculated  $\rho_{\text{SiO}_2}$  value of 3.7 % using the Fresnel equation and the refractive index of  $1.476 + 0i$  for an 8-nm  $\text{SiO}_2$  respectively. The measured value of  $\alpha_g$  was  $3.011 \pm 0.142$  %, along with  $\rho_{\text{SiO}_2}$ , resulting in  $\alpha_{\text{eff}}$  value of  $3.119 \pm 0.158$  %, obtained from Eq. (4.3).

### 4.3 Sample description in terms of thermal annealing

Experimental results denoted as ‘1<sup>st</sup>’, ‘2<sup>nd</sup>’, ‘3<sup>rd</sup>’, and ‘4<sup>th</sup>’ are named after the number thermal annealing cycles in atmospheric condition (1 atm) from 300 K to 550 K. Sample ‘N<sup>th</sup>’ has been thermally annealed repeatedly for more than 10 cycles from 300 K to 600 K in atmospheric condition. Sample ‘VAC’ has been thermally annealed in high vacuum condition ( $\sim 10^{-7}$  torr) from 300 K to 520 K. ‘1<sup>st</sup>’ to ‘N<sup>th</sup>’ are for an identical sample with different number of annealing cycles, whereas ‘VAC’ is a separately prepared sample. Thermal annealing conditions for the corresponding samples are shown in Figure 4.3.

### 4.4 Raman peak position vs. temperature

In optothermal Raman technique, temperature change ( $\Delta T$ ) is determined from the measured position shift ( $\Delta\omega$ ) of either Raman G or 2D peak of the graphene.



To assess the quantitative relation between  $\Delta T$  and  $\Delta\omega$ , position change of the supported graphene sample was measured as the temperature was controlled by a heated stage, as shown in Fig. 4.2 (b).

#### **4.4.1 Linear temperature dependence of Raman peaks for samples 1<sup>st</sup>, 2<sup>nd</sup>, and 3<sup>rd</sup>**

Raman peak position as a function of temperature is fitted to a 1<sup>st</sup> order polynomial function ('straight line'), which is valid for a suspended graphene. Measurement data for Raman G and 2D peak position of 1<sup>st</sup>, 2<sup>nd</sup>, and 3<sup>rd</sup> are shown in Figures 4.4 and 4.5. The resulting temperature coefficients of Raman G and 2D peaks ( $\partial\omega/\partial T$ ) are listed in Table 4.1. It is seen that  $\partial\omega/\partial T$  values of G peak position for 1<sup>st</sup>, 2<sup>nd</sup>, and 3<sup>rd</sup> are not only similar to each other, but also in good agreement with the values reported for a suspended graphene experimentally (Calizo et al., 2007), and with the theoretical prediction (Bonini et al., 2007).

#### **4.4.2 Curve-fitting of temperature dependence of Raman peaks for samples 4<sup>th</sup>, N<sup>th</sup>, and VAC**

On the other hand, the samples where the graphene is believed to be strongly adhered to the substrate due to repeated thermal annealing (4<sup>th</sup>, N<sup>th</sup>, and VAC) showed larger  $\partial\omega/\partial T$  values with distinctively convex-downwards behavior of  $\Delta\omega$  as a function of  $\Delta T$ , suggesting the inadequacy of a straight-line approximation, as shown in Figure 4.6.

In this regard, we deployed a more sophisticated curve-fitting model to the relevant samples, proposed by Yoon et al. (2011), accounting for the measured shift of Raman G peak position with respect to the temperature difference ( $\Delta\omega^{\text{total}}$ ) as a superposition of the intrinsic contribution ( $\Delta\omega^{\text{intrinsic}}$ ) and the thermal expansion mismatch strain contribution ( $\Delta\omega^{\text{strain}}$ ). While the  $\Delta\omega^{\text{intrinsic}}$  is directly adopted from a theoretical model based on first principles calculation (Bonini et al., 2007),  $\Delta\omega^{\text{strain}}$ , arising from the difference in thermal expansion coefficient (TEC) between the graphene and the underlying substrate, is given as

$$\Delta\omega^{\text{strain}}(T) = \int_{300K}^T \left[ -2\omega_0\gamma \left\{ \beta_{\text{SiO}_2}(T) - \beta_g(T) \right\} \right] dT \quad (4.4)$$

where  $\omega_0$  is the Raman peak position at 300 K, where  $\omega_0$  ( = 1580 cm<sup>-1</sup>) is the Raman G peak position at room temperature,  $\gamma$  ( = 1.8) is the Grüneisen parameter of graphene (Zabel et al., 2012; Metten et al., 2014),  $\beta_g$  and  $\beta_{\text{SiO}_2}$  are the thermal expansion coefficients of graphene and SiO<sub>2</sub>, respectively, and  $\beta_{\text{SiO}_2}(T)$  is adopted from the existing database (Standard Reference Material 739 Certificate, NIST). To restrict the number of fitting parameters, a first-order temperature dependence of  $\beta_g(T) = \beta_0 + \beta_1(T - T_\infty)$  has been assumed.  $\beta_g(T)$  has been obtained by minimizing the mean squared error (MSE) of temperature calibration of N<sup>th</sup> sample, given as

$$MSE = \frac{1}{n} \sum_{i=1}^n (\omega_i - \Omega_i)^2 \quad (4.5)$$

where  $\omega_i$  and  $\Omega_i$  are the G peak positions of the  $i$ -th measurement and fitting model values corresponding to the controlled temperature  $T_i$ , respectively, and  $n$  ( $= 405$ ) is total number of measured data points. As a result, curve fitting of N<sup>th</sup> sample is shown in Figure 4.7 (red solid line), corresponding to the optimized set of parameters,  $\beta_0$  and  $\beta_1$ , of  $-7.86 \times 10^{-6} \text{ K}^{-1}$  and  $3.72 \times 10^{-8} \text{ K}^{-2}$ , respectively. It is noteworthy that TEC of graphene ( $\beta_g$ ) obtained from the curve fitting of N<sup>th</sup> sample is in reasonable agreement with previous experiments, as shown in Figure 4.8.

In assessing the temperature rise from the measured Raman shift over varying incident laser power, details of which will be explained in the following section (Section 4.5), we relied upon the curve fitting result of N<sup>th</sup>, instead of those of the corresponding samples. Although temperature calibration also had been conducted over 4<sup>th</sup> and VAC samples as well as N<sup>th</sup>, the total number of temperature calibration data points of 4<sup>th</sup> ( $n = 50$ ) and VAC ( $n = 26$ ) were significantly smaller than that of N<sup>th</sup> ( $n = 405$ ), to the point of being inadequate to represent the subtle convex-downwards curvature associated with the non-linear fitting model (as discussed above) resulting from the corresponding samples. The restrictions in the total number of acquired data points were imposed inevitably to minimize the undesirable thermal annealing effect involved in the temperature

calibration process, while  $N^{\text{th}}$  is inherently free of such restraints, enabling multiple sets of temperature calibration measurement and large number of data points. The validness of substituting the temperature calibration fitting curve of  $4^{\text{th}}$  and VAC samples with that of  $N^{\text{th}}$  is illustrated in Figure 4.6, where it is clearly shown that temperature calibration data points of  $4^{\text{th}}$  (red filled square markers) and VAC (blue open diamond markers) are distributed along the fitted model of  $N^{\text{th}}$  (solid black line), and all of the data points of  $4^{\text{th}}$  and VAC are within the 95% prediction band (Bonferroni method) of the  $N^{\text{th}}$  without exception.

As for samples  $4^{\text{th}}$ ,  $N^{\text{th}}$ , and VAC, where the nonlinear temperature calibration model discussed above was deployed, only the Raman G peak position was used in assessing the temperature, since a theoretical model accounting for the  $\Delta\omega^{\text{intrinsic}}(T)$  contribution to the  $\Delta\omega^{\text{total}}(T)$  for the Raman 2D peak was not available. On the contrary, as for the samples Ambient-1st to -3rd, where straight-lined 1<sup>st</sup> order approximation was applied, both the Raman G and 2D peaks were utilized.

## 4.5 Temperature vs. laser power

To determine the thermal conductivity of supported graphene as a function of temperature, Raman peak shift ( $\Delta\omega$ ) has been measured as a function of laser power ( $P_L$ ), where  $\Delta\omega$  is transduced into  $\Delta T$  using the results of Section 4.4. The result are shown in Figure 4.8, where  $\Delta\omega$  for G and 2D peaks are plotted versus

the absorbed laser power ( $P_{\text{eff}}$ ), respectively.

## 4.6 Thermal conductivity dependence on pre-annealing

From the results of Section 4.2 ~ 4.5, combined with the 3D heat transfer model, thermal conductivity  $k_g$  of the supported graphene could be determined. In principle,  $k_g$  is determined as the parameter that best fits the measured temperature  $T_m$  for the given amount of laser power  $P_L$ . To minimize the time consuming trial-and-error iteration, a quantitative one-to-one relation between  $k_g$  and  $\Delta T_m/P_L$  has been tabulated as a polynomial function using a spline-interpolation method, which is possible since the governing equations Eqs. (2.3) and (2.4) are linear with respect to the variable  $\Delta T_m$ . Coefficients of a 50<sup>th</sup> order polynomial function have been derived from spline interpolation over 80 pairs of  $k_g$  and  $\Delta T_m/P_L$  obtained by 3D heat transfer model, using the 1-D interpolation function of MATLAB software (`interp1(x, y, xx, 'spline')`), as shown in Figure 4.10. Based on this result any  $\Delta T_m/P_L$  data could be converted to thermal conductivity.

The thermal conductivity of supported graphene as a function of temperature for 1<sup>st</sup>, 2<sup>nd</sup>, 3<sup>rd</sup>, 4<sup>th</sup>, N<sup>th</sup>, and VAC are shown in Figure 4.11 with their respective measurement errors. Previous experimental studies on supported graphene (Cai et al., 2010; Seol et al., 2010; Wang et al., 2011; Bae et al., 2013; Sadeghi et al., 2013) and suspended graphene (Cai et al., 2010; Chen et al., 2011, Chen et al., 2012a, Chen et al., 2012b), as well as that of a pyrolytic graphite (Touloukian,

1970) are shown in Figure 4.12, for comparison. For the first time, the thermal conductivity of monolayer graphene has been measured at temperatures higher than 400 K.

From Figure 4.11, it is seen that  $k_g$  of supported graphene varies not only with temperature, but also with number of thermal annealing cycles. Especially, for the supported graphene sample that has been annealed only once (1<sup>st</sup>), the  $k_g$  values are comparable with those of suspended graphene, exceeding 3000 W/m K at 344 K, as clearly seen in Figure 4.12. This unusually high thermal conductivity of supported graphene is contrary to the perception that  $k_g$  of supported graphene is several factors lower than that of suspended graphene, due to strong substrate-induced phonon scattering with respect to the out-of-plane acoustic (ZA) phonon modes, which is the dominant contributor to the thermal conduction of graphene (Seol et al., 2010; Lindsay et al., 2010). The highest thermal conductivity reported for a monolayer supported graphene on SiO<sub>2</sub> was 617 W/m K at ~300 K for the experimental measurement (Seol et al., 2010; Seol et al., 2011) and 923 W/m K for the theoretical prediction (Lee et al., 2015), while 1<sup>st</sup>-sample has the maximum  $k_g$  value of 3396 W/m K, which is even higher than most of the experimental reports for the suspended graphene, as Figure 4.12 shows.

As thermal annealing is repeated at atmospheric conditions from 2<sup>nd</sup> to N<sup>th</sup>, thermal conductivity is gradually decreased until becoming saturated, where peak  $k_g$  value of N<sup>th</sup> was 948 W/m K, which is drastically lower than that of the 1<sup>st</sup>, but significantly higher than 617 W/m K that has been measured by a micro-

resistance method (Seol et al., 2010; Seol et al., 2011). We temporarily attributed this difference to the measurement condition, where micro-resistance method was implemented in a vacuumized chamber while our optothermal Raman measurement was conducted in atmospheric conditions. It has been reported previously that average separation distance between graphene and SiO<sub>2</sub> decreases from 9 Å in atmospheric condition to 4.2 Å in vacuum condition which is attributed to reduced amount of ambient molecular species (Ishigami et al., 2007), alluding to a different degree of substrate-induced phonon scattering for supported graphene in vacuum and atmospheric condition. While optothermal Raman measurement under vacuum condition was not possible with the existing equipment, pre-annealing was conducted in an attempt to further reduce the graphene-substrate separation distance of the supported graphene, resulting in VAC-sample. Interestingly, the peak thermal conductivity of VAC was 646 W/m K at 352 K, which is very close to the value reported by Seol et al. (2010).

## **4.7 Conclusion**

Optothermal Raman measurement has been performed for supported monolayer CVD graphene samples on 8-nm-thick SiO<sub>2</sub> substrate, where thermal conductivity has been evaluated from the measured temperature and the 3D heat transfer model. To the best of our knowledge, we were the first to report the thermal conductivity of supported graphene at temperatures higher than 400 K,

which is critical for thermal management of high-current high-performance device application of graphene. As predicted by the numerical analysis, the uncertainties of our measured thermal conductivity values improved dramatically over the previous work (Cai et al., 2010) and were comparable to those reported for suspended graphene, demonstrating the viability of optothermal Raman technique for supported graphene as well as suspended graphene thermal conductivity measurements.

Furthermore, our result shows that the thermal conductivity of supported graphene is strongly dependent upon sample preparation conditions (i.e. number of pre-annealing), where thermal conductivity values ranged from 646 W/m K (vacuum-annealed sample) and 900 W/m K (more than 10 annealing cycles) to 3396 W/m K (single annealing cycle) at temperatures around 350 K. The effect of annealing on thermal conductivity of supported graphene will be discussed in the following chapter.



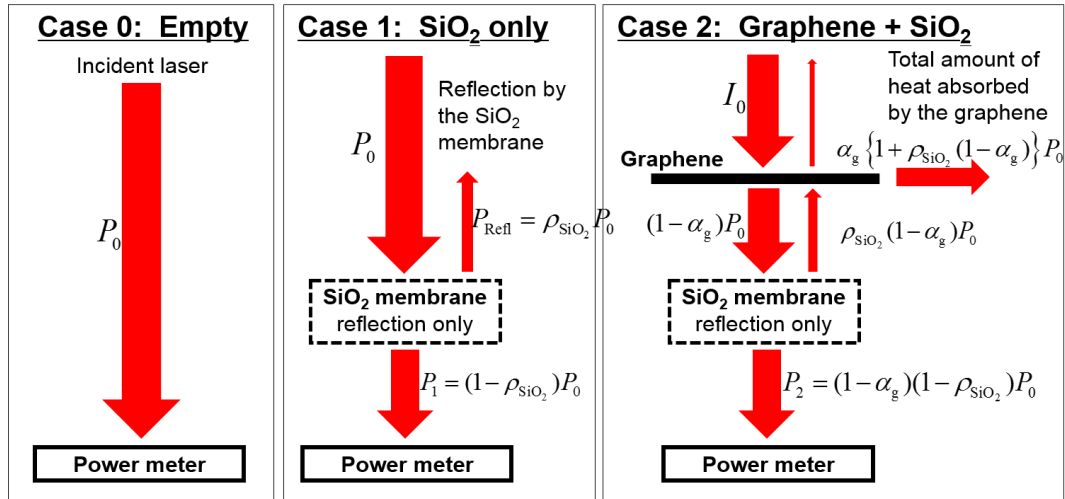


Figure 4.1 Procedure of determining the effective absorbance of supported graphene on 8-nm-thick SiO<sub>2</sub> substrate using a powermeter.

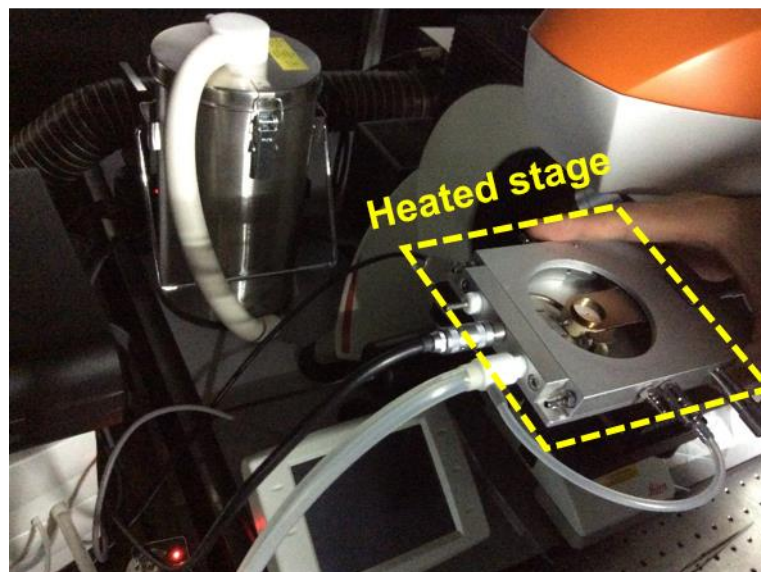
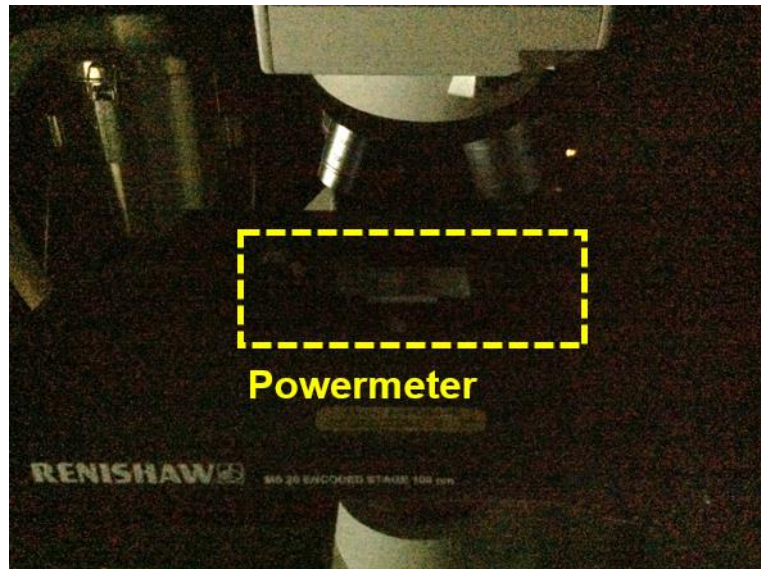


Figure 4.2 Photographic image of the powermeter (above) and the temperature-controlled heated stage (below).

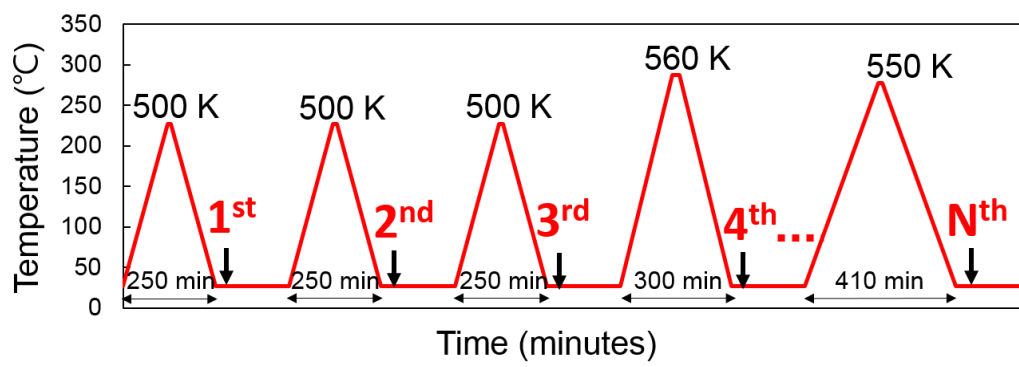


Figure 4.3 Thermal annealing conditions for 1<sup>st</sup>, 2<sup>nd</sup>, 3<sup>rd</sup>, 4<sup>th</sup> and N<sup>th</sup> samples.

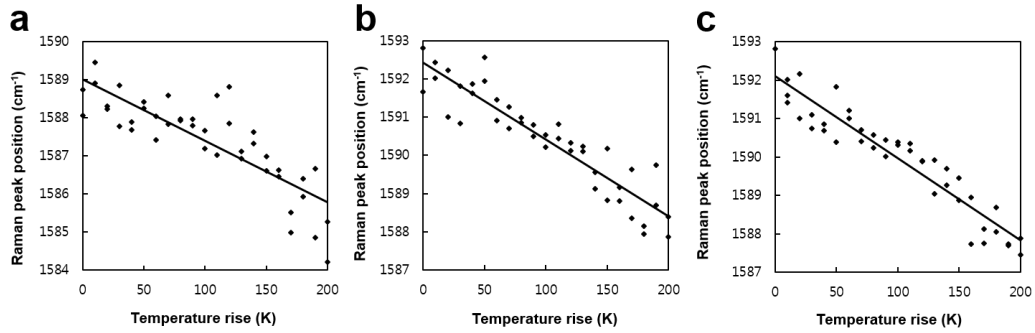


Figure 4.4 Temperature dependence of Raman G peak positions for 1<sup>st</sup> (a), 2<sup>nd</sup> (b), and 3<sup>rd</sup> (c) samples.

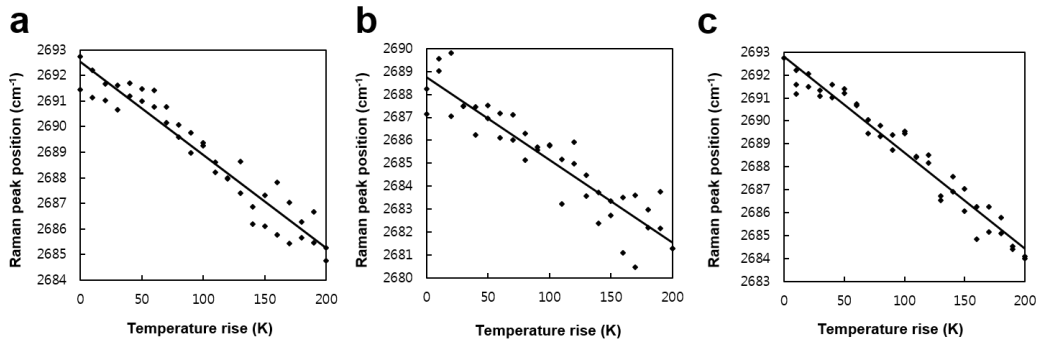


Figure 4.5 Temperature dependence of Raman 2D peak positions for 1<sup>st</sup> (a), 2<sup>nd</sup> (b), and 3<sup>rd</sup> (c) samples.

	$\partial\omega_G/\partial T$	$\partial\omega_{2D}/\partial T$
1 <sup>st</sup>	$-0.01617 \pm 0.003457 \text{ cm}^{-1}/\text{K}$	$-0.03615 \pm 0.004781 \text{ cm}^{-1}/\text{K}$
2 <sup>nd</sup>	$-0.02006 \pm 0.002660 \text{ cm}^{-1}/\text{K}$	$-0.03636 \pm 0.003305 \text{ cm}^{-1}/\text{K}$
3 <sup>rd</sup>	$-0.02134 \pm 0.002376 \text{ cm}^{-1}/\text{K}$	$-0.04190 \pm 0.002836 \text{ cm}^{-1}/\text{K}$

Table 4.1 Temperature coefficients of Raman G and 2D peak positions for 1<sup>st</sup>, 2<sup>nd</sup>, and 3<sup>rd</sup> samples.

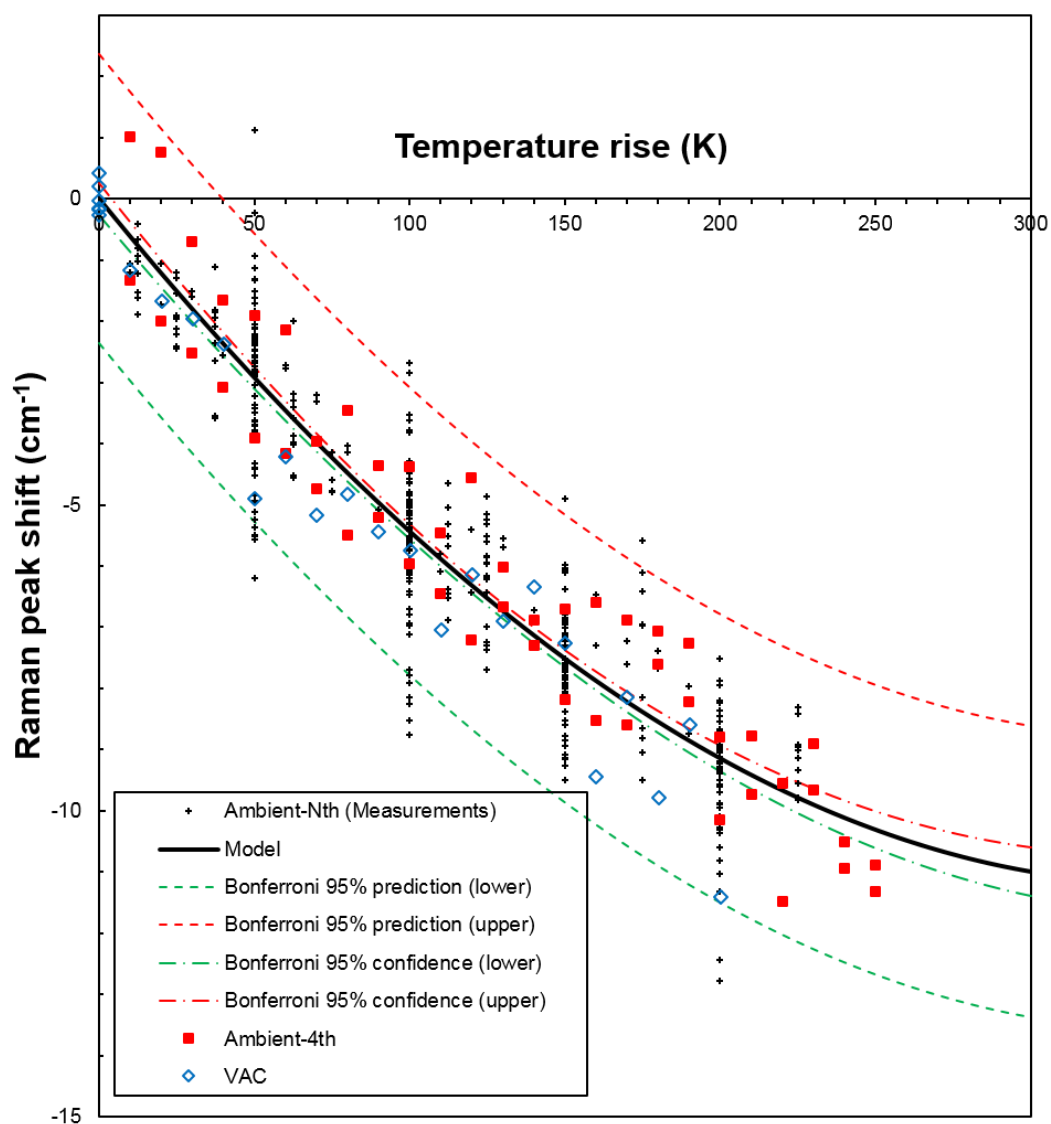


Figure 4.6 Temperature dependence of Raman G peak positions for 4<sup>th</sup>, Nth, and VAC samples, along with the prediction and confidence bands determined from Bonferroni criteria.

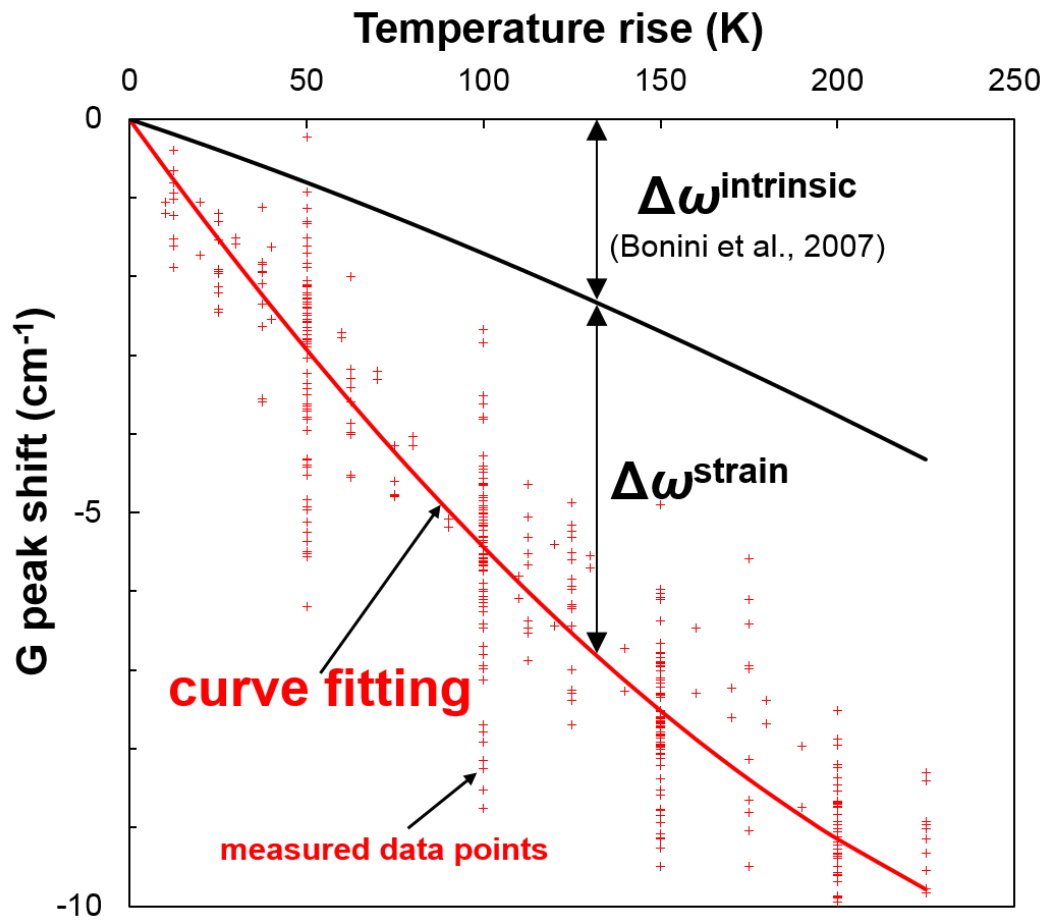


Figure 4.7 Curve fitting of Raman G peak position as a function of temperature change for the N<sup>th</sup> sample, where temperature change is the summation of intrinsic component and thermal expansion mismatch induced strain component.

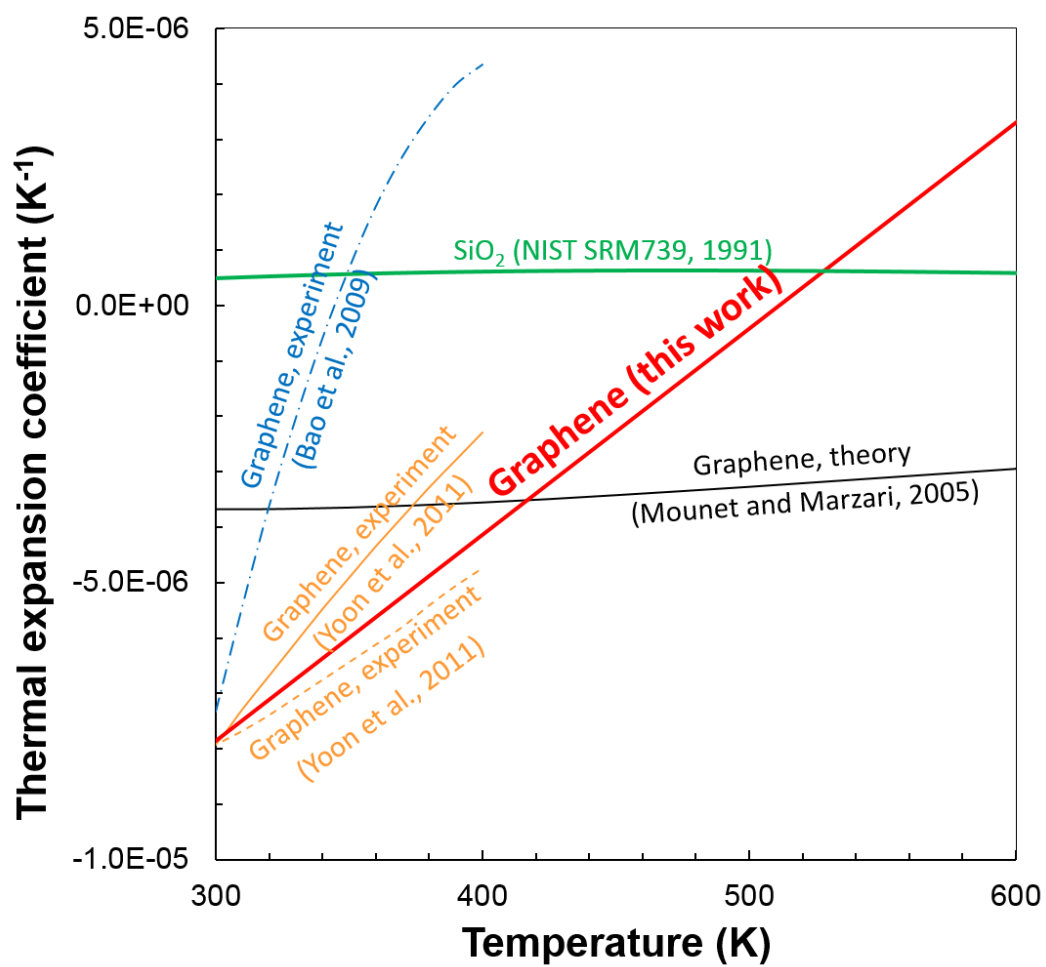


Figure 4.8 Thermal expansion mismatch coefficient of monolayer graphene deduced from the curve-fitting of Raman G peak position as a function of temperature.

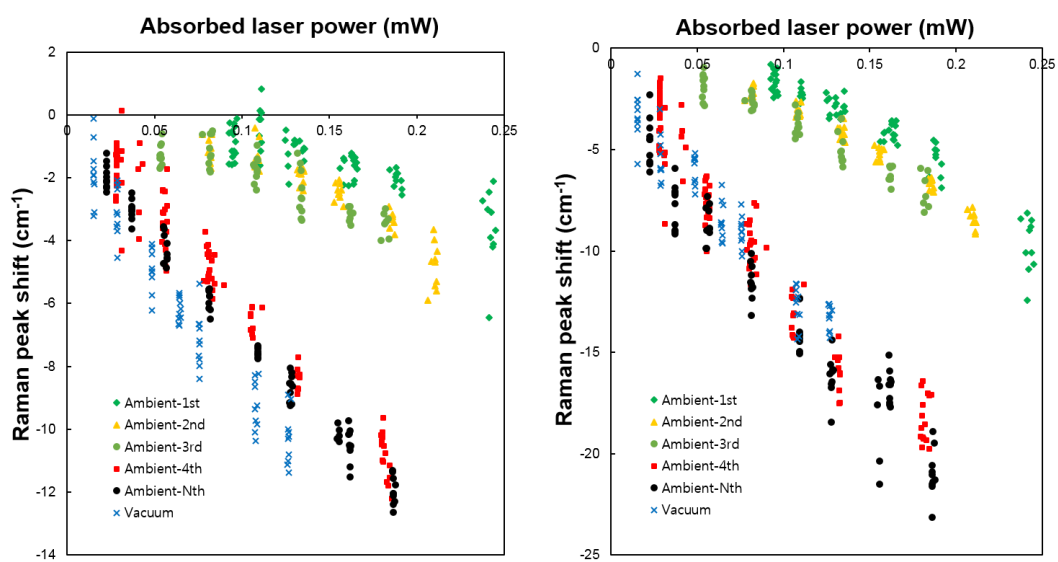


Figure 4.9 Shifts of Raman G (left) and 2D (right) peak positions upon varying laser power for 1<sup>st</sup>, 2<sup>nd</sup>, 3<sup>rd</sup>, 4<sup>th</sup>, N<sup>th</sup>, and VAC samples.



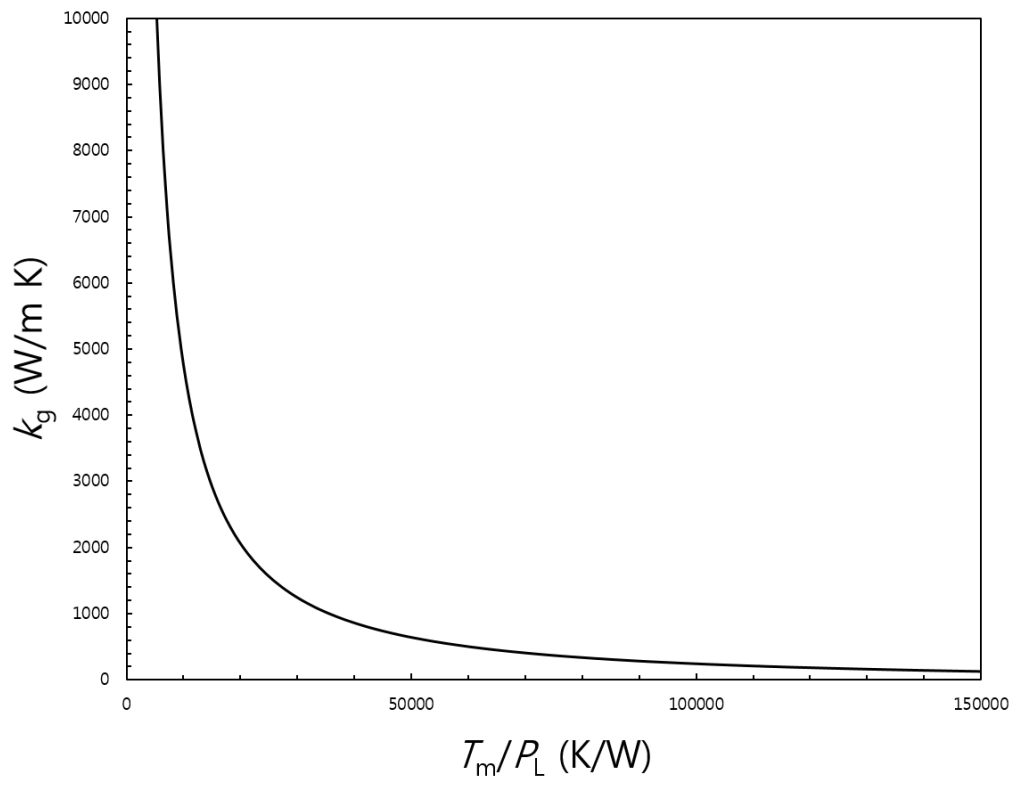


Figure 4.10 Thermal conductivity of graphene ( $k_g$ ) as a function of measured temperature ( $T_m$ ) divided by laser power ( $P_L$ ), obtained from the 3D heat transfer model and spline interpolation.

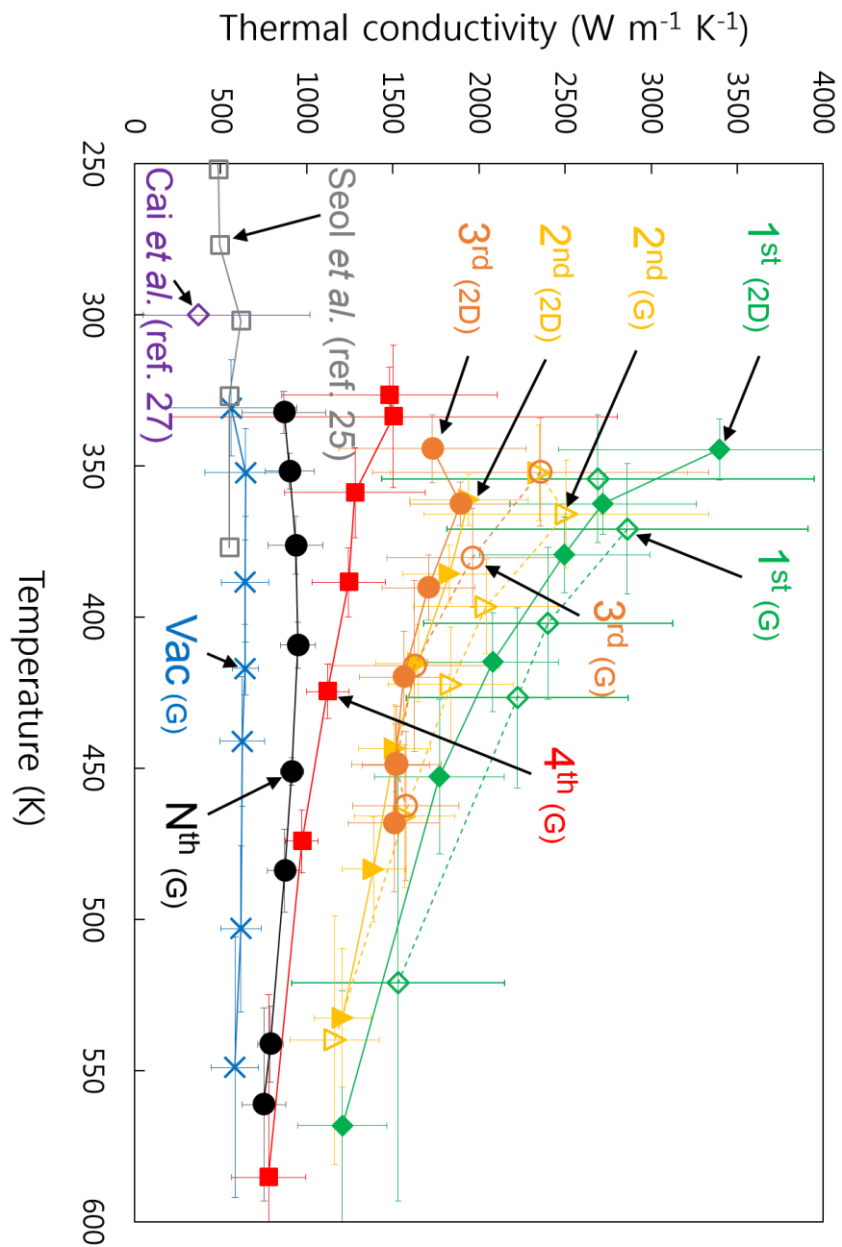


Figure 4.11 Thermal conductivity of supported graphene at various temperatures for 1<sup>st</sup>, 2<sup>nd</sup>, 3<sup>rd</sup>, 4<sup>th</sup>, N<sup>th</sup>, and VAC samples, using either Raman G or 2D peaks.

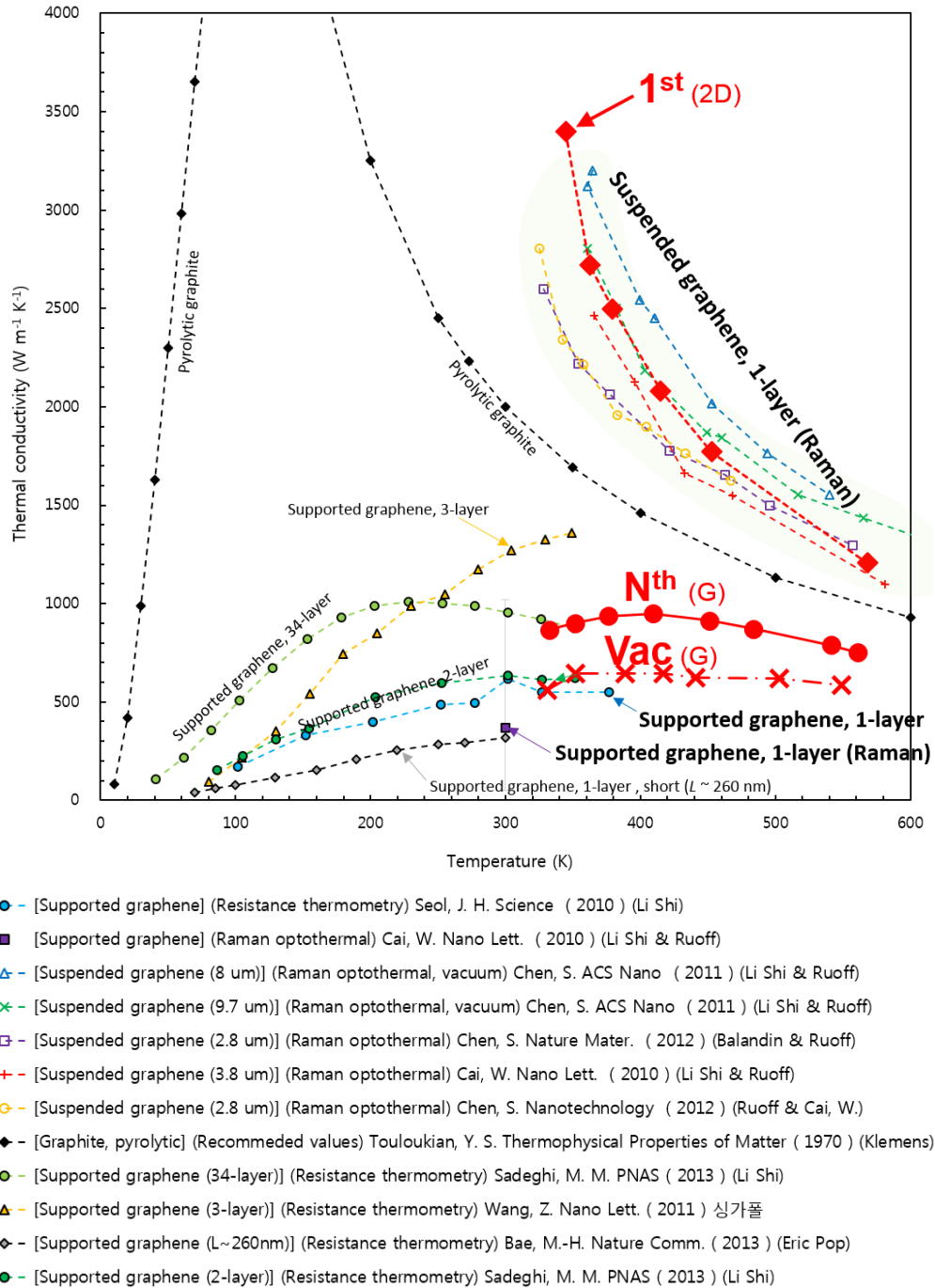


Figure 4.12 Comparison of thermal conductivity values with previous works.

## **Chapter 5**

# **Effect of Graphene-Substrate Interactions on Thermal Conductivity of Supported Graphene**

### **5.1 Introduction**

Thermal conductivity of supported graphene has been hitherto considered as a single-valued property for a given temperature, while our optothermal measurement of supported graphene with various pre-annealing conditions clearly shows that  $k_g$  is not only a variable of temperature, but also of number of annealing and of pressure condition, as discussed in Chapter 4.

In this chapter we attempt to explain the effect of pre-annealing on thermal conductivity of supported graphene. We show that repeated thermal annealing enhances the graphene-substrate conformity, firstly, by investigating the positions of Raman G and 2D peaks at room temperature condition for the supported graphene samples as regards their charge carrier concentration, and secondly, by comparing the temperature dependence of Raman G and 2D peaks. Analysis of interfacial dynamic constants based on elastic theory and equation of states reveals that enhanced graphene-substrate conformity results in an increase in the substrate-induced phonon scattering rate of supported graphene, thereby reducing its basal plane thermal conductivity.

## **5.2 Effect of thermal annealing on graphene-substrate conformity**

Previous atomic force microscopy and scanning tunneling microscopy studies revealed that the surface of a thermally grown amorphous SiO<sub>2</sub> substrate consists of various topological features, including protrusions, depressions, and corrugations. Typical SiO<sub>2</sub> surface exhibits an average root-mean-square roughness ranging from 0.168 nm (Lui et al., 2009) to 0.37 nm (Cullen et al., 2009) and an average correlation length between peaks ranging from 16 nm (Ishigami et al., 2007) to 22 nm (Lui et al., 2009). Due to the extremely thin cross sectional area and mechanical strength, supported graphene ‘partially’ adheres to the SiO<sub>2</sub> surface, closely resembling the topological features of the substrate (Ishigami et al., 2007; Geringer et al., 2009; Lui et al., 2009; Cullen et al., 2010; Bunch and Dunn, 2012; Yamamoto et al., 2012).

It is known from various experimental studies reported that the degree of conformity of graphene to the substrate increases as a result of thermal annealing, resulting in increased area of contact and decreased average separation distance between graphene and the substrate (Ishigami et al., 2007; Liu et al., 2008; Ryu et al., 2010; Song and Cho, 2010; Cheng et al., 2011; Lee et al., 2012; Kumar et al., 2013). The effect of heating on graphene-substrate conformity is understood as a transition between metastable states of varying degree of adhesions, whereas the most stable configuration of graphene on substrate should exhibit the minimum

energy of formation, and annealing provides the energy to overcome the ‘potential barrier’ between the metastable states. Indeed, a theoretical study based on elastic theory of membrane has revealed that multiple numbers of supported graphene configurations in equilibrium are possible for a given geometry of the substrate, and transition between ‘pinned’ and ‘de-pinned’ state is determined by the energy cost to overcome bending and strain of the supported graphene (Kusminskiy et al., 2011).

#### **5.2.1 Height ratio and FWHM of Raman peaks**

As shown in Figure 5.2, repeated thermal annealing resulted in a decrease in height ratio between Raman 2D to G peaks, as well as broadening of the 2D peak. It is in good agreement with the previous reports where thermal pre-annealing was implemented before Raman measurements of supported graphene (Das et al., 2008; Ryu et al., 2010).

#### **5.2.2 Charge carrier concentration of supported graphene**

Enhanced graphene-substrate conformity of supported graphene in atmospheric condition is manifested by the increase in positive charge carrier (‘hole’), as recent studies suggest (Das et al., 2008; Ryu et al., 2010; Cheng et al., 2011; Gammelgaard et al., 2014). Increased hole concentration is explained as a result of increased area of graphene-substrate contact points, where attraction of ambient molecules including O<sub>2</sub> and H<sub>2</sub>O, that contribute to p-type charge carriers,

are encouraged due to increased reactivity of graphene, as shown in Figure 5.1 (a).

To investigate the p-type charge carrier concentrations of our supported graphene samples with different number of thermal annealing, a vector analysis in Raman  $\omega_G$ -  $\omega_{2D}$  space has been conducted, method of which has been proposed by Lee et al. (2012). It has been observed that change in p-type carrier concentration ( $\Delta n_p$ ) expedites a shift of Raman G and 2D peak positions simultaneously (Das et al., 2008), with the ratio of position change between G and 2D peaks showing a constant value

$$\frac{\Delta\omega_{2D}}{\Delta\omega_G} = 0.7 \quad (5.1)$$

At constant temperature condition, another source of Raman G and 2D peak shift is the magnitude of the residual strain of the supported graphene, where the ratio between  $\Delta\omega_G$  and  $\Delta\omega_{2D}$  is

$$\frac{\Delta\omega_{2D}}{\Delta\omega_G} = 2.2 \quad (5.2)$$

The changes in p-doping and residual strain have discriminable slopes in the  $\omega_G$ - $\omega_{2D}$  map by Eqs. (5.1) and (5.2), allowing for determining the degree of p-doping by a vector decomposition of Raman G and 2D peak shifts.

The  $\omega_G$  and  $\omega_{2D}$  data for our samples 1<sup>st</sup> to N<sup>th</sup> were measured at room

temperature in atmospheric condition, as shown in Figure 5.3. Vector decomposition between the samples clearly shows that the concentration of p-type charge carriers gradually increases as thermal annealing is repeated, resulting in a very strong p-doping of N<sup>th</sup> sample ( $\Delta n_p \sim 10^{13} \text{ cm}^{-2}$ ), indicating that the graphene-substrate conformity have increased accordingly.

### **5.2.3 Increase in temperature coefficients of Raman peaks as a result of thermal annealing**

The difference in the temperature dependence of Raman peaks between samples 1<sup>st</sup> to N<sup>th</sup>, also supports that repeated thermal annealing enhanced the graphene-substrate conformity, as shown in Figure 5.4. As discussed in Section 4.4.2, Raman shift of a supported graphene is attributed to the intrinsic anharmonicity of graphene and the external effect of thermal expansion mismatch between the graphene and the SiO<sub>2</sub> substrate. For a suspended graphene, which is free of external strain, the temperature coefficient originates from the intrinsic anharmonicity, where the experiment for a suspended graphene (Calizo et al., 2007) and the theoretical study for a graphene that is free of external interactions (Bonini et al., 2007) showed a good agreement in the temperature coefficient of Raman G peak of graphene of  $-0.016 \text{ cm}^{-1}/\text{K}$ , approximately.

While the temperature coefficients of Raman G peaks for 1<sup>st</sup>, 2<sup>nd</sup>, and 3<sup>rd</sup> samples (Table 4.1) are comparable to that of suspended graphene, 4<sup>th</sup>, N<sup>th</sup>, and VAC shows a significantly larger magnitude of Raman shift for a given amount of



temperature change, as could be seen in Figure 5.4. This implies that supported graphene samples thermally annealed to a lesser degree (1<sup>st</sup>, 2<sup>nd</sup>, and 3<sup>rd</sup>) are relatively free to expand and contract on the substrate as temperature changes, while thoroughly annealed samples are strongly bound to the substrate, as the larger proportion of thermal expansion mismatch strain induced Raman shift suggest.

### **5.3 Effect of graphene-substrate separation distance on thermal conductivity**

Assuming an infinitely thin graphene membrane in the proximity of a SiO<sub>2</sub> substrate with sinusoidal corrugations as shown in Figure 5.5, the equilibrium configuration of the graphene for a given topology of the substrate is determined by minimizing the total free-energy of the system. Following the method reported by Aitken and Huang (2010), for a various set of parameters  $\delta_s$ ,  $\lambda$  (corrugation amplitude and wavelength of the substrate, respectively), and  $\varepsilon$  (built-in strain), the degree-of-conformation parameters  $\delta_g$  (corrugation amplitude of the graphene) and  $h$  (mean separation distance) could be obtained, and the resulting dynamic constants ( $K_{vdW}$ ) has been evaluated as the second derivative of the van der Waals (vdW) energy of the system, as shown in Figure 5.6. Here, Young's modulus and bending stiffness of graphene was assumed to be 352.8 N/m and  $2.392 \times 10^{-19}$  N m, respectively. Also  $h_0 = 6.0 \times 10^{-10}$  m was used for equilibrium separation

between flat graphene and flat SiO<sub>2</sub> substrate and  $\Gamma_0 = 0.0961 \text{ J/m}^2$  for its equilibrium van der Waals energy per unit area. Since  $|K_{\text{vdW}}|^2$  is proportional to the phonon scattering rate of the graphene that is induced by the substrate interaction (Seol et al., 2010), it could be inferred from our analysis that an increase in graphene-substrate conformity (i.e. a decrease in  $h$  or an increase in  $\delta_g$ ) results in a decrease in thermal conductivity of a supported graphene, which is in agreement with our experimental observations. See Appendix B for details in numerical implementation using MATLAB.

#### **5.4 Effect of intercalated layer of water on thermal conductivity**

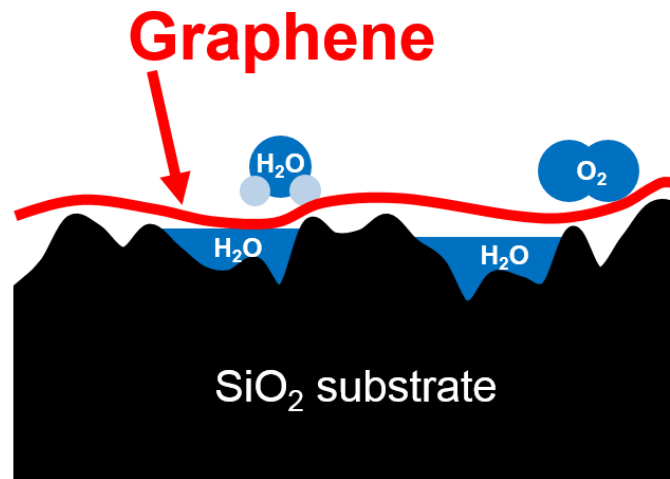
The effect of a possible layer of H<sub>2</sub>O molecules intercalated between the graphene and the substrate has been investigated. It has been recently reported that a layer of water formed between graphene and SiO<sub>2</sub> remains stable under ambient atmosphere despite the hydrophobicity of graphene (Lee et al., 2014), in accordance with the wide consensus that the existence of a water layer in-between is possible (Schedin et al., 2007; Sabio et al., 2008). Since the preparation of our supported graphene sample had involved a series of wet transfer processes in a deionized water, it is feasible that a significant amount of H<sub>2</sub>O molecules had been confined within the graphene-SiO<sub>2</sub> interface, dehydrating upon thermal annealing. To simplify the analysis, a graphene over an ideally flat substrate without any topological features has been assumed, and the compressibility of the

intercalated H<sub>2</sub>O layer is determined from the Tait equation of state (Gilvarry, 1957). By varying the amount of H<sub>2</sub>O, the equilibrium separation distance ( $h$ ) and the net force constant ( $K_{\text{net}}$ ) is determined from the force balance between the atmospheric pressure ( $F_1$ ), graphene-substrate vdW interaction ( $F_{\text{vdW}}$ ), and the internal pressure exerted by the H<sub>2</sub>O layer ( $F_2$ ) with respect to the graphene membrane as illustrated in Figure 5.7. As plotted in Figure 5.8, due to a decrease in  $h$  as a result of dehydration of intercalated H<sub>2</sub>O from thermal annealing,  $K_{\text{net}}$  increases, thereby reducing the thermal conductivity of a supported graphene. It has also been explained theoretically that the adhesion energy of graphene/water/SiO<sub>2</sub> is expected to be considerably lower than that of graphene/SiO<sub>2</sub> (Gao et al., 2014), indicating that removal of a water layer by thermal annealing could also contribute to decrease in graphene thermal conductivity. We notice that the possible presence of an intercalated water layer and its dehydration is not in contradiction with our observations on the increase in p-type charge carrier concentration as a result of thermal annealing (Figure 5.3), where a layer of H<sub>2</sub>O is known to decouple the charge transfer from the substrate to the graphene (Shim et al., 2012). See Appendix C for details in numerical implementation using MATLAB.

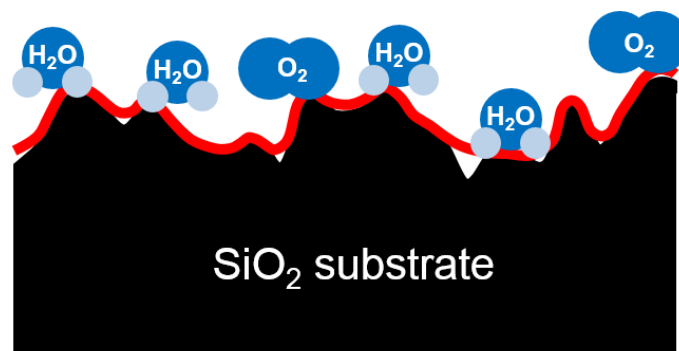
## 5.5 Conclusion

The reduction of supported graphene thermal conductivity with repeated

thermal pre-annealing is attributed to the increased graphene-substrate conformity which in turn enhances the substrate-induced phonon scattering rate of graphene. The increased graphene-substrate conformity was manifested through both the change in charge carrier concentration of graphene, and the increase in thermal expansion mismatch strain between graphene and the substrate. Qualitative analysis based on elastic theory shows that phonon scattering rate increases as graphene-substrate separation distance decreases, resulting in a decrease in thermal conductivity. The effect of a possible intercalated water layer also has been investigated, where dehydration due to thermal annealing leads to stronger net force constant enacting on the graphene, and consequently reducing the thermal conductivity of graphene.



**As prepared**



**After annealing**

Figure 5.1 Schematic comparison of supported graphene as prepared (above), and after annealing (below).

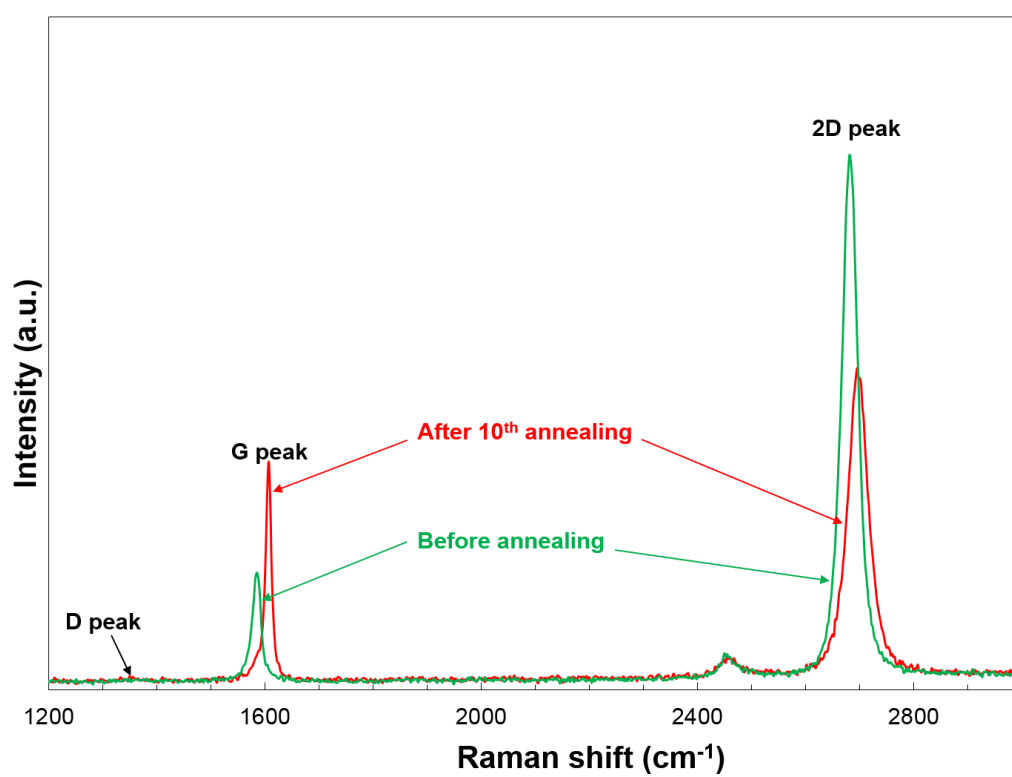


Figure 5.2 Raman spectra of supported graphene as prepared and after 10<sup>th</sup> thermal annealing. Notice the significant decrease in the ratio of height between Raman 2D and G peaks.

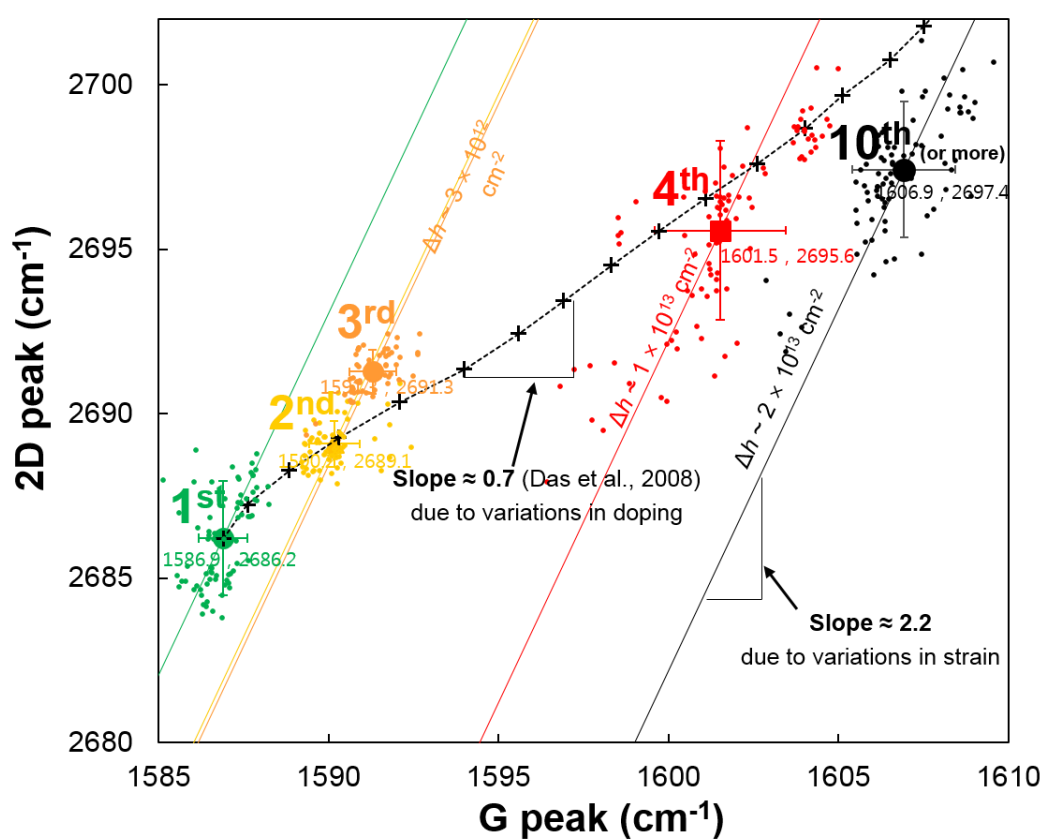


Figure 5.3 Raman peak positions of supported graphene samples with varying degree of thermal pre-annealing, measured at room temperature in atmospheric conditions. By vector decomposition of the p-doping components (slope = 0.7) and the strain component (slope = 2.2), difference in positive charge carrier concentrations between the samples could be estimated.

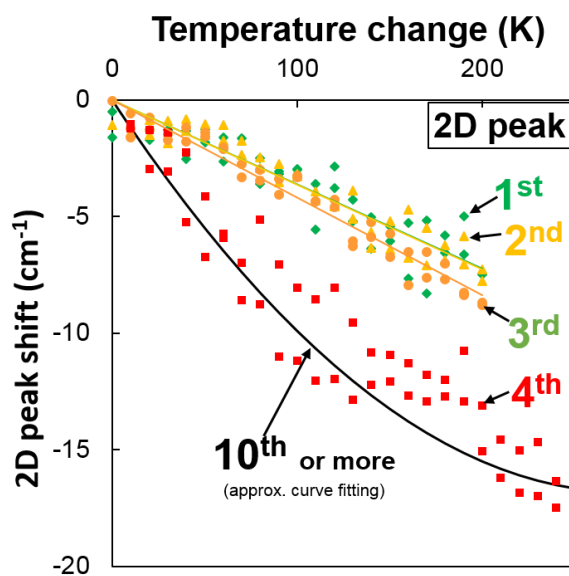
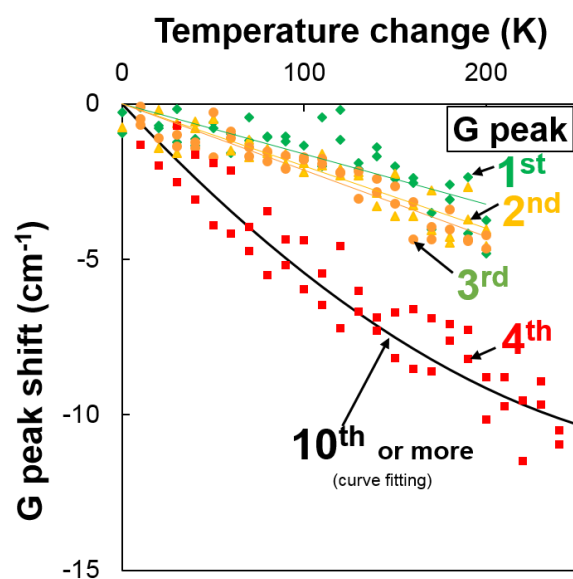


Figure 5.4 Comparison of the temperature dependence of Raman G (above) and 2D (below) peaks of supported graphene samples with varying degree of thermal pre-annealing.



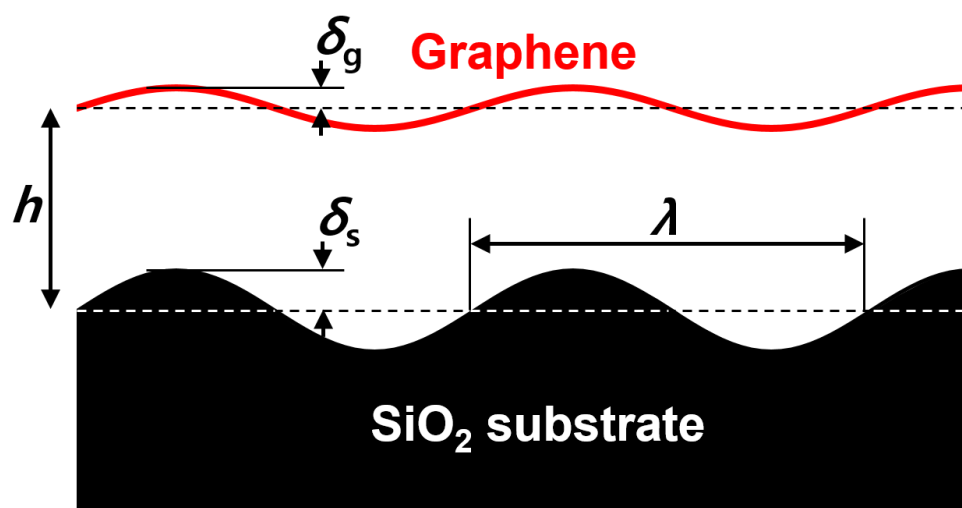


Figure 5.5 Schematic representation of the simplified model for a supported graphene over a substrate with a sinusoidal corrugations.

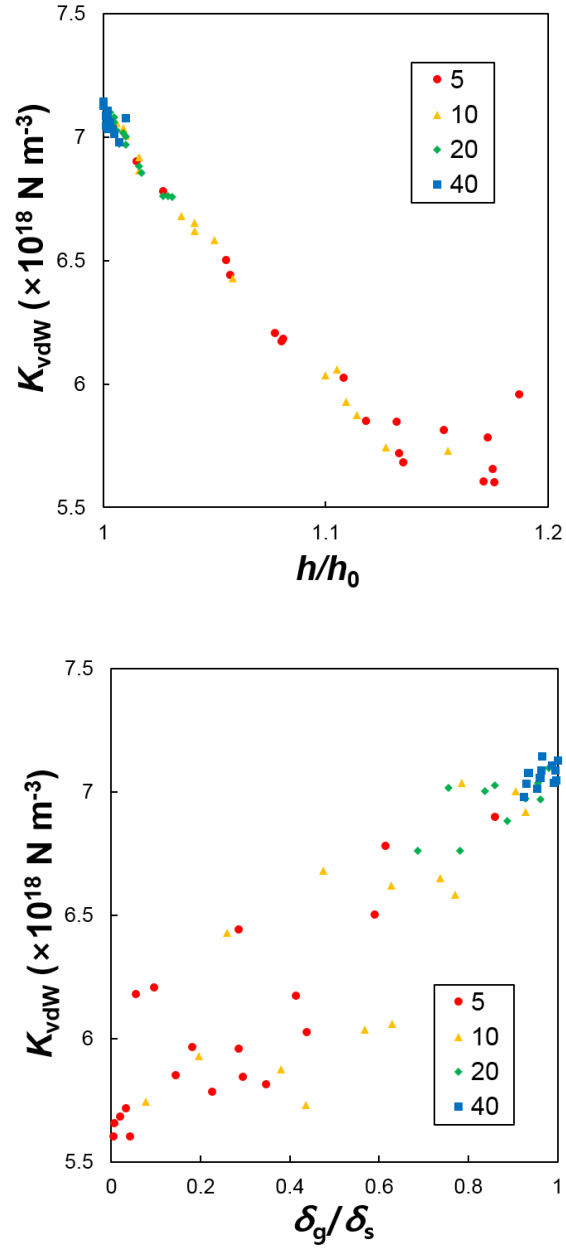


Figure 5.6 Relations between the force constant and the degree of conformation parameters,  $h$  and  $\delta_g$ . Here,  $h_0$  is the equilibrium distance between a flat graphene and a flat substrate free of corrugation and strain.

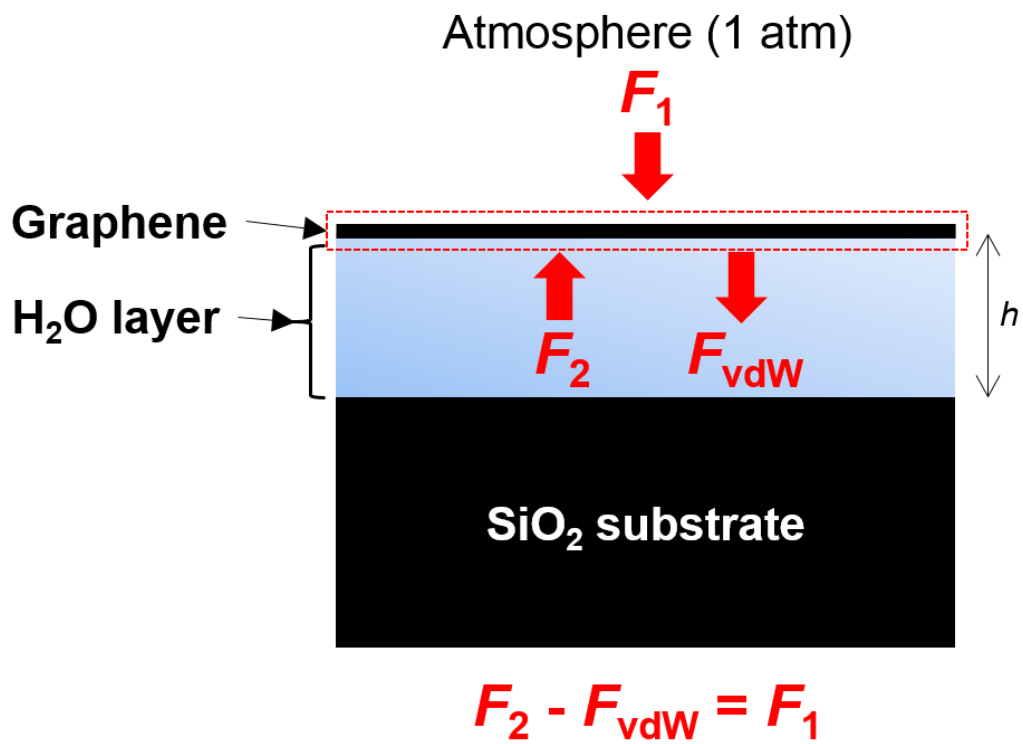


Figure 5.7 Schematic of the balance between the forces enacting over a supported monolayer graphene with an intercalated layer of H<sub>2</sub>O, where  $F_1$  is the downward force due to the ambient atmospheric pressure,  $F_2$  is the compressive force exerted by the H<sub>2</sub>O layer, and  $F_{vdW}$  is the attractive force induced by the graphene-substrate van der Waals interaction.

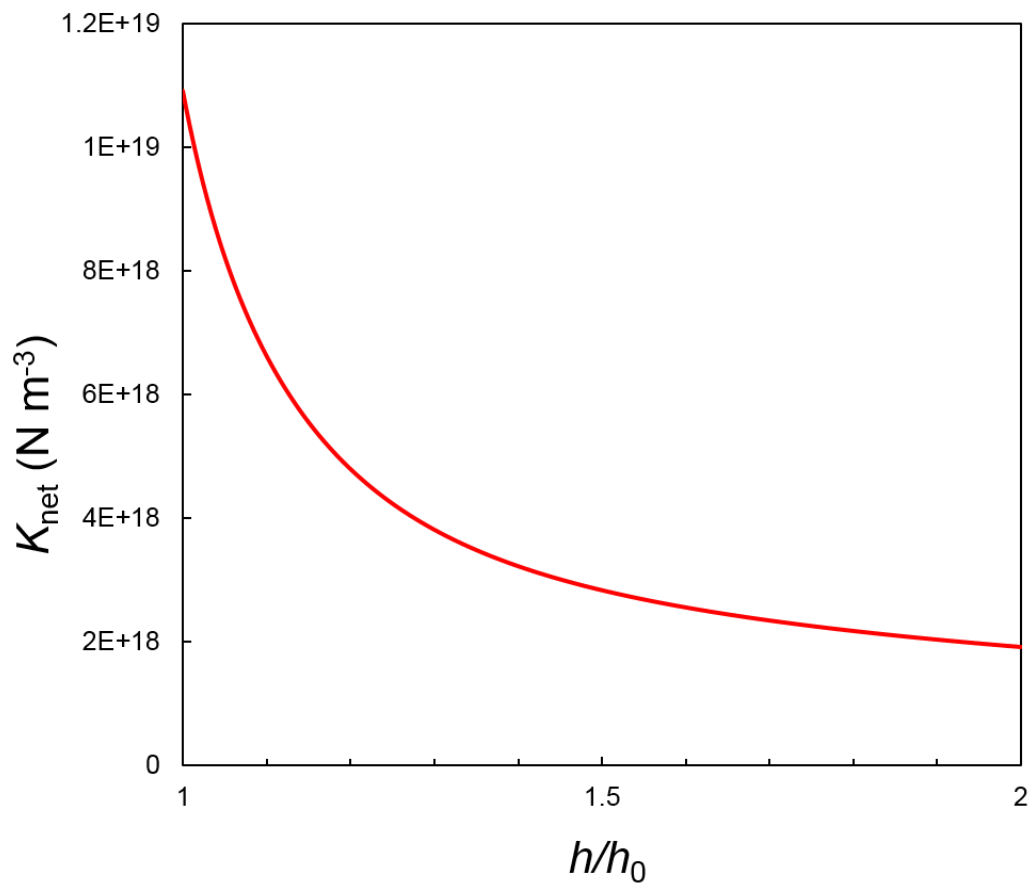


Figure 5.8 Net force constant ( $K_{\text{net}}$ ) as a function of normalized separation distance between graphene and  $\text{SiO}_2$  substrate with intercalated  $\text{H}_2\text{O}$  layer in between.

## **Chapter 6**

### **Summary and Conclusions**

Thermal conductivity of supported CVD monolayer graphene in contact with SiO<sub>2</sub> substrate from 350 K to 600 K has been measured by optothermal Raman technique with significantly improved measurement accuracy. The thermal conductivity of supported showed a strong decreasing behavior as thermal pre-annealing was repeated, which is attributed to enhanced graphene-substrate conformity and increased substrate-induced phonon scattering.

In Chapter 2, a 3D heat transfer model accounting for the spatial temperature distribution of optothermal Raman measurements of supported graphene has been developed. Numerical analysis showed the inadequacy of the previous 2D heat transfer model assuming a constant value cross-plane heat transfer coefficient at the interface of graphene-substrate, resulting in a significant overestimation of the measured thermal conductivity value. By minimizing the thickness of the substrate, 3D heat transfer model demonstrates that optothermal Raman technique robustly determines the thermal conductivity of supported graphene, regardless of the uncertainties in the thermal boundary conductance and thermal conductivity of SiO<sub>2</sub>.

In Chapter 3, detailed sample preparation procedures has been presented. High quality monolayer graphene has been synthesized by CVD method with copper

foil as the catalyst substrate, followed by a transfer of graphene to the target 8-nm-thick SiO<sub>2</sub> substrate applying the PMMA transfer technique. The characteristics and quality of CVD graphene have been examined by optical microscopy, SEM, XPS, and Raman spectroscopy techniques. Characterization of the sample has shown that the synthesized CVD graphene is large-area monolayer-dominant and free of major cracks and structural defects, with sufficiently large grain sizes.

In Chapter 4, optothermal Raman technique devised in Chapter 2 was implemented over the supported graphene sample prepared in Chapter 3. Effective absorbance, temperature vs Raman peak positions, and laser power vs. Raman peak positions have been measured. Tabulated one-to-one correspondence between thermal conductivity ( $k_g$ ) and measured temperature difference divided by laser power ( $\Delta T_m/P_L$ ), thermal conductivity values of supported graphene under varying degrees of thermal pre-annealing have been plotted against the measured temperatures. To the best of our knowledge, we are the first to report the thermal conductivity values of supported monolayer graphene at temperatures higher than 400 K, understanding of which is essential in practical device applications and thermal management of graphene.

The strong dependence of supported graphene thermal conductivity on pre-annealing condition has never been observed before. In Chapter 5, vector decomposition in Raman G-2D space has revealed that repeated thermal annealing resulted in gradual increase in p-type charge carrier concentrations of supported

graphene samples. The comparison of temperature coefficients of Raman peaks between samples showed that repeated annealing resulted in increased thermal expansion mismatch induced strain of graphene, indicating the enhanced graphene-substrate conformity. Analysis based on elastic theory of membrane has been conducted to investigate the effect of graphene-substrate conformity on thermal conductivity. The decrease in thermal conductivity with thermal annealing was attributed to the corresponding increase in net dynamic constant of the graphene-substrate interaction, which in turn increase the substrate induced phonon scattering of graphene.

The optothermal Raman technique developed in this work has been successfully applied in measuring the thermal conductivity of supported graphene at high temperature regimes. Due to its simplicity and reliability, we believe that our method will encourage extensive studies on thermal properties of two-dimensional materials for device applications.

We experimentally demonstrated that the thermal conductivity of supported graphene depends on thermal pre-treatment as well as temperature. This could offer an alternative route to modulating the thermal conductivity of supported graphene by controlling its thermo-mechanical affiliation without inducing any structural defects.

## References

Aitken, Z. H. & Huang, R. 2010, Effects of mismatch strain and substrate surface corrugation on morphology of supported monolayer graphene. *Journal of Applied Physics*, 107.

Bae, M. H., Li, Z. Y., Aksamija, Z., Martin, P. N., Xiong, F., Ong, Z. Y., Knezevic, I. & Pop, E. 2013, Ballistic to diffusive crossover of heat flow in graphene ribbons. *Nature Communications*, 4.

Balandin, A. A. 2011, Thermal properties of graphene and nanostructured carbon materials. *Nature Materials*, 10, 569-581.

Balandin, A. A., Ghosh, S., Bao, W. Z., Calizo, I., Teweldebrhan, D., Miao, F. & Lau, C. N. 2008, Superior thermal conductivity of single-layer graphene. *Nano Letters*, 8, 902-907.

Bao, W. Z., Miao, F., Chen, Z., Zhang, H., Jang, W. Y., Dames, C. & Lau, C. N. 2009, Controlled ripple texturing of suspended graphene and ultrathin graphite membranes. *Nature Nanotechnology*, 4, 562-566.



Bolotin, K. I., Sikes, K. J., Jiang, Z., Klima, M., Fudenberg, G., Hone, J., Kim, P. & Stormer, H. L. 2008, Ultrahigh electron mobility in suspended graphene. *Solid State Communications*, 146, 351-355.

Bonini, N., Lazzeri, M., Marzari, N. & Mauri, F. 2007, Phonon anharmonicities in graphite and graphene. *Physical Review Letters*, 99.

Bunch, J. S. & Dunn, M. L. 2012, Adhesion mechanics of graphene membranes. *Solid State Communications*, 152, 1359-1364.

Cai, W. W., Moore, A. L., Zhu, Y. W., Li, X. S., Chen, S. S., Shi, L. & Ruoff, R. S. 2010, Thermal Transport in Suspended and Supported Monolayer Graphene Grown by Chemical Vapor Deposition. *Nano Letters*, 10, 1645-1651.

Calizo, I., Balandin, A. A., Bao, W., Miao, F. & Lau, C. N. 2007, Temperature dependence of the Raman spectra of graphene and graphene multilayers. *Nano Letters*, 7, 2645-2649.

Castro Neto, A. H., Guinea, F., Peres, N. M. R., Novoselov, K. S. & Geim, A. K. 2009, The electronic properties of graphene. *Reviews of Modern Physics*, 81, 109-162.

Chen, J., Zhang, G. & Li, B. W. 2013, Substrate coupling suppresses size dependence of thermal conductivity in supported graphene. *Nanoscale*, 5, 532-536.

Chen, S. S., Li, Q. Y., Zhang, Q. M., Qu, Y., Ji, H. X., Ruoff, R. S. & Cai, W. W. 2012, Thermal conductivity measurements of suspended graphene with and without wrinkles by micro-Raman mapping. *Nanotechnology*, 23.

Chen, S. S., Moore, A. L., Cai, W. W., Suk, J. W., An, J. H., Mishra, C., Amos, C., Magnuson, C. W., Kang, J. Y., Shi, L. & Ruoff, R. S. 2011, Raman Measurements of Thermal Transport in Suspended Monolayer Graphene of Variable Sizes in Vacuum and Gaseous Environments. *Acs Nano*, 5, 321-328.

Chen, S. S., Wu, Q. Z., Mishra, C., Kang, J. Y., Zhang, H. J., Cho, K. J., Cai, W. W., Balandin, A. A. & Ruoff, R. S. 2012, Thermal conductivity of isotopically modified graphene. *Nature Materials*, 11, 203-207.

Cullen, W. G., Yamamoto, M., Burson, K. M., Chen, J. H., Jang, C., LI, L., Fuhrer, M. S. & Williams, E. D. 2010, High-Fidelity Conformation of Graphene to SiO<sub>2</sub> Topographic Features. *Physical Review Letters*, 105.

Faugeras, C., Faugeras, B., Orlita, M., Potemski, M., Nair, R. R. & Geim, A. K. 2010, Thermal Conductivity of Graphene in Corbino Membrane Geometry. *Acs*

*Nano*, 4, 1889-1892.

Ferrari, A. C. 2007, Raman spectroscopy of graphene and graphite: Disorder, electron-phonon coupling, doping and nonadiabatic effects. *Solid State Communications*, 143, 47-57.

Ferrari, A. C. & Basko, D. M. 2013, Raman spectroscopy as a versatile tool for studying the properties of graphene. *Nature Nanotechnology*, 8, 235-246.

Ferrari, A. C., Meyer, J. C., Scardaci, V., Casiraghi, C., Lazzeri, M., Mauri, F., Piscanec, S., Jiang, D., Novoselov, K. S., Roth, S. & Geim, A. K. 2006, Raman spectrum of graphene and graphene layers. *Physical Review Letters*, 97.

Fugallo, G., Cepellotti, A., Paulatto, L., Lazzeri, M., Marzari, N. & Mauri, F. 2014, Thermal Conductivity of Graphene and Graphite: Collective Excitations and Mean Free Paths. *Nano Letters*, 14, 6109-6114.

Gao, W., Xiao, P. H., Henkelman, G., Liechti, K. M. & Huang, R. 2014, Interfacial adhesion between graphene and silicon dioxide by density functional theory with van der Waals corrections. *Journal of Physics D-Applied Physics*, 47.

Geim, A. K. & Grigorieva, I. V. 2013, Van der Waals heterostructures. *Nature*,

499, 419-425.

Geringer, V., Liebmann, M., Echtermeyer, T., Runte, S., Schmidt, M., Ruckamp, R., Lemme, M. C. & Morgenstern, M. 2009, Intrinsic and extrinsic corrugation of monolayer graphene deposited on SiO<sub>2</sub>. *Physical Review Letters*, 102.

Gilvarry, J. J. 1957, Temperature-Dependent Equations of State of Solids. *Journal of Applied Physics*, 28, 1253-1261.

Hu, X. J., Jain, A. & Goodson, K. E. 2008, Investigation of the natural convection boundary condition in microfabricated structures. *International Journal of Thermal Sciences*, 47, 820-824.

Huang, P. Y., Ruiz-Vargas, C. S., van der Zande, A. M., Whitney, W. S., Levendorf, M. P., Kevek, J. W., Garg, S., Alden, J. S., Hustedt, C. J., Zhu, Y., Park, J., McEuen, P. L. & Muller, D. A. 2011, Grains and grain boundaries in single-layer graphene atomic patchwork quilts. *Nature*, 469, 389.

Ishigami, M., Chen, J. H., Cullen, W. G., Fuhrer, M. S. & Williams, E. D. 2007, Atomic structure of graphene on SiO<sub>2</sub>. *Nano Letters*, 7, 1643-1648.

Kim, E., Shim, H. W., Unithrattil, S., Kim, Y. H., Choi, H., Ahn, K. J., Kwak, J.

S., Kim, S., Yoon, H. & Bin Im, W. 2016, Effective Heat Dissipation from Color-Converting Plates in High-Power White Light Emitting Diodes by Transparent Graphene Wrapping. *Acs Nano*, 10, 238-245.

Kim, K. J. & King, W. P. 2009, Thermal conduction between a heated microcantilever and a surrounding air environment. *Applied Thermal Engineering*, 29, 1631-1641.

Kim, S. M., Hsu, A., Lee, Y. H., Dresselhaus, M., Palacios, T., Kim, K. K. & Kong, J. 2013, The effect of copper pre-cleaning on graphene synthesis. *Nanotechnology*, 24.

Kusminskiy, S. V., Campbell, D. K., Castro Neto, A. H. & Guinea, F. 2011, Pinning of a two-dimensional membrane on top of a patterned substrate: The case of graphene. *Physical Review B*, 83.

Lee, C., Wei, X. D., Kysar, J. W. & Hone, J. 2008, Measurement of the elastic properties and intrinsic strength of monolayer graphene. *Science*, 321, 385-388.

Lee, D., Ahn, G. & Ryu, S. 2014, Two-Dimensional Water Diffusion at a Graphene-Silica Interface. *Journal of the American Chemical Society*, 136, 6634-6642.

Lee, J. E., Ahn, G., Shim, J., Lee, Y. S. & Ryu, S. 2012, Optical separation of mechanical strain from charge doping in graphene. *Nature Communications*, 3.

Lee, J. U., Yoon, D., Kim, H., Lee, S. W. & Cheong, H. 2011, Thermal conductivity of suspended pristine graphene measured by Raman spectroscopy. *Physical Review B*, 83.

Lee, S., Broido, D., Esfarjani, K. & Chen, G. 2015, Hydrodynamic phonon transport in suspended graphene. *Nature Communications*, 6.

Lee, W., Kihm, K. D., Kim, H. G., Shin, S., Lee, C., Park, J. S., Cheon, S., Kwon, O. M., Lim, G. & Lee, W. 2017, In-Plane Thermal Conductivity of Polycrystalline Chemical Vapor Deposition Graphene with Controlled Grain Sizes. *Nano Letters*, 17, 2361-2366.

Lee, Y., Pak, A. J., Paek, E. & Hwang, G. S. 2015, Principal Role of Contact-Force Distribution in Determining the Thermal Conductivity of Supported Graphene. *Physical Review Applied*, 4.

Lewis, A. M., Derby, B. & Kinloch, I. A. 2013, The Influence of Gas Phase Equilibria on the Chemical Vapor Deposition of Graphene. *Acs Nano*.

Li, X. S., Cai, W. W., An, J. H., Kim, S., Nah, J., Yang, D. X., Piner, R., Velamakanni, A., Jung, I., Tutuc, E., Banerjee, S. K., Colombo, L. & Ruoff, R. S. 2009, Large-Area Synthesis of High-Quality and Uniform Graphene Films on Copper Foils. *Science*, 324, 1312-1314.

Li, X. S., Cai, W. W., Colombo, L. & Ruoff, R. S. 2009, Evolution of Graphene Growth on Ni and Cu by Carbon Isotope Labeling. *Nano Letters*, 9, 4268-4272.

Li, Z. Y., Bae, M. H. & Pop, E. 2014, Substrate-supported thermometry platform for nanomaterials like graphene, nanotubes, and nanowires. *Applied Physics Letters*, 105.

Lindsay, L., Broido, D. A. & Mingo, N. 2010, Flexural phonons and thermal transport in graphene. *Physical Review B*, 82.

Liu, L., Ryu, S. M., Tomasik, M. R., Stolyarova, E., Jung, N., Hybertsen, M. S., Steigerwald, M. L., Brus, L. E. & Flynn, G. W. 2008, Graphene oxidation: Thickness-dependent etching and strong chemical doping. *Nano Letters*, 8, 1965-1970.

Lui, C. H., Liu, L., Mak, K. F., Flynn, G. W. & Heinz, T. F. 2009, Ultraflat

graphene. *Nature*, 462, 339-341.

Mak, K. F., Lui, C. H. & Heinz, T. F. 2010, Measurement of the thermal conductance of the graphene/SiO<sub>2</sub> interface. *Applied Physics Letters*, 97.

Mattevi, C., Kim, H. & Chhowalla, M. 2011, A review of chemical vapour deposition of graphene on copper. *Journal of Materials Chemistry*, 21, 3324-3334.

Mehdipour, H. & Ostrikov, K. 2012, Kinetics of Low-Pressure, Low-Temperature Graphene Growth: Toward Single-Layer, Single-Crystalline Structure. *Acs Nano*, 6, 10276-10286.

Metten, D., Federspiel, F., Romeo, M. & Berciaud, S. 2014, All-Optical Blister Test of Suspended Graphene Using Micro-Raman Spectroscopy. *Physical Review Applied*, 2.

Mounet, N. & Marzari, N. 2005, First-principles determination of the structural, vibrational and thermodynamic properties of diamond, graphite, and derivatives. *Physical Review B*, 71.

Nair, R. R., Blake, P., Grigorenko, A. N., Novoselov, K. S., Booth, T. J., Stauber, T., Peres, N. M. R. & Geim, A. K. 2008, Fine structure constant defines visual



transparency of graphene. *Science*, 320, 1308-1308.

NIST, 1991, Standard Reference Material 739 Certificate; National Institute of Standards and Technology: Gaithersburg MD.

Novoselov, K. S., Fal'ko, V. I., Colombo, L., Gellert, P. R., Schwab, M. G. & Kim, K. 2012, A roadmap for graphene. *Nature*, 490, 192-200.

Novoselov, K. S., Geim, A. K., Morozov, S. V., Jiang, D., Zhang, Y., Dubonos, S. V., Grigorieva, I. V. & Firsov, A. A. 2004, Electric field effect in atomically thin carbon films. *Science*, 306, 666-669.

Novoselov, K. S., Mishchenko, A., Carvalho, A. & Neto, A. H. C. 2016, 2D materials and van der Waals heterostructures. *Science*, 353.

Ong, Z. Y. & Pop, E. 2011, Effect of substrate modes on thermal transport in supported graphene. *Physical Review B*, 84.

Persson, B. N. J. & Ueba, H. 2010, Heat transfer between weakly coupled systems: Graphene on a-SiO<sub>2</sub>. *Epl*, 91.

Pettes, M. T., Jo, I. S., Yao, Z. & Shi, L. 2011, Influence of Polymeric Residue on

the Thermal Conductivity of Suspended Bilayer Graphene. *Nano Letters*, 11, 1195-1200.

Pop, E., Varshney, V. & Roy, A. K. 2012. Thermal properties of graphene: Fundamentals and applications. *Mrs Bulletin*, 37, 1273-1281.

Pulavarthy, R. A., Alam, M. T. & Hague, M. A. 2014, Effect of heated zone size on micro and nanoscale convective heat transfer. *International Communications in Heat and Mass Transfer*, 52, 56-60.

Qiu, B. & Ruan, X. L. 2012, Reduction of spectral phonon relaxation times from suspended to supported graphene. *Applied Physics Letters*, 100.

Ryu, S., Liu, L., Berciaud, S., Yu, Y. J., Liu, H. T., Kim, P., Flynn, G. W. & Brus, L. E. 2010, Atmospheric Oxygen Binding and Hole Doping in Deformed Graphene on a SiO<sub>2</sub> Substrate. *Nano Letters*, 10, 4944-4951.

Sabio, J., Seoanez, C., Fratini, S., Guinea, F., Castro, A. H. & Sols, F. 2008, Electrostatic interactions between graphene layers and their environment. *Physical Review B*, 77.

Sadeghi, M. M., Jo, I. & Shi, L. 2013, Phonon-interface scattering in multilayer

graphene on an amorphous support. *Proceedings of the National Academy of Sciences of the United States of America*, 110, 16321-16326.

Sadeghi, M. M., Pettes, M. T. & Shi, L. 2012, Thermal transport in graphene. *Solid State Communications*, 152, 1321-1330.

Schedin, F., Geim, A. K., Morozov, S. V., Hill, E. W., Blake, P., Katsnelson, M. I. & Novoselov, K. S. 2007, Detection of individual gas molecules adsorbed on graphene. *Nature Materials*, 6, 652-655.

Seol, J. H., Jo, I., Moore, A. L., Lindsay, L., Aitken, Z. H., Pettes, M. T., Li, X. S., Yao, Z., Huang, R., Broido, D., Mingo, N., Ruoff, R. S. & Shi, L. 2010, Two-Dimensional Phonon Transport in Supported Graphene. *Science*, 328, 213-216.

Seol, J. H., Moore, A. L., Shi, L., Jo, I. & Yao, Z. 2011, Thermal Conductivity Measurement of Graphene Exfoliated on Silicon Dioxide. *Journal of Heat Transfer-Transactions of the Asme*, 133.

Tang, X. D., Xu, S., Zhang, J. C. & Wang, X. W. 2014, Five Orders of Magnitude Reduction in Energy Coupling across Corrugated Graphene/Substrate Interfaces. *Acs Applied Materials & Interfaces*, 6, 2809-2818.

Touloukian, Y. S., Powell, R. W., Ho, C. Y. & Klemens, P. G. 1970, Thermal Conductivity of Nonmetallic Solids. *Thermophysical Properties of matter* (IFI/Plenum, New York), Vol. 2.

Tuinstra, F. & Koenig, J. L. 1970, Raman Spectrum of Graphite. *Journal of Chemical Physics*, 53, 1126.

Vlassioug, I., Regmi, M., Fulvio, P. F., Dai, S., Datskos, P., Eres, G. & Smirnov, S. 2011, Role of Hydrogen in Chemical Vapor Deposition Growth of Large Single-Crystal Graphene. *Acs Nano*, 5, 6069-6076.

Wang, Y. X., Xu, N., Li, D. Y. & Zhu, J. 2017, Thermal Properties of Two Dimensional Layered Materials. *Advanced Functional Materials*, 27.

Wang, Z. Q., Xie, R. G., Bui, C. T., Liu, D., Ni, X. X., Li, B. W. & Thong, J. T. L. 2011, Thermal Transport in Suspended and Supported Few-Layer Graphene. *Nano Letters*, 11, 113-118.

Xu, X. F., Pereira, L. F. C., Wang, Y., Wu, J., Zhang, K. W., Zhao, X. M., Bae, S., Bui, C. T., Xie, R. G., Thong, J. T. L., Hong, B. H., Loh, K. P., Donadio, D., Li, B. W. & Ozyilmaz, B. 2014, Length-dependent thermal conductivity in suspended single-layer graphene. *Nature Communications*, 5.

Xu, Y., Li, Z. Y. & Duan, W. H. 2014, Thermal and Thermoelectric Properties of Graphene. *Small*, 10, 2182-2199.

Yamamoto, M., Einstein, T. L., Fuhrer, M. S. & Cullen, W. G. 2012, Charge Inhomogeneity Determines Oxidative Reactivity of Graphene on Substrates. *Acs Nano*, 6, 8335-8341.

Yan, Z., Liu, G. X., Khan, J. M. & Balandin, A. A. 2012, Graphene quilts for thermal management of high-power GaN transistors. *Nature Communications*, 3.

Yoon, D., Son, Y. W. & Cheong, H. 2011, Negative Thermal Expansion Coefficient of Graphene Measured by Raman Spectroscopy. *Nano Letters*, 11, 3227-3231.

Zabel, J., Nair, R. R., Ott, A., Georgiou, T., Geim, A. K., Novoselov, K. S. & Casiraghi, C. 2012, Raman Spectroscopy of Graphene and Bilayer under Biaxial Strain: Bubbles and Balloons. *Nano Letters*, 12, 617-621.

Zhang, W. H., Wu, P., Li, Z. Y. & Yang, J. L. 2011, First-Principles Thermodynamics of Graphene Growth on Cu Surfaces. *Journal of Physical Chemistry C*, 115, 17782-17787.

Zhang, Z. K., Du, J. H., Zhang, D. D., Sun, H. D., Yin, L. C., Ma, L. P., Chen, J. S., Ma, D. G., Cheng, H. M. & Ren, W. C. 2017, Rosin-enabled ultraclean and damage-free transfer of graphene for large-area flexible organic light-emitting diodes. *Nature Communications*, 8.

## Appendix

## MATLAB codes for numerical simulations

[illegible]

[illegible]





```

        for j = 1:N
            T(i,j) = T_room;
        end
    end

end

%-----
% Energy balance; Gauss-Seidel
%-----

omega = 1.0;
Tmax = T_room;

% Constants
ktg = kg*tg;

% Coefficients-----
r1 = r(1) - 0.5*dr(1);
r2 = r(1) + 0.5*dr(2);
rr = r(1);

B(1,N) = 0;
C(1,N) = r2*ktg/dr(2);
D(1,N) = rr*(r2-r1)*TBC;
E(1,N) = 0;
F(1,N) = rr*(r2-r1)*hT;

A(1,N) = 1/( B(1,N) + C(1,N) + D(1,N) + E(1,N) + F(1,N) );
G(1,N) = rr*(r2-r1)*q(1);

for i = 2:M
    r1 = r(i) - 0.5*dr(i);
    r2 = r(i) + 0.5*dr(i+1);

```

```

rr = r(i);

B(i,N) = r1*ktg/dr(i);
C(i,N) = r2*ktg/dr(i+1);
D(i,N) = rr*(r2-r1)*TBC;
E(i,N) = 0;
F(i,N) = rr*(r2-r1)*hT;

A(i,N) = 1/( B(i,N) + C(i,N) + D(i,N) + E(i,N) + F(i,N) );
G(i,N) = rr*(r2-r1)*q(i);
end

r1 = r(1) - 0.5*dr(1);
r2 = r(1) + 0.5*dr(2);
rr = r(1);

B(1,N-1) = 0;
C(1,N-1) = r2*(0.5*dz(N-2))*ko/dr(2);
D(1,N-1) = rr*(r2-r1)*ko/dz(N-2);
E(1,N-1) = rr*(r2-r1)*TBC;
F(1,N-1) = 0;

A(1,N-1) = 1/( B(1,N-1) + C(1,N-1) + D(1,N-1) + E(1,N-1) + F(1,N-1) );
G(1,N-1) = 0;

for i = 2:M
    r1 = r(i) - 0.5*dr(i);
    r2 = r(i) + 0.5*dr(i+1);
    rr = r(i);

    B(i,N-1) = r1*(0.5*dz(N-2))*ko/dr(i);

```

```

C(i,N-1) = r2*(0.5*dz(N-2))*ko/dr(i+1);
D(i,N-1) = rr*(r2-r1)*ko/dz(N-2);
E(i,N-1) = rr*(r2-r1)*TBC;
F(i,N-1) = 0;

A(i,N-1) = 1/( B(i,N-1) + C(i,N-1) + D(i,N-1) + E(i,N-1) + F(i,N-1) );
G(i,N-1) = 0;

end

for j = 2:N-2
    r1 = r(1) - 0.5*dr(1);
    r2 = r(1) + 0.5*dr(2);
    rr = r(1);

    B(1,j) = 0;
    C(1,j) = r2*0.5*(dz(j-1) + dz(j))*ko/dr(2);
    D(1,j) = rr*(r2-r1)*ko/dz(j-1);
    E(1,j) = rr*(r2-r1)*ko/dz(j);
    F(1,j) = 0;

    A(1,j) = 1/( B(1,j) + C(1,j) + D(1,j) + E(1,j) + F(1,j) );
    G(1,j) = 0;

    for i = 2:M
        r1 = r(i) - 0.5*dr(i);
        r2 = r(i) + 0.5*dr(i+1);
        rr = r(i);

        B(i,j) = r1*0.5*(dz(j-1) + dz(j))*ko/dr(i);
        C(i,j) = r2*0.5*(dz(j-1) + dz(j))*ko/dr(i+1);
        D(i,j) = rr*(r2-r1)*ko/dz(j-1);

```

```

E(i,j) = rr*(r2-r1)*ko/dz(j);
F(i,j) = 0;

A(i,j) = 1/( B(i,j) + C(i,j) + D(i,j) + E(i,j) + F(i,j) );
G(i,j) = 0;
end
end

r1 = r(1) - 0.5*dr(1);
r2 = r(1) + 0.5*dr(2);
rr = r(1);

B(1,1) = 0;
C(1,1) = r2*(0.5*dz(1))*ko/dr(2);
D(1,1) = 0;
E(1,1) = rr*(r2-r1)*ko/dz(1);
F(1,1) = rr*(r2-r1)*hB;

A(1,1) = 1/( B(1,1) + C(1,1) + D(1,1) + E(1,1) + F(1,1) );
G(1,1) = 0;

for i = 1:M
    r1 = r(i) - 0.5*dr(i);
    r2 = r(i) + 0.5*dr(i+1);
    rr = r(i);

    B(i,1) = r1*(0.5*dz(1))*ko/dr(i);
    C(i,1) = r2*(0.5*dz(1))*ko/dr(i+1);
    D(i,1) = 0;
    E(i,1) = rr*(r2-r1)*ko/dz(1);
    F(i,1) = rr*(r2-r1)*hB;

```

```

    A(i,1) = 1/( B(i,1) + C(i,1) + D(i,1) + E(i,1) + F(i,1) );
    G(i,1) = 0;
end

% Iteration-----
for k = 1:Nk
    T_pre = T;

    T(1,N) = A(1,N)*[ C(1,N)*T(2,N) + D(1,N)*T(1,N-1) + F(1,N)*T_room +
G(1,N) ];
    for i = 2:M-1
        T(i,N) = A(i,N)*[ B(i,N)*T(i-1,N) + C(i,N)*T(i+1,N) +
D(i,N)*T(i,N-1) + F(i,N)*T_room + G(i,N) ];
    end

    T(1,N-1) = A(1,N-1)*[ C(1,N-1)*T(2,N-1) + D(1,N-1)*T(1,N-2) + E(1,N-
1)*T(1,N) ];
    for i = 2:M-1
        T(i,N-1) = A(i,N-1)*[ B(i,N-1)*T(i-1,N-1) + C(i,N-1)*T(i+1,N-1) +
D(i,N-1)*T(i,N-2) + E(i,N-1)*T(i,N) ];
    end

    for j = 2:N-2
        T(1,j) = A(1,j)*[ C(1,j)*T(2,j) + D(1,j)*T(1,j-1) +
E(1,j)*T(1,j+1) ];
        for i = 2:M-1
            T(i,j) = A(i,j)*[ B(i,j)*T(i-1,j) + C(i,j)*T(i+1,j) +
D(i,j)*T(i,j-1) + E(i,j)*T(i,j+1) ];
        end
    end
end

```

```

end

T(1,1) = A(1,1)*[ C(1,1)*T(2,1) + E(1,1)*T(1,2) + F(1,1)*T_room ];
for i = 2 : M-1
    T(i,1) = A(i,1)*[ B(i,1)*T(i-1,1) + C(i,1)*T(i+1,1) +
E(i,1)*T(i,2) + F(i,1)*T_room ];
end

T = T_pre + omega*(T-T_pre);
eps(k) = abs((T(1,N)-Tmax)/Tmax);
Tmax = T(1,N);
Tcenter(k) = Tmax;
end

%-----
% Assessment of measured temperature Tm
%-----

Tm = 0;
for i = 1:M
    rr = r(i);
    r1 = rr - 0.5*dr(i);
    r2 = rr + 0.5*dr(i+1);
    Tm = Tm + pi*T(i,N)*q(i)*(r2^2 - r1^2)/(absorption*Q_total);
end

%-----
% Plot
%-----

for i = 1:k-1
    rNk(i) = i;
end

```

```

Q_conv = 0.0;
for i = 1:M
    r1 = r(i)-0.5*dr(i);
    r2 = r(i)+0.5*dr(i+1);
    Q_conv = Q_conv + (hT*(T(i,N)-T_room) + hB*(T(i,1)-T_room))*pi*(r2^2 -
r1^2);
end
subplot(1,3,1)
semilogx(r,T(:,1),'r', r,T(:,N),'b')
subplot(1,3,2)
loglog(rNk,real(eps(1:k-1)))
subplot(1,3,3)
semilogx(rNk,real(Tcenter(1:k-1)))

T_top = T(1,N)
T_mid = T(1,round(N/2))
T_bottom = T(1,1)
Tm
Convection_contribution = Q_conv/(absorption*Q_total)
R_domain = r(M)
Z_domain = z(N)

```



## Appendix B. Effect of graphene-SiO<sub>2</sub> conformity on force constant

---

```
nu = 0.149;
C = 345/(1-nu^2);    % N/m
D = 1.46*(1.60219*10^-19)/(1-nu^2);    % N*m

G0 = 0.6*(1.60219*10^-1);    % J/m^2
h0 = 0.6*10^-9;    % m
dhn = 0.001;    % user input
hn = [0.7 : dhn : 2];    % normalized h, hn = h/h0
h = hn*h0;
dh = dhn*h0;
M = size(hn,2);

% user input-----
lam = 5*h0;    % 16 ~ 23 nm
dels = 0.6*h0;    % 0.17 ~ 0.37 nm
eps = -0.02    % mismatch strain
%-----

delsn = dels/h0;
ilam = h0/lam;
lamn = lam/h0;

delgn = [0 : 0.001 : 1];    % c2 = 0 ~ 1 : relative amplitude of the
graphene to that of the substrate
delg = h0*delgn;
N = size(delg,2);

for j = 1:N
    Ug(j) = ( 0.25*C*eps*((2*pi/lam)^2) +
```

```

0.25*D*((2*pi/lam)^4) )*(delg(j)^2) + (3*C*((2*pi*delg(j)/lam)^4))/64;
end

for i = 1:M
    ih = h0/h(i);
    q = 2*pi*h(i)/lam;
    U_vdw(i) = -G0*[1.5*(ih^3) - 0.5*(ih^9)];
    U1(i) = 4.5*G0*[ -(ih^5) + 2.5*(ih^11) ];
    U2(i) = 9*(pi^3)*G0*[ (ilam^3)*(ih^2)*besselk(3,q) -
((pi^3)/24)*(ih^5)*(ilam^6)*besselk(6,q) ];
    for j = 1:N
        UU_vdw(i,j) = U_vdw(i) + U1(i)*((delgn(j)^2) + (delsn^2)) +
U2(i)*(delgn(j)*delsn);
        U_total(i,j) = UU_vdw(i,j) + Ug(j);
    end
end

criteria = 0;
I = 0;
J = 0;
for j = 1:N
    for i = 1 : M-1
        if U_total(i,j) < criteria
            I = i;
            J = j;
            criteria = U_total(i,j);
        end
    end
end
end

```

```

for j = 1:N
    for i = 1 : M-1
        dU_total(i,j) = (U_total(i+1,j) - U_total(i,j))/dh;
    end
end

for j = 1:N
    for i = 1 : M-2
        ddU_total(i,j) = (dU_total(i+1,j) - dU_total(i,j))/dh;
    end
end

for i = 1 : M-2
    hh(i) = h(i+1);
end
hhn = hh/h0;

I
J
U_min_n = U_total(I,J)/G0
h_eq = h(I);
%k_stiff = ddU_total(I+1,J+1)
h_eq_n = h_eq/h0
delgs = delg(J)/dels
k_vdw = ddU_total(I,J)

%for j = 1:N
%    subplot(1,2,1)
%    plot(hn,U_total(:,j))
%    hold on

```

```
% subplot(1,2,2)
% plot(hhn,ddU_total(:,j))
% hold on
%end
```

## Appendix C. Effect of intercalated water layer on force constant

---

```
M_H2O = (18.01528/6.022140857)*10^-26; % kg per molecule
V0 = 0.001; % m^3/kg
a_g = 1.42*10^-10; % m
N_g = (3^-0.5)/(a_g^2);

G0 = 0.6*(1.60219*10^-1); % J/m^2
h0 = 0.6*10^-9; % m
P0 = 1.01325 *10^5; % N/m^2 (= J/m^3)
K0 = 2.15*10^9; % Pa
n = 7.15;

dhn = 0.0001;
hn = [1 : dhn : 2];
h = h0*hn;

M = size(h,2);

for i = 1:M
    ihn = 1/hn(i);
    P_vdw(i) = 4.5*G0*(1/h0)* ( ihn^4 - ihn^10 );
    ha(i) = (((n/K0)*P_vdw(i) + 1)^(1/n))*h(i);
    P_in(i) = (K0/n)*((ha(i)/h(i))^n - 1) + P0;
    V(i) = V0/(((n/K0)*P_vdw(i) + 1)^(1/n));
end

for i = 1:M
    ihn = 1/hn(i);
```

```

k_in(i) = K0*(ha(i)^n)*(1/(h(i)^(n+1)));
k_vdw(i) = 27*G0*(1/h0^2)*(-(2/3)*(ihn^5) + (5/3)*(ihn^11) );
k_net(i) = k_vdw(i) + k_in(i);
k_Seol(i) = 27*G0*(1/h(i)^2);
N_H2O(i) = h(i)/(M_H2O*V(i));
n_H2O(i) = N_H2O(i)/N_g;
end

subplot(1,3,1)
plot(hn,k_net, hn,k_in, hn,k_vdw, hn,k_Seol)
hold on
subplot(1,3,2)
%plot(hn, P_vdw, hn, P_in)
plot(hn,n_H2O)
hold on
subplot(1,3,3)
plot(hn, V)
hold on

```

# 기관과 접촉하는 그래핀의 열전도도 계측

서울대학교 대학원

기계항공공학부

김 홍 구

## 요 약

그래핀은 그 탁월한 물성으로 각광을 받고 있는 신소재이며, 특히 높은 열전도도를 보유하고 있어 열분산기를 비롯한 열관리 응용이 기대되고 있는 물질이다. 그러나 상용화에 적합한 그래핀의 형상은 기관과 면접촉을 이루는 지지된 그래핀임에도 불구하고, 현재까지 그래핀의 열물성에 대한 실험적인 보고는 매달린 형상의 그래핀에 치중되어 왔으며, 이는 지지된 그래핀의 열전도도에 대한 신뢰성 있고 신속한 계측 기법의 부재에서 기인한다.

마이크로 저항 기법의 경우 100 K에서부터 400 K에 이르는 온도 범위에서 지지된 그래핀의 열전도도 측정에 이용되었는데, 측정 정밀도가 우수한 대신에 시편제작 비용이 막대하고 패턴 공정에 따른 시편 오염의 문제가 심각하다. 반면 광열 라만 기법의 경우 시편 제작이 간편하고 실험 결과를 신속하게 획득할 수 있다는 장점이 있으나 지지된 그래핀의 열전도도 측정에 적용하기에는 측정 오차가 과도하게 크다는 문제점이 있다.

본 연구에서는 지지된 그래핀의 열전도도 측정을 위하여 광열 라만

기법을 바탕으로 그 측정 정밀도를 획기적으로 향상시키는 측정 기법을 개발하였다. 광열 라만 측정에 대한 3차원 열전달 모델을 수립하여 수치해석을 수행한 결과, 열전도도 측정 정밀도를 좌우하는 가장 결정적인 파라미터가 기관의 두께임을 규명하였으며, 극박막 기관을 도입하여 실험적으로 이를 입증하였다.

이러한 계측 기법을 활용하여 세계 최초로 350 K에서부터 600 K에 이르는 온도범위에서 지지된 그래핀의 열전도도를 성공적으로 측정하였으며, 이러한 실험 결과는 그래핀의 상용화 및 열관리 응용에 중요한 기여를 할 것으로 기대된다. 나아가서 지지된 그래핀 시편 제작 과정에서의 열처리 반복 회수와 열전도도 간의 강한 상관관계를 실험적으로 관측하였으며, 이는 열처리가 반복될수록 그래핀과 기관의 접착도가 높아지는데 기인함을 규명하였다. 박막 탄성이론에 기초한 그래핀과 기관 간의 상호작용력 및 힘 상수를 계산을 통하여 그래핀과 기관의 접착도가 높아질수록 기관에 의한 그래핀의 포논산란이 강해지는 경향성을 확인하였으며, 이는 실험적 관측을 뒷받침한다.

본 연구에서 개발한 열전도도 계측 기법은 그래핀에 국한되지 않고 다양한 2차원 물질 적용이 가능하다는 점에서 저차원 신소재의 열물성에 대한 실험적 연구에 기여할 것으로 전망되며, 지지된 그래핀의 열전도도가 그래핀과 기관 간의 상호작용에 강한 의존성을 가진다는 본 연구 결과는 향후 그래핀과 2차원 신소재의 열물성 제어 및 열전성능 향상에 활용될 수 있을 것으로 기대된다.

주요어 : 지지된 그래핀, 열전도도, 라만분광법, 포논산란, 유한차분기법  
학번 : 2011-20704